Title
Microscale organization of active liquid crystal using patterned surfaces

Permalink
https://escholarship.org/uc/item/5z18b6vf

Author
Khaladj, Dimitrius Ammir

Publication Date
2022

Peer reviewed|Thesis/dissertation

UNIVERSITY OF CALIFORNIA, MERCED

Microscale organization of active liquid crystal using patterned surfaces

A dissertation submitted in partial fulfillment of the requirements
for the degree of Doctor of Philosophy

in

Physics

by

Dimitrius A. Khaladj
June 2022

The dissertation of Dimitrius A. Khaladj, titled Microscale organization of active liquid crystal using patterned surfaces, is approved, and it is acceptable in quality and form for publication.

Dr. Linda S. Hirst (Principal Advisor)	Date

Dr. Jay E. Sharping (Committee Chair)	Date

Dr. Kevin A. Mitchell (Committee Member)	Date

Dr. Anand Subramaniam (Committee Member)	Date

To Mom and Walt, for all the valuable lessons you taught me in life.

Table of Contents

Acknowledgements

Curriculum Vitae

Dimitrius Ammir Khaladj

dkhaladj@ucmerced.edu ▪ (908) 216-4782

Professional Summary

I have more than 10 years of research experience in interdisciplinary work in applied physics, polymers, and biological material in an academic setting. In this time, I have developed skills in microscopy to characterize nano/microfabricated structures and other exotic materials to study collective motion in lyotropic active filamentary systems under confined conditions. With my training as an experimental physicist, I have experience in computational work and 3D modeling (blender), developing methods to quantify topological entropy, defect organization and director orientation; I also worked as the director of development for a sobriety company. My work has been published in several journals with collaborators abroad and I have lead projects with colleagues within my cohort.

Education

University of California at Merced   Merced, CA
Ph. D. in Physics   *Expected Graduation Spring 2022*

<u>Topic:</u> Nanoscale organization of active nematic systems via patterned surfaces
        -Advisor: Prof. Linda S. Hirst

University of California at Merced (2020)   Merced, CA
M.S. in Physics

College of Nanoscale Science and Engineering (CNSE), University at Albany-SUNY (2014)
                                                                             Albany, NY

M.S. in Nanoscale Engineering

<u>Topic:</u> *Investigation of chemically reactive additives and their impact on the mechanical properties of lithographically defined SU8*
        - Advisor: Prof. Magnus Bergkvist

Binghamton University, State University of New York (2012)
Binghamton, NY
Honors Thesis on *DNA Manipulation using Nanostructures*
Bachelor of Science in Applied Physics and Astronomy (with Honors)
Bachelor of Science in History
Minor in Global Studies (Chinese Concentration)

List of Publications

- Fereshteh L. Memarian, **Dimitrius A. Khaladj**, Derek Hammar, Linda S. Hirst. *Forming, confining and observing microtubule-based active matter*. (Submitted to JOVE)
- **Dimitrius A. Khaladj***, Linda S. Hirst. *Using Curved Fluid Boundaries to Confine Active Nematic Flow*. Frontiers in Physics. 10. 2022
- Kristian Thijssen*, **Dimitrius A. Khaladj***, Amin Doostmohammadi, Tyler N. Shendruk, Julia M. Yeomans, Linda S. Hirst. *Submersed Micropatterned Structures to Control Active Nematic Phase Separation*. PNAS 118 (38) September 2021.
- **Dimitrius A. Khaladj***, Amanda J. Tan and Linda S. Hirst. *Using epoxy-based lithography to probe confinement effects on active nematics*. SPIE Proceedings. Published 09/2019
- Luke A. Beardslee, Judith Stolwijk, **Dimitrius A. Khaladj**, Mohamed Trebak, Justin Halman, Karen Y. Torrejon, Nuttawee Niamsiri, Magnus Bergkvist. *Sacrificial Process for Fabrication of Biodegradable Polymer Membranes with Sub-Micron Thickness*. Submitted to Journal of Biomedical Materials Research: Part B – Applied Biomaterials. Vol. 104, Issue 6. First published: 16 June 2015.
- Luke A. Beardslee, **Dimitrius A. Khaladj**, Magnus Bergkvist. *Preliminary Investigation of a Sacrificial Process for Fabrication of Polymer Membranes with Sub-Micron Thickness*. MRS Online Proceedings Library (OPL). Published online: 22 January 2014.

Related Experience

University of California at Merced   *August 2016-Present*

Graduate Research Assistant
- Developed patterned surfaces and microfluidic devices composed of surface treated glass and negative photoresist using photolithography and characterized physical dimensions using AFM and SEM
- Experience using wet and dry etching, multilayer photopatterning and sputter coating to create devices and electrodes to probe conductivity of quantum dot nematic foams for gas sensors
- Purified and nucleated microtubule proteins to create a lyotropic active nematic network confined in a quasi-2D layer
- Tracked topological defects in active matter and quantified novel defect dynamics by using patterned surfaces using MATLAB, R, Bash, and Python
- Used 3D reconstructions via confocal microscopy to obtain thickness profiles of the fluorescently labeled network to observe how thickness affects active flow
- Used Blender to create 3D models and textures for illustrations in publications. Can also use Blender for rigging and animations
- Collaborated and published work with groups across the US and Europe. Also mentored and trained incoming PhD Students

Computational/Development Experience   *December 2017 - May 2020*

Director of Development
- Developed "Sobercoin" - a cryptocurrency implementation of the Litecoin protocol with associated support elements

- Developed desktop wallet and miner, blockchain explorer, and support nodes on the cloud.
- Managed worldwide team during software development and worked with the implementation process across multiple vendors
- Did full stack development work for websites and small apps using Linux, HTML, Bash, Python, C/C++, CSS, MySQL, Javascript, and React

College of Nanoscale Science and Engineering *August 2012 – December 2014*
Graduate Research Assistant
- Multidisciplinary project fabricating artificial Descemet's membrane tissue scaffolds from synthetic polymers.
- Use of photolithography, wet/dry, etching, RIE, exposure to create novel nano and microstructures using negative tone photoresist
- Trained in nano/microfabrication processing, negative tone lithography, SEM and ESEM imaging.
- Cultured cells on tissue scaffolds for immuno-stain protein activity of tight junctions with confocal microscopy
- Other skills also involved Immuno-histochemistry, DNA Purification, Ligation and Nano Imprinting Techniques

Binghamton University Physics Department/Bio-Nanoengineering
August 2011 – June 2012
Undergraduate Researcher
- Utilized nanofluidic channels to understand DNA folding and stretching.
- Use of photolithography, wet/dry, etching, RIE, exposure to create novel nano and microstructures using positive tone photoresist
- Was recognized by Binghamton Physics department for distinguished independent research by demonstrating DNA unfolding under confined conditions and measured mobility of gliding within nanofluidic devices

Fellowships and Awards

- Spring 2022 Physics Travel Award (*April 2022*)
- Center for Cellular and Biomolecular Machines Travel Award (*March 2022*)
- American Physical Society DSOFT Student Travel Award (*March 2022*)
- Center for Cellular and Biomolecular Machines Fellowship (*Spring 2021*)
- Physics Summer 2020 Research Fellowship (*Summer 2020*)
- Spring 2020 Physics Travel Award (*Spring 2020*)
- Recipient of MACES Summer Internship and Fellowship (*Summer 2019*)
- Recipient of MACES Summer research fellowship (*Summer 2018*)
- Awarded Distinguished Research at SUNY Binghamton (*May 2012*)
- Awarded Dean's List at SUNY Binghamton (*May 2012*)
- Member of Sigma Pi Sigma (ΣπΣ) Physics Honors Society (*May 2012*)

Internships/Team Participation

NASA Langley Research Center – Mentor: Dr. Cheol Park   *June 2019 – August 2019*

Alignment of Boron Nitride Nanotube (BNNT)/Polymer composites
- Mechanically tested BNNT composites in different polymer blends using tensile, pull, twisting and hardness testing
- Ran thermal testing using Differential Scanning Calorimetry (DSC) and characterized composition of BNNT/Polymer composites using X-ray diffraction and checked alignment using SEM
- Demonstrated BNNT alignment using Polyetherimide polymer matrix

NASA Europa Clipper – Mentor: Dr. Kate Craft   *September 2020*

Observation Team
- Participated in the meetings for the Europa Clipper launch mission
- Oversaw team members discussing mission logistics and plans
- Shared and discussed ideas on specific tasks to image the moon, characterize atmospheric, surface, and internal composition

Teaching-Related Experience

Teaching Assistant for the UC Merced Physics department
MATH 021, Calculus I for Physical Sciences and Engineering - Fall 2016
PHYS 008, Introduction to Physics I - Spring 2017, Summer 2017, Spring 2018, Spring 2020
PHYS 018, Introduction to Physics I for Biological Science - Fall 2018, Spring 2019
PHYS 009, Introduction to Physics I - Fall 2017, Spring 2022

Presentations/Posters

- American Physical Society March Meeting 2022. **(Speaker)** Dimitrius A. Khaladj, Linda S. Hirst. *Active Defect Control and Morphology via Variation in Oil Sublayer Thickness. (March 2022 in Chicago, IL)*
- Center of Cellular and Biomolecular Machines Thrust Meeting. **(Speaker)** Dimitrius A. Khaladj, Linda S. Hirst. *Active Defect Control and Morphology via Variation in Oil Sublayer Thickness*. (*March 2022 in Merced, CA*)
- Biophysical Society Annual Meeting 2022. **(Poster)** Dimitrius A. Khaladj, Linda S. Hirst. *Methods to Control Chaotic Active Nematic Flow. (February 2022 in San Francisco, CA)*
- Invited speaker at the University of Edinburgh by Professor Tyler Shendruk for the Shendruk group. **(Speaker)** Dimitrius A. Khaladj, Linda S. Hirst. *Control and organization of active nematic bundled microtubules via submersed micro-patterned substrates (October 2021* in *Edinburgh, UK)*
- Conference of Liquid Crystal 2021 in Poland (CLC2021). **(Speaker)** Dimitrius A. Khaladj, Linda S. Hirst. *Control and organization of active nematic bundled microtubules via submersed micro-patterned substrates (October 2021 in Karpacz, Poland)*
- Center of Cellular and Biomolecular Machines Thrust Meeting. **(Speaker)** Dimitrius A. Khaladj, Linda S. Hirst. Nanoscale organization of active nematic bundled microtubules via submersed micro-patterned substrates. (March 2021 at Merced, CA)

- American Physical Society (APS) Division of Fluid Dynamics (DFD). **(Speaker)** Dimitrius A. Khaladj, Amanda J. Tan, Linda S. Hirst. *Active nematic defect dynamics influenced by submerged microstructures November 2020*
- American Physical Society (APS) March Meeting (Cancelled due to COVID-19; presented at UC Merced). **(Speaker)** Dimitrius A. Khaladj, Amanda J. Tan, Linda S. Hirst. *Submerged microstructures generate a soft boundary effect on active nematic flows. (March 2019 in Merced, CA)*
- Gordon Research Conference. **(Poster)** Complex Active and Adaptive Material Systems Dimitrius A. Khaladj, Amanda J. Tan, Linda S. Hirst. *Active nematic systems in confined geometries. (February 2019 in Ventura, CA)*
- Gordon Research Seminar. **(Poster)** Complex Active and Adaptive Material Systems Dimitrius A. Khaladj, Amanda J. Tan, Linda S. Hirst. *Active nematic systems in confined geometries.* (*January 2019 in Ventura, CA)*
- APS Far west. **(Poster)** Dimitrius A. Khaladj, Linda S. Hirst. *Fabrication of PDMS Surfaces for the investigation of Microtubule Tracking and Mobility.* (*November 2017 in Merced, CA)*
- SUNY Polytechnic Nanoengineering. **(Poster)** Dimitrius A. Khaladj, Luke Beardslee, Magnus Bergkvist. Investigation of chemically reactive additives and their impact on the mechanical properties of lithographically defined. (*June 2014 in Albany, NY)*
- Preliminary Investigation of a Sacrificial Process for Fabrications of Polymer Membranes with Sub-Micron Thickness. (*December 2013 in Boston, MA)*

Tutoring and Public Service

- Freelance Tutoring High School Students (October 2016- May 2018)
- Tutored calculus at University at Albany Disability Resource Center (September 2014 – December 2014)
- Mentored nanoscience for NanoAMPS at local middle schools for CNSE. (August 2013 – May 2014)

List of Figures

thickness of is obtained by measuring the difference between the heights of the active nematic film and the solid substrate, multiplied by the refractive index of the oil (1.3). (d) Near the steps, the 3D reconstruction of the active nematic confirms the film is flat without any deformation or curvature. Scale bars = 100µm. Image was produced from Dr. Mohamed Amine Gharbi in "Submersed Micropatterned Structures Control Active Nematic Flow, Topology and Concentration" *[9]*.

Figure 4.2. (a) 3D rendered images depicting an active film residing at the oil-water interface above different substrate depths. The active flows drag the underlying oil sublayer as viscous dissipation is depth dependent, affecting active nematic film dynamics. (b) Fluorescence microscope image of the active nematic bundled-microtubule film above a submerged trench. Scale bar = 250µm.

Figure 4.3. (a-b) Distribution of +1/2 (dark green) and -1/2 (magenta) defects as a function position x. (c-d) Probability of nematic director oriented less than 10° from the direction parallel to the trench wall as a function of x. (e-f) Normalized root mean square fluid velocity profile across the trench.

Figure 4.4. (a) 3D rendered submerged steps. (d) Fluorescence microscope image of micro-milled stairway and the superjacent active bundled-microtubule film. Scale bar = 500µm where the step locations are indicated by red dashed lines and the oil depth increases from left to right.

Figure 4.5. Illustration of the cross section of the submerged steps.

Figure 4.6. Plus (dark green) and minus (magenta) defect distribution as a function of position down the stairway x. (a) Measurements from experiments for steps of width wt = 500µm (b) Measurements from simulations for steps of width of width wt = 5R.

Figure 4.7. (a) 3D rendered image of submerged pillars (b) Fluorescence microscope image of the bundled-microtubule film above the SU-8 micropillar. Scale bar = 100µm.

Figure 4.8. (a) Submerged SU-8 pillar with a +1/2 defect penetrating the top portion of the pillar. (b) As the +1/2 pushes toward the interior of the pillar, it quickly dissipates leaving the top of the pillar completely deplete of active material.

Figure 4.9. (a) Radial defect distributions from experiments (b) Radial defect distributions from simulated work. (a-c) x-y trajectories of example ±1/2 defects dynamics in the vicinity of the pillar. Time along the trajectory is displayed as circular markers colored blue at the initial time and changing to red at the final instant. (c-d) +1/2 defects deflecting from the pillar; experiments (c) and simulations (d). (j) Experimental x-y trajectories of +1/2 defects being absorbed at the pillar boundary through defect annihilation with the -1/2 residing at the perimeter.

Figure 5.1. The two-tier active nematic system. (a) Two channel laser scanning confocal microscopy images showing a pillar (blue) overlaid with the active nematic layer (red) a z = 0um and (b) z = 7.45um with respect to top of the pillar. (c) graph showing curvature

List of Abbreviations

- 5CB   4-Cyano-4'-pentylbiphenyl
- α Activity constant
- ATP   Adenosine triphosphate
- c   Characteristic material constant
- D   Diffusion Constant
- Δ_t Trench depth
- Δ_s Step height
- E_c Threshold electric field
- F   Free energy per unit area
- γ Effective friction coefficient
- GDP   Guanosine diphosphate
- GTP   Guanosine-5'-triphosphate
- h   Fluid depth
- h(r)   Fluid height as a function of depth
- h_0 Height of oil layer
- h_p Height of pillar
- h_s Fluid depth of shallow region
- h_t Fluid depth of deep region
- K   Elastic constant
- k_B Boltzmann constant
- M2B   Microtubule buffer
- η Viscosity
- n   Step number
- Δn Birefringence
- $\hat{n}$ Vector of director
- n(x)   Step number as a function of position
- η' Effective viscosity of oil
- PAG   Photoacid generator
- PEB   Post exposure bake
- PEG   Polyethylene Glycol
- q   Defect charge
- R_p Radius of arbitrary particle
- r_p Radius of pillar
- S   Order parameter
- T   Temperature
- θ Director angle
- v_{rms} Root mean square velocity
- T_g Glass transition temperature
- w_s Width of steps
- w_t Width of trench

Abstract

Active matter is a growing interdisciplinary field of science that studies the collective motion of different species of particles and living organisms. This field of research is often bio-inspired as collective motion of fish, birds and insects are ubiquitous throughout nature. Such behavior is not just limited to the macroscopic world but is also found in the micro- and nanoscopic realms as well. Under the microscope, it can be observed that bacterial and protein assemblies are subject to the same group motion serving as the inner machines vital to the functions of life and natural forces of the world. In this thesis, I focus attention to the interesting method of an actively driven bundled microtubule network in a lyotropic liquid crystal phase.

The active nematic bundled microtubule system has gained substantial international exposure in the field of soft matter. Several groups across the world have not only reproduced this novel system, but also developed new methods to measure and probe its properties and kinematics. These actively driven protein networks have become a useful framework to study energy driven particles in complex structured fluids. An interesting method to probe the behavior of this system is the the implementation of boundaries serving as a useful strategy to control defect flow, morphology and dynamics. In this thesis, I study the behavior of an active nematic microtubule system confined to several different geometries. I was initially motivated from our preliminary work, when I observed that submerged 3D structures can influence defect dynamics by organizing their flows and pinning defects at specific locations. This prompted me to investigate active nematic flows in microfluidic devices in different confining conditions, which will be covered in this work.

For my first project, I engineered micropatterned surfaces using photolithography to control local orientation directors to take advantage of the interplay between surface curvatures and topological defects. Epoxy-based lithography represents a simple approach to develop lab-on-a-chip methods to probe active materials. In this dissertation, I will discuss optimized fabrication methods using negative tone epoxy-based photoresists to create microfluidic devices for active matter systems. I demonstrate that arrays of circular structures and submerged topographies can generate a variety of liquid crystal defect configurations, not typically observed on unconfined planar surfaces. I then build on these observations by considering the creation of new interfaces not limited to hard boundaries.

For my second project, I demonstrated that soft or virtual boundaries can be generated by submerged structures. With the assistance of micro patterned surfaces, different submersed geometrical patterns were created for my analysis: trenches, pillars, stairways, and undulated sinusoidal structures. I investigated the spontaneous flows of this novel system as pillar dimensions influenced active material flow due to abrupt changes in oil depth. This created virtual boundaries because of the change in the effective viscosity in proximity to the boundary. In this study, I collaborated with several groups to develop simulations and other micro-milled patterns.

Finally, my third project was to confine active material but by curving the oil-active layer interface, creating a two-tiered elevated system. The geometry for this work was submersed pillars impinging on the interface, creating a two-tier continuous active layer in which material is partially confined. Active flows above the pillars were influenced by the circular geometry and the thin oil layer resulting in physical changes of the material i.e., depletion. Building from the second project, the thin oil layer beneath the active material was thinner in the region above the pillars relative to outside the encircled area, consequently producing an area of higher effective friction. This was confirm using 3D reconstructions of the curvature of the active layer and auto-fluorescent pillar using confocal microscopy. This resulted in changes of velocity fields, defect densities and active length scales.

Overall, I have investigated new methods for probing a living liquid crystal system capable of generating internal flows using microfluidic devices. This new way to confine active material opens many opportunities to control and organize topological defects and materials at nanoscales using simple micro-fabricated structures. I hope that we can move this method and platform to other active or even passive liquid crystal systems for biomedical and electronic devices. Such methods can be invaluable to pursue the integration of liquid crystal phase to nanoelectronics. The work presented in this dissertation has demonstrated the adaptability of this active protein assembly and open new possibilities to organize structured fluids.

Chapter 1: Introduction

1.1   What is active matter?

Collective motion of particles in living organisms is ubiquitous throughout nature. Nature is dynamic where particles exert force on their environment to move, either individually or collectively. This framework is the essence of active matter. Active matter is a new field of study that investigates the collective motion of particles. Particles are loosely defined, as it can be anything from flocks of birds (Figure 1.1a), swarms of insects (Figure 1.1b), schools of fish (Figure 1.1c) to smaller components at the microscale, such as bacterial suspensions (Figure 1.1d) and novel protein assembles (Figure 1.1e). The components of these systems tend to be energy driven, where particles consume energy in their local environment to exert a force resulting in an overall motion. In essence, active matter is composed of energy driven particles that are capable of collective motion. Outside the observation of collective movement, active matter has other interesting properties. Active matter systems have properties of self-motility, self-healing, internally generated flows, and synchronous dynamics [10]. These characteristics are often bio-inspired where nature is defined by its consumption of energy and self-propulsion within its local environment. Despite how consistently we observe these motifs in living systems, active matter has found itself in non-living or synthetic systems like bristle-bots [11].
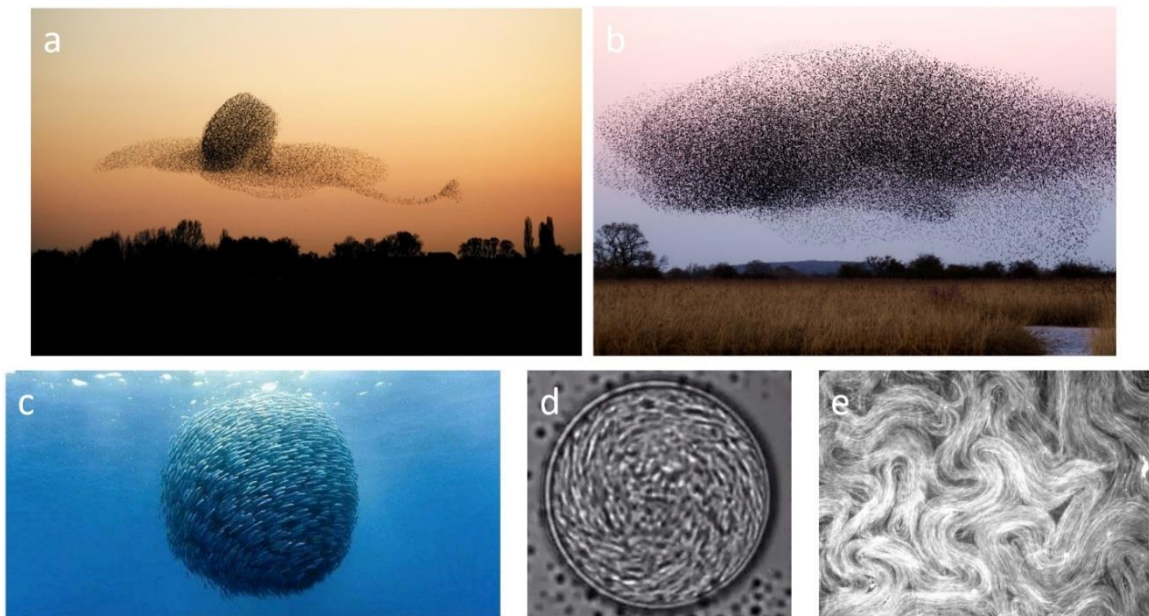
Figure 1.1. Examples of active matter. (a) a flock of birds collectively moving collectively (reproduced from Popkin, 2016 with permission ©2016 Springer Nature) [1], (b) a swarm of bees [2], (c) a school of fish [3], (d) bacterial within a circular confinement (adapted and reproduced from Lushi 2014 with permission ©2014 PNAS) [4], (e) a bundled microtubule/kinesin network confined in a quasi-2D configuration between two immiscible fluids.

Referring back to the previous example of active matter, from a macroscopic perspective, flocks of birds [1], swarms of insects [2] and even schools of fish [3], although a common sight to see when viewing the world, methods to describe this motion on how species determine its pathways in their respective spaces, have been of interest in material science. Although, each of these unique species consume energy from their habitats to move, each of these cases differ in terms of how each particle or organism determines its pathway.

If we were to go smaller, we can observe similar collective motion with cells, bacterial suspensions [4], and protein assemblies where their pathways are determined by regulatory biochemical processes. In Figure 1.1d for example, bacteria can move in a vortex-like fashion if the bacteria can sustain themselves where their pathways are determined not only by the availability of energy but also by hydrodynamic forces and chemical signals [12] [13]. More relevant to my presented work, protein assemblies such as kinesin draw available energy in the form of adenosine triphosphate (ATP) where their paths are determined by motor proteins walking along microtubules. If the microtubules were bundled continuously by these motor proteins and then began to move, what kind of motion can be observed? This essential biological system has been modified to create a complex lyotropic active nematic fluid that generates topological defects continuously when in the presence of ATP. This system has become a useful experimental model for understanding topological defects, morphology, and kinematics. Outside of the biochemical, hydrodynamic, and intrinsic properties determining how these systems move, their microenvironment is another factor that should be considered. Using different interfaces, scaffolds and other surface designs can help guide and optimize collective motion of particles [14]. I add to this body of work using microfluidic devices to organize active liquid crystal systems.

1.2   Overview

In this Chapter, I have defined active matter using several examples, both relatable to the human experience and within research. Although a few examples of active matter have been presented, it can be safely said that all livings things exist within this category. Despite seeing this phenomenon exclusively within living systems, growing interest in developing synthetic materials and *in vitro* assemblies that fit this behavior, has given rise to a range of methods and models to probe this novel system. Going beyond the creation of an active matter system, methods to organize, arrange and induce consistent motifs of motion by modifying its microenvironment, has also been of growing interest in this emerging field. Examples such as colloidal suspensions, liquid crystal phases, protein assemblies, etc., have been subject to methods for nano and microscale organization; the focus of this work will be using patterned microfluidic devices to organize the flows of an *in vitro* active nematically bundled microtubule/kinesin assembly. For this dissertation, I will present previous findings of this topic, including its scientific foundation and my own contributions to this work. In Chapter 2, I will cover the theory and scientific background of this topic with the mention of reported experimental examples. Chapter 3 will cover my preliminary work reproducing the active system and probing its motion using microfluidic devices. In Chapter 4, I will discuss how different submerged geometries can influence defect kinematics and positional organization via the induction of a soft boundary. Chapter 5 will

discuss a method I have developed to control active material through curvature and how making slight changes to the systems microenvironment can change its continuity and kinematics. Finally, Chapter 6 will reflect on future directions from my findings and possible explanations that can further the field of active matter. I also hope in this dissertation, that these methods will not only be applied to active matter systems, but also for application of liquid crystal phase in the semiconductor industry where examples of surface or interfacial modification can impact material organization [15].

Chapter 2: Background and Theory

2.1 Introduction

Topological defects in complex fluids are a robust and diverse field of research. There are many systems that are subject to non-Newtonian dynamics and exhibit complex forms of arrangements, ordering and aggregations. One interesting state of matter, the liquid crystal phase, is commonly characterized as a complex fluid. These fluids have many applications in electronic devices, self-assembly of macromolecules, and emulsions [16] [17] [18] [19]. More specifically, molecules in the liquid crystal phase tend to locally order whether prompted through temperature or concentration. Over longer ranges, discontinuities in molecular alignment can occur [20]. These discontinuities are referred to as disclinations or defects that spontaneously occur whether the liquid crystal material is thermotropic or lyotropic [16]. Defects form when two molecular entities within a local vicinity are in some way orientationally mismatched when a seamless transition of alignment of either structure is impossible. Although these defects occur spontaneously in solid or liquid crystalline material, topological defects can be induced by a boundary. In the scope of this chapter, I will define what is a complex fluid, how the liquid crystal phase fits into this context, and how topological defects are formed near a boundary. I will also discuss the microtubule protein assembly in focus of this dissertation, its composition and work already reported on this system.

2.2 Complex fluids

Complex fluids can be any fluidic system comprised of one or several components, that can have properties of both a liquid and a solid phase. If we consider a homogeneous material like water, which obeys Newtonian physics, hydrodynamics etc., it is explicitly defined by its isotropic state where it is indistinguishable no matter where it is probed. On the other hand, this may not be the case for a complex fluid. A complex fluid may not retain such molecular organization because depending on certain conditions, probing different axes or locations, can result in different properties. Because these different orientations or areas of measurement can be structured differently, a complex fluid will not have the same measurements as different properties are the result of a specific condition as the material reorganizes to an alternative energetically favorable state.

Complex fluids are often a combination of several substances. Examples of complex fluids are emulsions and colloids. If we consider an emulsion like a dollop of mayonnaise or whip cream (a mixture of oil/fats in an aqueous suspension); it is a fluid but behaves like a solid because it maintains its shape unlike water. If we were to expose these dollops to small stresses, it would somewhat maintain the continuity of its original shape. If we were to then apply more stress to the dollop, the emulsion would flow where the molecules would rearrange themselves and slide passed each other as the stress changes its form. If we were to compare this to a solid, the solid would deform but ultimately fracture with increasing stress as opposed to the emulsion, which would just continue to flow. However, fluids that have short range orientational or positional order, do exist and their phase is defined as a liquid-crystal.

Liquid crystal is another kind of complex fluid with very interesting properties. A material in this phase does not have to be a mixture or emulsion comprising of many ingredients but rather, of just one. One distinct feature held by materials that can enter liquid crystal phase is that their components can be a myriad of molecular shapes such as, long rod-like structures with rigid semi-flexible physical properties or disk-shaped (discotic) that can stack on top of each other [16]. More relevant to our work, materials like these rod-like structures can be modelled as cylindrical tubes. These materials in the liquid crystal phase can be proteins, bacteria, and even cells i.e., they need not be limited to molecules [21]. Under the right conditions, these tube-like structures can exhibit both positional and orientational order in short ranges [20].

2.3 Liquid crystal ordering

In section 2.2, I discussed that molecules in the liquid crystal phase tend to exhibit some short-range order with respect to their position and/or orientation, transitioning from isotropic to anisotropic phase. The isotropic phase implies no molecular ordering where if the material were observed from different orientations, the material would not be distinguishable from any other arbitrary point it was probed. Anisotropy implies a directional dependency of the material where it can exhibit different properties when observed in different directions or orientations. When measuring an anisotropic material, different properties such as optical, electric, and/or mechanical changes can be a consequence of material ordering. Anisotropy is defined by the distribution of the material's director field aligned in a one direction, $\hat{n}$.
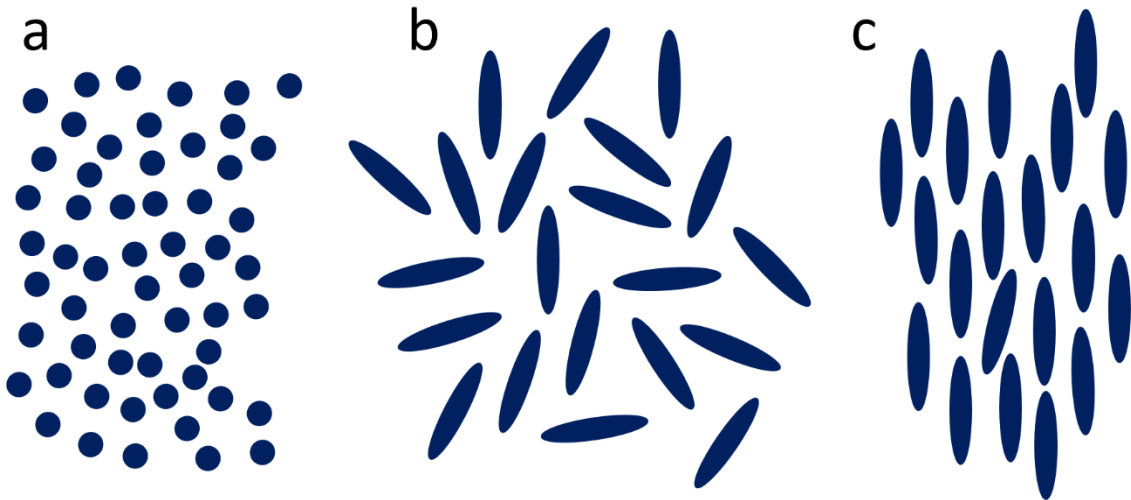
Figure 2.1. Indistinguishable Particles in (a, b) isotropic phase where S=0 and (c) anisotropic phase where S=1.

There are two conditions that can cause a material to enter the liquid crystal phase: thermotropic or lyotropic. Thermotropic phase is the tendency for molecules in isotropic phase to transition to anisotropic phase via changes in temperature, entering a first order phase transition (an abrupt change in phase depending on volume and energy) [16]. The

lyotropic liquid crystal phase can transition to the anisotropic phase as a function of both temperature and concentration. An example of a lyotropic phase can be surfactants self-assembling into micelles at the critical micelle concentration [16], although it would not in a liquid crystal phase. Materials in lyotropic liquid crystal phases of matter, however, can largely be found in biological systems and has been a focus for active liquid crystal systems which will be discussed later.

The simplest and largely applied thermotropic liquid crystal phase is the nematic phase. In the nematic phase, molecules tend to align themselves on average in the same direction however, there is a considerable degree of variation in molecular tilt with respect to the axis from the director of the nematic material. To characterize the average variation of molecular tilt, the nematic liquid crystal material can be quantified using the order parameter equation:

$$S = \frac{1}{2}\langle 3cos\,\theta^2 - 1\rangle$$

This order parameter is a Legendre polynomial used to describe the orientational order of the liquid crystal material where θ refers to the angle between the molecule and the director, $\hat{n}$ [16]. If $S = 0$, this would imply that there is no orientational order or alignment between the molecules; this configuration can be described as in the isotropic phase. If $1 > S > 0$, then there is some orientational order and alignment, where the material is approaching or is already in the anisotropic phase. If $S = 1$, there will be perfect orientational order between liquid crystal molecules; in this configuration, the material is in the anisotropic phase and crystalline. For a thermotropic liquid crystal, the phase transitions are temperature dependent thus heating the material will cause molecules to lose its orientational order going from nematic, back to isotropic. If the system was lyotropic, concentration would be another parameter to consider as decreasing concentration can result in a transition from the anisotropic to isotropic phase if temperature were constant. The organization and corresponding order parameters S can be illustrated in Figure 2.1. If $S = 0$ as depicted in Figure 2.1a-b, there is no distinguishable order of the bulk material. Should the molecules transition from a state depicted in Figure 2.1b to the state represented in Figure 2.1c, it is inferred that the system has transitioned from the isotropic to anisotropic phase, where the order parameter is quantified as $S \approx 1$.
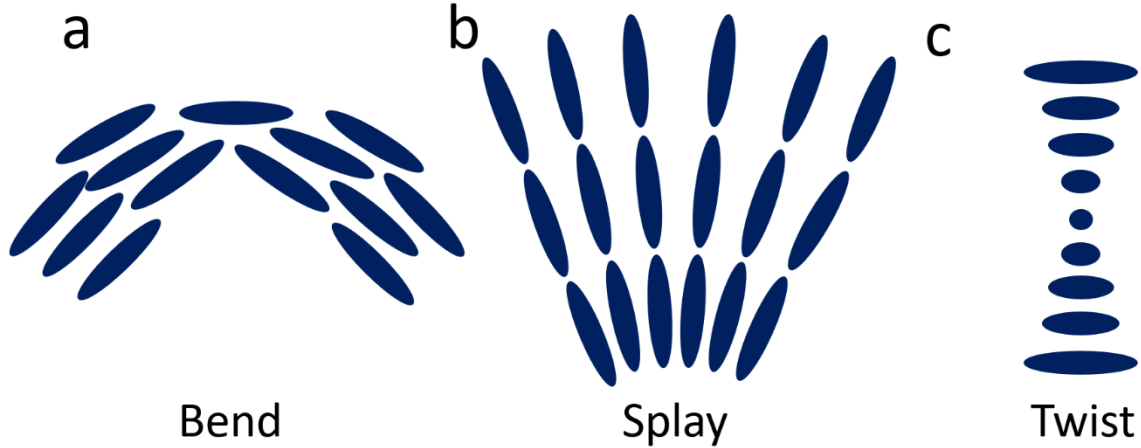
Figure 2.2. Different modes of liquid crystal phase organization: (a) Bend, (b) Splay, and (c) Twist.

While in these phases, materials can deform under external forces whether mechanically or depending on the liquid crystal, through electromagnetic fields. Deformations cause changes in the director via variations in molecular orientation. For nematic materials, the ordering is deformed, and three classifications can be identified: splay, twist, and bend. The free energy, F of a deformed nematic liquid crystal can be expressed as:

$$F = \frac{1}{2}K_{11}(\nabla \cdot \hat{n})^2 + \frac{1}{2}K_{22}(\hat{n} \cdot \nabla \times \hat{n})^2 + \frac{1}{2}K_{33}(\hat{n} \times \nabla \times \hat{n})^2$$

Each term represents the free energy of deformation in terms of splay, twist, and bend respectively [1]. K_{11}, K_{22}, and K_{33} are the Frank elastic constants and $\hat{n}$ represents the director field. Liquid crystal material exhibiting bend are locally aligned at short range but gradually change direction over a longer range of length (Figure 2.2a). Splay deformations have similar local alignment but will gradually change over longer distances as liquid crystal molecules align in multiple directions (Figure 2.2b). Finally, twist is when liquid crystal molecules gradually rotate on an axis (Figure 2.2c). In nematic systems, topological defects that are characterized by defect charges. Many defect charges are often a combination of bend, splay, and twist.

Deformations can be influenced by external forces resulting variations in the director field. Liquid crystal material in nematic phase is stabilized because of the increase in free volume and hence entropy [22]. Within this phase, structural inhomogeneities and external forces can cause mismatches between neighboring domains having different directions resulting in a defect to take place [23]. Defects are characterized by their charges, which are identified by the change in the director around a specific point. In the next section, I will discuss how defects are characterized [24]. Topological defects are important because they describe the broken symmetry of the ordered material in the liquid crystal phase.

2.3.1 Characterization of defects in liquid crystal phases
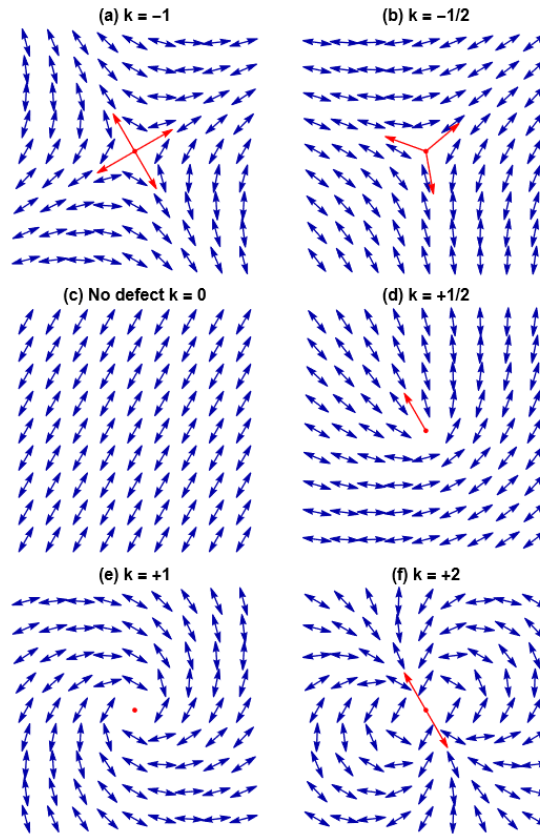
Figure 2.3. Topological defect charge illustrations with topological defect charges of (a) -1, (b) -1/2, (c) 0, (d) +1/2, (e) +1, (f) +2. Image was reproduced from Tang et al with permission ©2017 Soft Matter, Royal Society of Chemistry [5].

Over long distances within a material in the nematic liquid crystal phase, there are competing boundary conditions and external fields that can result in continuous variations of orientation. These variations of orientation of the director $\vec{n}$ can change as a function of position $\vec{r}$ resulting in deformations. If a liquid crystal material is in the nematic phase, bend, splay, and twist play a crucial role in the formation of discontinuities as different permutations of these deformations generate a defect. The topological defects observed in the material in the nematic phase can be quantified by measuring the change in φ of the director or rather the change in angle of the director over a range of 360° depicted in the illustration from Tang et al (Figure 2.3) [5]. φ is the change of direction of the director field in the enclosed area. These defects are characterized by their defect charge q enclosed around a point at the core of the defect, which is defined as:

$$\oint d\varphi = 2\pi q_{enclosed}$$

For passive liquid crystal phases, defects will annihilate with their oppositely charged partners overtime resulting in more macroscopic organization. Defects can return when exposed to some internal or external force but once again, if left unperturbed, will eventually annihilate once more. For active systems, this is will not be the case, as defects are capable of annihilating and reforming continuously if there is energy present in the system.

2.3.2 Applications of nematic liquid crystal phase

The most well-known application for the liquid crystal phase is liquid crystal displays or LCDs. The introduction of liquid crystal has resulted in a huge market of cheaper electronic goods that can range from big screen TVs, monitors, digital/smart watches, and smart phones [16]. In general, liquid crystal devices are ubiquitous both on the market with a broad range of research developing new liquid crystal phase molecules [16] [25] [26] [27]. Today, most LCD devices are composed of nematic liquid crystal for their active medium with optimized reflective, transmissive, and electronic properties [16]. In its basic form, the liquid crystal nematic medium between two parallel plates serves as a single pixel that can change its optical and electric properties by making variations in molecular orientation through an external applied field (Figure 2.4) [16].
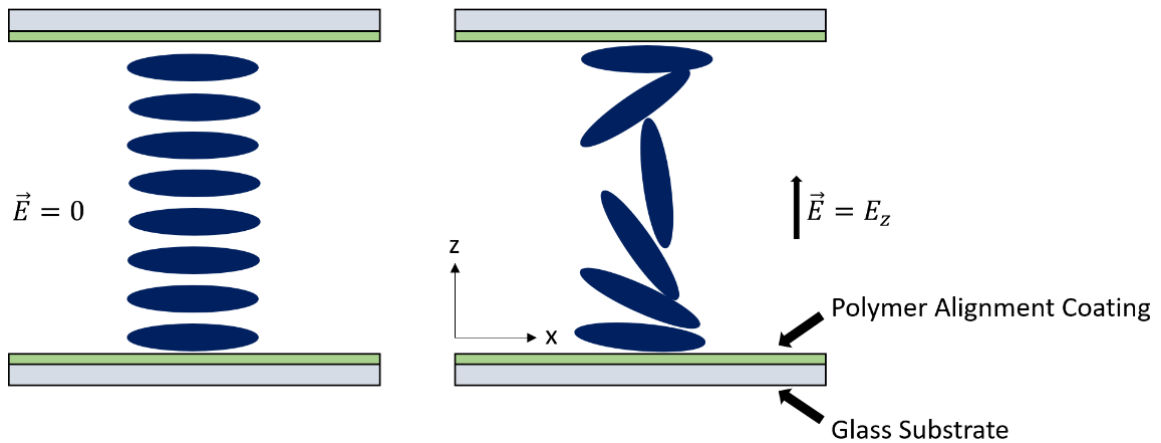
Figure 2.4. Response of a planarly aligned positive dielectric anisotropic liquid crystal along the direction of an external electric field in the +z-direction. E_z is the applied electric field in the z-direction.

Molecules not under the influence of an external field will have a strong tendency to be planarly aligned on the surface. The mechanism that determines whether a device is on or off is the alignment and reorientation of the liquid crystal medium once an electric field is applied. The polarization of light through a liquid crystal medium can be explained with a block of material in the liquid phase sandwiched between two crossed polarizers. If we consider unpolarized monochromatic light passing through the first polarizer oriented in the y-direction, the light will become linearly polarized. As the polarized light hits the block of the liquid crystal material, it is polarized into two waves in two orthogonal

directions with amplitudes of $A\cos\theta$ and $A\sin\theta$, where θ is the angle between the director of the liquid crystal and the first polarizer. Both these components can be treated independently when passing through the liquid crystal layer. After passing through the second polarizer oriented in the x-direction, the transmitted intensity will vary as a function of $\sin^2\theta$ where the maximum value of rotation of the material's director is 45°. The intensity of light once it has passed through the crossed polarizers and liquid crystal medium can be expressed as:

$$I = I_0 \sin^2 2\theta \sin^2(\frac{\pi d}{\lambda}\Delta n)$$

From above, Δn is the birefringence, d is the thickness of the liquid crystal material, and λ is the wavelength of light. Changes in the director field can alter intensity of transmitted light as well as its birefringence. In everyday electronic devices, this is done using applied electric fields with liquid crystal molecules designed to be polarized by these fields.

When a molecule is polarized, a dipole is created on the molecule causing it to align parallel to the direction of the applied electric field; this is referred to as a Fréedericksz transition [16]. The transition of the bulk nematic when deformed is a splay deformation. When deformed, there are two competing responses that occur upon the electric field's application. The nematic molecules will align to field at the cost of elastic energy. Molecules that are close to the surface can be assumed to be tightly anchored on both substrates and will not change in orientation to the direction of the field. When the electric field is applied, there will be a change in free energy which can be expressed as:

$$f_e = -\frac{1}{2}\varepsilon_0 \Delta\varepsilon E^2 \sin^2\theta$$

The molecular reorientation will lower the free energy of the system where the angle, θ is defined as the director angle along the x-axis. Consequently, the elastic properties of the liquid crystal phase will act to oppose the motion with an increase in free energy:

$$f_{splay} = \frac{1}{2}K_{11}(\nabla n)^2$$

Where the director $\hat{n}$, is defined as:

$$\hat{n} = cos\theta(z)\hat{x} + sin\theta(z)\hat{z}$$

The expressed vector is represented in the x-z plane by varying in the direction as a function of z where the free energy for splay is rewritten as:

$$f_{splay} = \frac{1}{2}K_{11}(\frac{\partial\theta}{\partial z}cos\theta)^2$$

When integrated over the distance of the spacing between the two plates represented in Figure 5, we can obtain the free energy per unit area:

$$F = \int_0^d [-\frac{1}{2}\varepsilon_0 \Delta\varepsilon E^2 \sin^2\theta + \frac{1}{2}K_{11}(\frac{\partial\theta}{\partial z}cos\theta)^2]dz$$

Assuming there is a strong anchoring limit of the nematic molecules, the threshold electric field for a splay Fréedericksz transition is:

$$E_c = \frac{\pi}{d} \sqrt{\frac{K_{11}}{\varepsilon_0 \Delta \varepsilon}}$$

From above, K_{11} is the splay elastic constant, E_c is the threshold electric field, and d is the spacing or the general thickness of liquid crystal material slab between the two treated plates.

This example is much more simplified compared to real LCDs. The above example for realigning liquid crystal molecules assumes no twist within the nematic medium. More realistic liquid crystal displays are composed of twisted nematics. Although very similar to a simple nematic design, twisted nematic displays within a pixel are not uniformly aligned in a specific orientation or direction as there is a 90° twist between the upper and lower plates. Molecules in this state can rotate, acting like a waveguide. The 90° twisted alignment produces a bright state when no field is applied. Should a field be applied, the molecules will reorient, parallel to the electric field between the conducting plates reducing the birefringence of the device down to zero thus creating a dark state.

2.4   Liquid crystal anchoring

The anchoring of molecules in the liquid crystal phases refers to the orientation of the nematic director $\vec{n}$ on a boundary, whether it is a surface or an interface [28]. The interface aligns the director of the components in the nematic phase in a biased direction along the boundary upon contact. The anchoring behavior is an interplay of steric interactions of the bulk molecules and elastic energy [28]. The boundary induces parallel alignment of the liquid crystal material for example, uniform planar anchoring can be achieved when a substrate/surface is coated with a polymer layer. Once the layer is evenly coated, mechanical rubbing can be applied causing the polymer chains to align [22]. This results in the director aligning in parallel to the substrate and along the rubbing direction. Other methods such as microfluidics can promote anchoring as the built-in structure serves as a solid boundary for liquid crystal molecules to align. Another example of anchoring would be confining material in the nematic phase between two immiscible fluids i.e., confining the system from 3D to a quasi 2D configuration. Experimentally, this has been achieved where biological proteins were confined between the boundary of an aqueous solution and an oil layer [29]. This introduces an interesting observation as to what we can define as a boundary. A boundary can be more than a hard surface, it can be an interface between two different fluids or even the same material under different conditions. Doostmohammadi et al [30] reported that oil substrates of different viscosities can be used to generate boundaries. Anchoring can be very useful to influence defects and organizing flows of active structured fluids for materials in liquid crystal phase. My aim in this dissertation is to demonstrate that applications to anchoring passive liquid crystal systems, can be used to anchoring active matter in a liquid crystal phase.

2.4.1 Patterned surfaces aligning/anchoring material in liquid crystal phase

Patterned surfaces have offered new ways to organize materials and regulate flowing particles for both research and industry. Strategies to create more long-range alignment of the director field can be ideal without the need for external fields mentioned in section 2.3.2. Furthermore, such methods can be applied to materials in the liquid crystal phase that are not susceptible to external fields making patterned fluidic devices very appealing. Examples of applying these methods have been demonstrated for passive liquid crystal systems where beautiful birefringent mosaics and optical applications can be actualized [31] [32] [33] [34]. I provide two examples of liquid crystal phases, nematic and smectic, to demonstrate the efficacy of patterned surfaces to anchor directors and positionally organize defects.

2.4.2 Nematic and smectic anchoring using patterned surfaces

Molecules in passive liquid crystal systems such as (4-Cyano-4'-pentylbiphenyl) 5CB demonstrate anchoring effects within microfluidic devices. Microchannels can have strong uniform homeotropic or planar orientation of a director field creating uniform nematic alignment with a complete depletion of defects along the channel axis. Experimental findings by Sengupta et al [22], show that 5CB molecules demonstrate anchoring in a microfluidic device resulting in changes in birefringence. Long range uniform alignment is not likely to occur for unconfined material, however, the presence of the channel rectifies this by providing longer range organization near the boundary. Homeotropic anchoring at surface boundaries in tandem with hydrodynamic flows can influence optical properties. For rectangular channels, there can be many equilibrium configurations of the nematic director field from an application-based perspective [22].

Experimental and computational findings regarding the relationship between convection flow and nematic ordering were reported by Sengupta et al [22]. This work demonstrated the coupling of flow and nematic ordering of 5CB in liquid crystal phase confined to a rectangular trench. Three flow regimes were investigated in terms of convection flow strengths and its influence on director orientation. The flow profiles that were investigated in this work was weak (10µm/s), medium (30µm/s) and high (100µm/s) flow regimes to examine the interplay of the liquid crystalline structure and hydrodynamic forces.

For weak flow regimes, the nematic structure was the same or not too different from a no-flow regime with the director fields of bulk molecules remaining perpendicular to the flow direction. With small hydrodynamics forces, the 5CB was able to maintain its homeotropic continuity. Optically examined using crossed polarizers, there was a low signal for any changes in birefringence for both the x-y and y-z planes except for the walls of the channel where the directors underwent some bend deformations due to surface anchoring. The weak flow was not enough to overcome the nematic elastic forces, and director orientation had similar continuity to an unperturbed system.

Medium flow regimes demonstrated more complex flow rheology which was due to more competition between the nematic elastic energy and hydrodynamic flow [22]. Symmetrical variations in the birefringence along the center of the microchannels were also observed. Both experimental and numerical simulations found both complex splay and bend

deformations, specifically at the center of the channel where flow profiles were strongest. The director fields are found in a nearly flow aligned state relative to the weak flow regime. This complex behavior of the director field is a direct result of the coupling between the local shear and local director orientation. The medium flow regime represents a more complex state due to the direct competition of flow and orientation. Finally, the high flow regime demonstrated a configuration of a flow state that overcomes the nematic alignment. The nematic profile along the axis of the trench evolves into a flow-aligned state where hydrodynamic forces completely overcome the material's elasticity and the nematic director runs completely parallel to the direction of the flow. It is demonstrated that the coupling between flows and the nematic director field can be a non-intrusive optofluidic velocimetry technique for lab-on-a-chip methods. These changes in the director field from flow show alterations in physical and optical properties of the material. In other words, generated flows to effect director fields changing birefringence are a technique described as optofluidic modulation.

The next example covers a smectic liquid crystal phase organized using pillars in the absence of an external force. Instead, the alignment of material in the liquid crystal phase is entirely driven by the presence of fabricated micropatterns with no external perturbations such as fields or hydrodynamic pressures. Using surface patterns to directly influence bulk material alignment with boundaries can be an interesting method to integrate into nanoelectronics. Photolithography, although being the main approach to produce transistors in everyday devices, it is limited by the wavelength of light that determines feature sizes of the patterns [35]. Developing bottom-up methods/designs are an important tool for developing more complex hierarchical structures and potentially smaller feature sizes. Honglawan et al demonstrates anchoring of Smectic A (SmA) layers in proximity of microfabricated pillars [19]. Molecules in the SmA phase are rigid biphenyl molecules with semi-fluorinated chains that forms at ~114°C and can retain its liquid crystal structure when quenched to room temperature. Honglawan reports that SmA liquid crystal phase spontaneously form highly organized hexagonal arrays of toric focal conic domains (TFCDs) as the smectic layers wrap around the pair of disclination lines formed by a circle as a straight line passed through the domain center. This is possible because the toric focal conic domains form spontaneously when there is a decrease in the surface energy, outweighing the elastic energy cost of bending the layers of the smectic liquid crystal [36]. Due to the dimple-like deformation of the liquid crystal fluid/air interface, there is an increase in surface energy resulting in a toric focal conical domain that is formed.

TFCD domains were dependent on pillar spacing and diameters. The domains were able to form at the critical diameter $D_c \sim 1\mu m$ of spacing on top of a pillar when submerged within the smectic fluid. TFCDs on top of the pillar formed a larger dimple on the surface because they are centered at a lesser depth below. For unsubmerged square arrayed pillars, the TFCDs formed in between the center of four pillars. In this instance, Honglawan found that a critical spacing of $S_c \geq 5\mu m$ is required to form these domains. Furthermore, if $S < S_c$, the liquid crystal layer aligns in parallel to the bottom of the substrate causing the spacing between the pillars to fill up preventing the defect domain from forming regardless of fluid thickness. When confined within a space smaller than the critical spacing of 5µm,

homeotropic alignment of molecules at the substate surface become energetically favorable.

Anchoring of material in the liquid crystal phase although well known, is a useful effect for nanoscale changes within bulk material. Earlier in this section, I discussed two different liquid crystal phases, nematic and smectic, exhibiting alignment at micropatterned surface boundaries. For the nematic system, molecules exhibited strong homeotropic alignment at a rectangular boundary where hydrodynamic flows tuned the materials birefringence. For smectic, the material undergoes spatiotemporal control of liquid crystal defects solely through anchoring in pillar arrays, absent of external forces. These examples of passive liquid crystal phases are emphasized in this dissertation because of how applicable it can be in material science and nanotechnology. Anchoring control in structured fluids is ideal as they are highly tunable and in general can be applied to a wealth of new applications, especially when considering the addition of other additives like carbon nanotubes [37] [38].

2.5   Active nematic microtubule system

Despite the countless examples of passive liquid crystals, active liquid crystal materials have become a large focus in soft matter physics. Unlike passive liquid crystals, where defects annihilate slowly over time, defects in active systems can spontaneously be created where they are driven to annihilation and reform continuously. Many active liquid crystal systems are bio-inspired comprised of bacteria colonies [13] [39] [40] [41] [42] [43], cellular monolayers [44] [45] [46] [47] [48], and subcellular constituents [49] [50] [51]. The system I present is an active nematic protein assembly where the material of this complex fluid is composed of flexible rod-like protein assemblies that align at a critical concentration. The focus of this body of work covers a microtubule-kinesin based system exhibiting liquid crystal properties. Bundled microtubules are capable of spontaneous organization resulting in ordered patterns and defects [52] [53] when the system is confined in a quasi 2D configuration. This confinement is like that of planar anchoring as the nematic is confined to the boundary between two immiscible fluids, water, and oil. To facilitate the alignment of the microtubules, polyethylene-glycol (PEG) is used as a depletion agent resulting in the bundles to further concentrate. For imaging, the microtubules are fluorescently labelled microtubules using Alexa Fluor 647.

This system follows the criteria of active matter as it is energy driven and the material carries out collective motion in 2D from the consumption of energy. Spontaneous motion is a direct result of ATP hydrolysis as kinesins bound on the microtubules walk and push on filaments collectively [53]. As the kinesins walk, the filaments move past each other exhibiting extensile motion. $q = +1/2$ and $q = -1/2$ defect charges dominate the surface area as these disclinations are the most stable when no other external forces are applied [53]. In this section, I will discuss the protein assemblies associated with this system, the foundational research leading to its creation, and the methods involved.

2.5.1   Macromolecular assemblies

The system under investigation for this work is comprised largely of macromolecular proteins assemblies. Microtubules and their associated motor proteins serve as nature's nanomachines where they participate in active transport of material across a cell when in

the presence of available ATP in its microenvironment. Understanding the kinetics of this system is important because it is the basis of the forces that cause the collective motion of the active nematic.
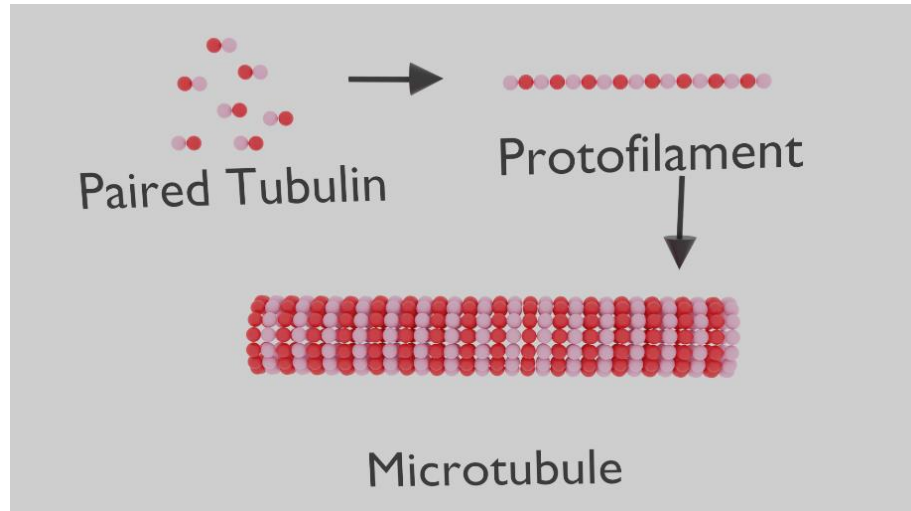
Figure 2.5.Illustration of microtubule regulated assembly of paired tubulin subunits, proto-filaments, and a microtubule.

2.5.2   Tubulin polymerization

Organic living systems are composed of assemblies of protein chains comprised of folded amino acids. These folded amino acids are polypeptide chains that can be thought of as long polymers where each peptide subunit serves as a monomer with some differences in physical properties. An interesting example of macromolecular protein assemblies are microtubules. Microtubules are the most rigid of cytoskeletal elements typically having a diameter of 25nm that can grow to a length as long as the cell they inhabit [54]. Microtubules form an interior network of structural beams that help maintain the integrity of its host cell, resisting deformations as well as serving as a highway to move cell organelles. The role of microtubules within living organisms serves as a direct track to move organelles and other necessary constituents for the life of a cell where it is vital for its function.

Microtubules play a crucial role in active transport within living organisms and are one of the three major classes of protein filaments. Microtubules have also been the subject of a broad range of research not just in cell biology, but also in material science. One study that describes and models the nucleation of microtubules has been reported by McIntosh et al. [55]. It is described as a cylindrical structure in which tubulin heterodimers are packed closely around a central core or rather a structure being built from 13 linear protofilaments with alternating α and β tubulin subunits, bundled in parallel [55]. The conventional idea of nucleation of a microtubule begins at the tip where tubulin dimers (α-tubulin and β-tubulin) alternate positions. At the start, the alternate tubulin forms a cyclic ring; as the length of the microtubule increases, proto filaments at the end begin to curve and increase

in length individually [55]. Furthermore, when the proto filaments increase in length, they fluctuate more rapidly in their later stages of the nucleation [55]. The α- and β-tubulin dimers used to form the microtubules are bound together through guanosine triphosphate (GTP) where the β-tubulin exposes the plus end of the microtubule while the α-tubulin exposes the minus end. This creates an alternating polarity of charge allowing for steady longitudinal growth along the filament and protofilaments. Once a dimer is incorporated into the microtubule, the molecule of GTP bound to the β-tubulin subunit will hydrolyze into Guanosine diphosphate (GDP) through inter-dimer binding. Building on this, GTP determines the bond of the dimers while the GDP determines the stability of the microtubule filament.

The conventional idea of microtubule growth conveyed in McIntosh's work is that microtubule nucleation is enhanced and stabilized through Brownian motion as GTP-tubulin polymerizes while GDP-tubulin does not [55]. The strength of the GTP-tubulin to GDP-tubulin hydrolyzation, both lateral and longitudinal bonds are weakened [55]. The weakening of these bonds during nucleation resulted in proto filaments to fluctuate describing the motion as Brownian [55]. Laterally, the protofilaments would increase in length as the microtubule nucleation continues. To maintain stability, the curvature of the proto filament would increase then would begin to rapidly vibrate, causing it to straighten from being curved to eventually form a lateral bond [55]. With enough time undergoing these fluctuations, the growing proto filaments would be able to straighten, grow then stabilize, allowing the tubulin to add itself to the growing microtubule and elongate proportional to the concentration of tubulin available in the suspension [55]. In short, microtubule growth is facilitated through Brownian fluctuations of their respective proto filaments. As the microtubule begins to nucleate, lateral bonds are much more likely to break and move randomly until the proto filaments would curve more, rapidly vibrate to increase the chance for them to grow, straighten and eventually stabilize forming a lateral bond.

2.5.3 Kinesins

Microtubules serve as both tracks and girders to allow for active transport of mobile proteins and for the structural integrity of the cell. Motor proteins are ubiquitous in living systems where there are many involved in active transport. Of the many examples of motor proteins that walk across cytoskeletal filamentary proteins, kinesins are the most reported with the active nematic microtubule system. Vesicles and organelles bind to the tail of the kinesin, while its head groups bind to the microtubule to move these components across the cell. Kinesins supply motive force to move organelles, vesicles, and chromosomes (particularly in cell division) [54]. The process of a microtubule hydrolyzing ATP to walk can be described using enzyme kinetics (Figure 2.6). When enzymes and substrates are suspended in solution, the enzyme binds with the substrate at a kinetic rate of $c_s k_1$. This process can be reversible denoted by k_{-1} but for the active microtubule system, we can assume that it is not very likely as it has a bias to towards the plus end. The enzyme creates/converts the substrate into the product where it is released at a kinetic rate of k_2. In a short time interval dt, the probability P_E to be in the enzyme state E, can change in three ways: 1) If the enzyme is originally unbound, it will have the probability per unit time $k_1 c_s$

of binding substrate and leaving the state E, 2) If the enzyme is initially in the enzyme-substrate state ES, it has probability per unit time k_2 of processing and releasing product, hence reentering the unbound state E, and 3) The enzyme-substrate complex also has probability per unit time k_{-1} of losing its bound substrate, reentering state E. In short, kinesins walking across a microtubule depends on the binding of its head groups cyclically by consuming ATP.

$$E + S \underset{k_{-1}}{\overset{c_s k_1}{\rightleftharpoons}} ES \overset{k_2}{\rightarrow} E + P$$
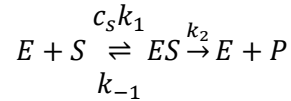
The Michaelis-Menten rule displays the saturation kinetics of kinesin movement. At high substrate concentrations, there is a delay in escaping from the enzyme-substrate complex and thus modifies the velocity as the velocity continues to increase with increasing c_s, however it will never exceed v_{max}. The Michaelis-Menten rule is used to tune the velocity of the active nematic by adjusting the ATP concentration.
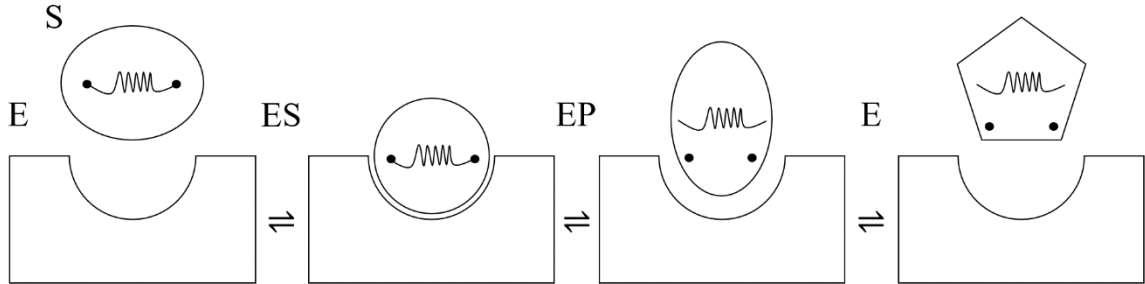
Figure 2.6. Illustration of simple enzyme kinetics serving as an analogue to explain the walk of a kinesin motor protein on a microtubule filament. In this illustration, S = Substrate, E = Enzyme, and P = Product.

The movement kinesin across a filament requires an energy source to carry out the motion. In this case, ATP that is present in the environment is consumed to exert a small force

along the microtubule. The hydrolyzation of a single ATP molecule result in a single step completing one cycle where the next step restarts the process all over again.

From Figure 2.7, the ATP cycle describing a single step taken by a kinesin protein can be visualized. Initially, the motor protein is suspended in solution with a microtubule filament within its proximity. The cycle starts with one head binding to the microtubule causing the release of ADP. The bound head binds to ATP from the solution causing the neck linker to dock its head, biasing the direction of one of the head groups to move in the plus direction. There is a weak energy landing to allow the unbound head to pass over the other head, letting the unbound head to be thrown over and with a high probability to bind to the next surface site on the microtubule filament. The forward head releases its ADP and allowing it to bind firmly to the microtubule where the stretched tether is under sustained strain. At this point, both heads are now bound. The rear head splits off its ATP releasing a phosphate which weakens its binding to the filament and is released from the filament causing the cycle to repeat completing one ~8nm step at the cost of one hydrolyzed ATP [54].
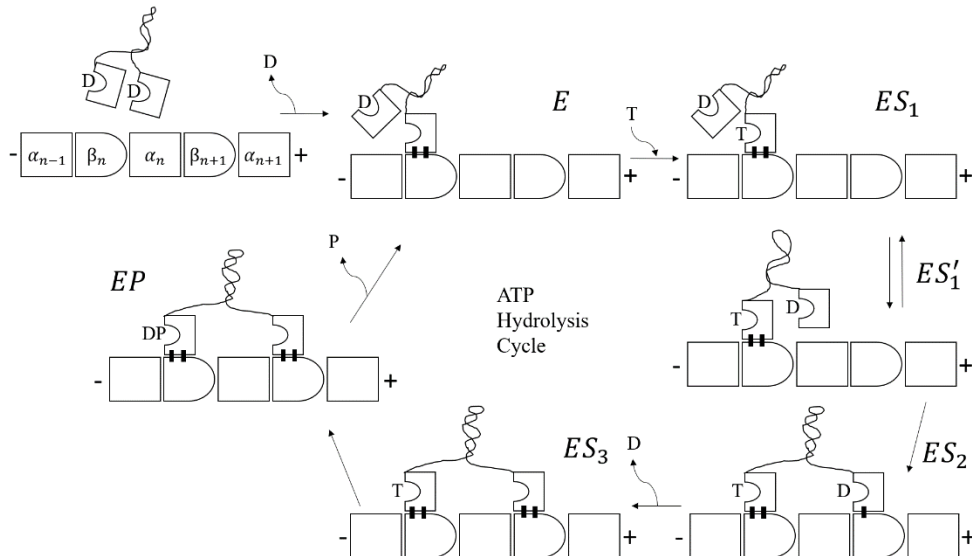
Figure 2.7. ATP hydrolysis cycle allowing kinesin motor proteins to walk along a microtubule. In this illustration, the symbols T = ATP, D = ADP, P = inorganic phosphate.

2.5.4 Depletion Forces

Depletion forces are attractive forces where diffusive smaller particles push together larger particles in a solution. These smaller particles, referred to as depletants, help facilitate the aggregation of larger particles through thermal motion. While in a solution, the particles in solvent are subject to Brownian motion where the components of the suspension randomly diffuse and fluctuate. If considering a particle with a defined radius diffusing through an aqueous medium, the Einstein relation can be used to describe the motion of the particle:

$$D = \frac{k_B T}{6\pi\eta R}$$

In this expression, D is the diffusion constant, T is the temperature of the solution, η is the viscosity of the medium, and k_B is the Boltzmann constant. Polyethylene Glycol (PEG) serves as the depletant that facilitates the bundling of microtubules in solution. Although PEG is a chain polymer, in free solution, it coils into an entropically maximized globular state. The polymer chain can be described as a suspended particle with its size being characterized by its radius of gyration, R_g:

$$R_g^2 = \frac{1}{N} \sum_{i=1}^{N} < |r_i - r_c|^2 >$$

From the above expression, N is the number of monomers or segments on the polymer chain, r_i is the ith segment of the chain, and r_c is the position vector to the center of mass of the coil. In solution, when two filaments are within proximity of each, smaller particles (PEG) collectively collide with the microtubule pushing them closer together. When the microtubules get close enough, there will be a small overlap where the PEG molecules can no longer fit. Eventually, the PEG force the cytoskeletal filaments together, where they are bundled together (Figure 2.8).
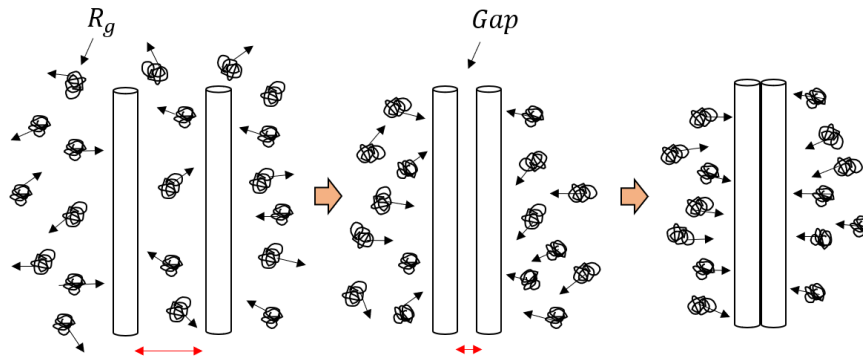
Figure 2.8. Illustration of depletion forces pushing two microtubule filaments together. Globular polymers act as depletants while making isotropic collisions with the larger microtubules. When two of the cytoskeletal filaments come in proximity, the PEG polymers push the protein assemblies closer together where overtime, the gap becomes smaller than R_g, preventing the depletants from coming between them. Eventually, the filaments are firmly bundled together.

2.5.5 A Microtubule/Kinesin based active nematic

Self-assembled cellular structures exhibit a dynamic interplay between many biochemical regulatory processes. It has been discussed in section 2.5.1 that self-organization of molecular assemblies provide a variety of protein structures that are responsible for the regulatory machinery for the function of cellular processes. Active nematics utilizes these regulatory processes to create a new assembly of proteins that exhibit extensile dynamics that generate internalized flows. This new way to assemble proteins, uses kinesin and microtubules to form another microtubule configuration of asters, which was first reported by Nédélec et al [52]. In Nédélec's work, multiheaded motor protein constructs are capable of assembling microtubules in different configurations by tuning kinesin concentrations in a homogeneous solution to form dynamic asters. Nédélec demonstrates that by adjusting these kinesin concentrations, different microtubule assemblies can be formed ranging from asters to microtubule spools. The microtubules are bound together by biotin-streptavidin linked kinesin that move when ATP is consumed, resulting in collective extensile motion of cytoskeletal filaments.
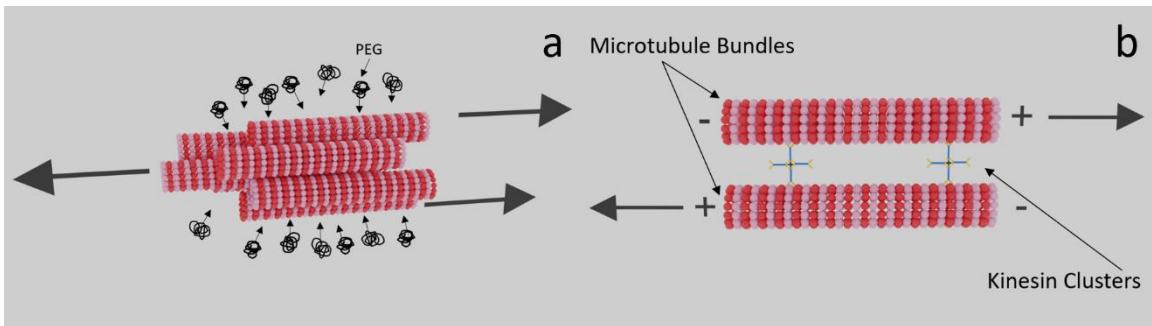
Figure 2.9. 3D Illustrations of (a) microtubule bundles subject to depletion forces by globular PEG polymers and (b) kinesin clusters resulting in two microtubules in the bundles to exhibit extensile motion.

The isotropic gel is composed of randomly crosslinked microtubules using streptavidin bound kinesins largely accumulated at the center of the asters. Nédélec reports that by incrementally increasing kinesin concentrations, different aggregations are realized; for low motor protein concentrations ($< 15 \mu g\ ml^{-1}$), lattice vortices form creating, spool like microtubule assemblies. At slightly higher concentrations ($\sim 25 \mu g\ ml^{-1}$), a combination of vortex lattices and asters take form. At $\sim 37.5 \mu g\ ml^{-1}$, only asters will exclusively form. Finally, microtubule bundles will form at $\sim 50 \mu g\ ml^{-1}$ [52]. Furthermore, circular geometrical constraints were also examined for this study. They report that as microtubules begin to polymerize in the confined circular well, asters will initially form at the center of the chamber. As the length of the microtubules increase, they buckle causing the asters to destabilize. As the asters become unstable, the plus ends at the center break apart resulting in a vortex structure, where the minus ends align the boundary walls [52]. By making subtle tweaks in kinesin concentration and nucleation lengths of microtubules, divergent protein ensembles can be observed at specific ionic conditions.

Nédélec's work served as a foundation for the spontaneous hierarchal assembly of active matter [53] [52]. The work reported by Sanchez et al builds on the efforts of microtubule/kinesin assemblies to create a dense active nematically aligned system that generates internalized flows [53]. With higher microtubule and kinesin concentrations, internally driven chaotic flows, hydrodynamic instabilities, and enhanced transport of matter is demonstrated [53]. Similar to Nédélec et al, microtubules are bound together by streptavidin-linked kinesin motor proteins. Streptavidin has four binding sites where the tail end of the kinesin can attach allowing for their head groups to be oriented 180°. The head groups of both kinesins are then able to bind to microtubule filaments, allowing them to be aligned nematically. In an aqueous solution with high concentrations of microtubules and kinesin, large protein bundles will form. To help facilitate the bundling of microtubules, PEG is added to act as a depletant (Figure 2.9a). The rigidity of the microtubules can be tuned by modifying PEG concentrations where higher PEG concentrations result in more stiff bundles [56]. For the system to move, ATP is added to the solution to tune the velocity of the active network as the origin of the motion lies in ATP hydrolysis.

The active system is initially prepared as an emulsion droplet where the network is suspended in solution in 3D. To configure the system so the microtubule bundles are planarly aligned to a surface, the active emulsion is adsorbed at an oil-water interface to produce a highly active 2D nematic liquid crystal system (Figure 2.10). In this confined state, streaming flows are regulated by an interplay of internally generated fractures and self-healing, evident by the continuous annihilation and reforming of liquid crystal defects. Upon inspection, the planarly aligned microtubule bundles exhibit sliding forces due to the collective motion of microtubule-bound kinesin (Figure 2.9b). Velocity of the active system can be tuned with the injection of ATP; however, based on what is mentioned in section 2.5.3, this system is subject to saturation as per Michaelis-Menten Kinetics.
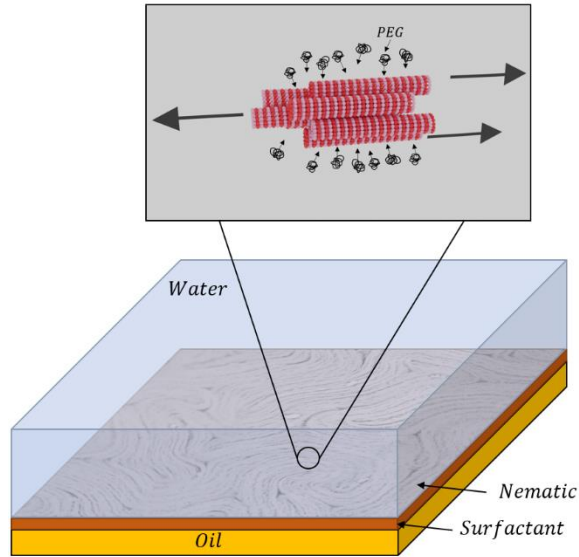
Figure 2.10. Bundled microtubule-kinesin assembly planarly aligned and confined between two immiscible fluids. Kinesins bind to streptavidin, allowing the filaments to nematically align. Figure was inspired by DeCamp et al [6].

The characteristic motion of this planarly confined quasi-2D active nematic has been subject to large amounts of work to interpret its kinematics quantitatively and qualitatively. The motion of active material has been described in a number of ways ranging from having straight baths to turbulent [30] [53] [57] [58] [59]. Sanchez describes the motion as being capable of exhibiting ballistic motion at ATP saturation as tracked silicon beads move straight from their own experiments [53]. In other work, reported by Tan et al [58], mathematical methods from chaos theory are used to describe mixing and braiding observed in the 2D confined active nematic. Given the turbulent-like nature of this novel system, attempts to probe, organize, and control material trajectories have been a pursued persistently in the field of active matter.

2.5.6   Active length scales

ATP and PEG impacts how defects forms, defect sizes, and active network kinematics. In active nematics, there are two important length scales that are characteristic to their defects; the coherence length and active length scales which can be written as $l_s = \sqrt{\frac{K}{A_0}}$ and $l_a = \sqrt{\frac{K}{|\alpha|}}$, respectively. K is the elastic constant of the bending bundles; A_0 is a material constant and α is the activity constant of the system. The coherence length describes how quickly the nematic order drops off within the vicinity of a topological defect. The coherence length is also used to measure the radius of a defect core as it considers the elastic cost to bend the material, the constituent's size, and temperature conditions [60] [61]. The active length scale on the other hand is the length at which the elastic stresses from bending and active stresses balance. Elastic and active stresses result in spontaneous distortions and flows in

the system. In other words, it is a length scale resulting from the competition between the energy used to bend the material and its rigidity. Active length scales can be measured though mean defect separation, director correlation length, vorticity, and velocity correlation lengths [62]. Such parameters can be tuned by controlling the composition of the active material itself i.e., PEG or ATP concentrations [58]. Recalling from section 2.4.2, we saw a similar interplay between the elasticity of 5CB and hydrodynamic convection flow. Although, the flows are different, parallels can be drawn from these two systems such as 5CB experiencing convection flows and active material exhibiting internally generated flows. Beyond tuning active material composition, we are interested in methods to tune active length scales through changes in viscosities using patterned surfaces. Reported work from Guillomat et al [8] demonstrates changes in defect sizes and kinematics when using silicon oils with different viscosities. I aim to turn our attention to methods from published work to create changes in microenvironments to modify defect kinematics and creation. Some of these methods inspired my published work to create activity gradients by varying the oil thickness at different positions. Such activity gradient can result in a range of active length scales and is another parameter to consider when aiming to control internally generated chaotic flows. These methods involved the creation of simple patterned structures to confine the active material and observing how viscosity can be tuned to influence the active material.

2.6   Active nematic microtubule systems and boundaries

From section 2.5.6, I discussed how length scales define defects in an active liquid crystal. There are many parameters that determine how defects form and how they develop their size. These parameters are activity, rigidity of the bundles, elasticity of the constituents and in this case, the dimensions of the microtubules. I also mentioned how changes in the microenvironment can influence length scales. These changes relate to patterns and confinements that can anchor active material which can result in changes director field alignment. In this section, I will discuss how simple fabricated patterns can organize defect flow patterns and alter their kinematics. Also, I will discuss how viscosity can influence defect length scales.

2.6.1   Cylindrical wells

The active nematic microtubule kinesin bundled system in a 2-D configuration has been a useful experimental setup to study active liquid crystal systems. These protein systems when confined to similar geometrical wells, are subject to circular flows and anchoring. The microfabricated cylindrical wells served as a boundary where the microtubule filaments anchor and align [7]. The cylindrical structures had a range of diameters from strong (smaller diameters) to weak confinements (larger diameters) from 60µm to 800µm. The strongest confinements at 60µm to 100µm, produce vortices and strong parallel alignment to the boundary. These confinements created consistent +1 defects where smaller defect charges, +1/2 and -1/2, are not very likely to form. This could be a consequence of the microtubule bundles being too rigid to bend. Defect charges of ±1/2 are more stable when not too two dimensionally confined making them unlikely to form. Weaker or intermediate confinements still demonstrate strong anchoring at the boundaries of the fabricated surface but since there is more space in the confinement to allow

microtubule bundles to bend, a net defect charge of q = +1, can be observed. This can be seen for intermediate confinements from 100µm to 200µm where +1/2 and -1/2 defects were able to form in an asymmetric doubly periodic spiral configuration [7]. For lesser or very weak confinements, 300µm to 600µm, proliferation of defects was observed, where defect kinematics resulted in bulk 2D nematic flow [7]. From 60µm to 600µm, circular flows along the walls of the geometries have been demonstrated where at 800µm, the active nematic demonstrated turbulent bulk dynamics.
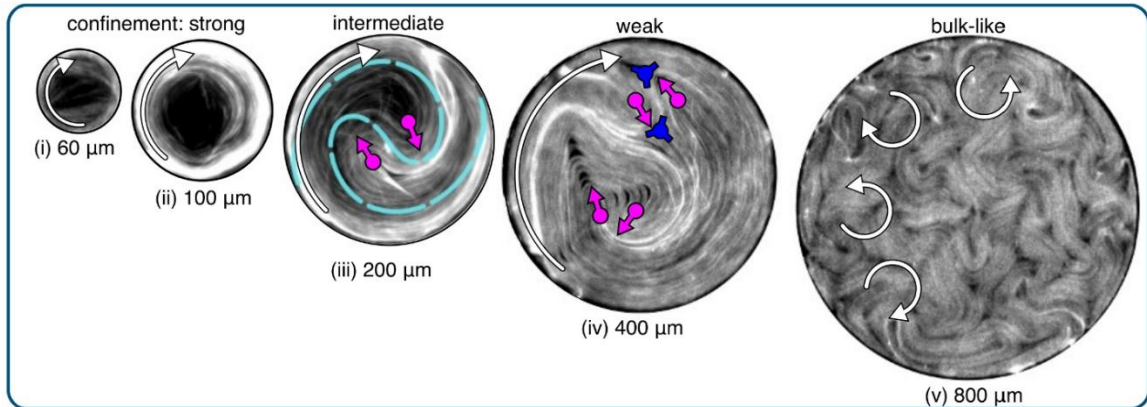
Figure 2.11. Fluorescence images of confined active nematics with diameters of (i) 60, (ii) 100, (iii) 200, (iv) 400, and (v) 800 µm. White arrows indicate direction of circulation. Cyan line overlaying the 200 µm disk highlights the double spiral configuration of the nematic director observed for intermediate confinements. Adapted from Opathalge et al [7] with permission ©2019 Proceedings of the National Academy of Sciences (PNAS).

Opathalage et al. demonstrates transient circular flows of bundled microtubule system [7] (Figure 2.11). Two common but unexplained conclusions were drawn throughout their work: 1) formation of doubly periodic spirals of +1/2 defects can evolve over time and 2) a two-step transition can occur from periodic dynamics to bulk turbulence with decreasing confinement [7]. The two-step transition refers to the transition of circular to bulk flow dynamics of defects at intermediate confinements. This resulted in defects nucleating at the boundary and somewhere midway in the confinement. Opathalage continues that the two possible explanations causing doubly periodic dynamics is the build-up of microtubule density at the boundary of the well inducing the formation of defects due to stress and persistent circulating flows suppressing defect nucleation for stronger confinements [7]. Physical boundaries that trap active material has provided consistent parallel anchoring and circular flow. Using microfabrication to create similar geometries to serve as obstacles instead of wells, may be a viable method to control nematic flow.

2.6.2   Rectangular Channels

The spontaneous nature of active bundled microtubules is an intrinsic property which can be described as chaotic. Flow patterns of 2D active nematics can be characterized in several ways as ballistic, jets, swirls, and braids [57]. From Opathalage, we observed that hard SU-8 circular boundaries with high confinement, result in vortex-like flow patterns, boundary nucleated defects and strong planar alignment [7]. Other simple geometries to encourage

organized flow patterns are possible. Rectangular structures confining active bundled microtubules has been reported both from simulation and experiments [57] [63]. At certain channel widths, different defect dynamics can be observed. Furthermore, both simulations and experiments demonstrated organized flows and interesting braiding trajectories when confined.

Micro-printed geometries reveal consistent motifs regardless of the patterned shape. One motif that appears ubiquitous despite the shape are boundary nucleated defects. For circular boundaries, +1/2 defects nucleate at the boundary, where it moves towards the interior, leaving behind a -1/2 defect stagnating at the wall. Similarly, rectangular geometries produce the boundary nucleated defects, reported by Hardoüin and Shendruk et al [57] [63]. Bending of bundled filaments due to the activity occur at the boundary, causing once planarly alignment bundles to pinch together. Like with circular boundaries, these +1/2 defects move to the interior of the rectangular confinement. In this example, higher defect concentrations of -1/2 defects exist at the boundary where +1/2 defects are not likely to exist at these locations. This is due to the disparity of +1/2 defects that approach the boundary, where they annihilate with bound -1/2 defects.

Another observation is the tendency of +1/2 defects to form net +1 defect charges. These +1 net charges are comprised of two +1/2 defects that swirl around each other until eventually their symmetry breaks or sometimes rarely, form a single +1 defect. For circular confinements, these spiraling defects twirl in place until a bend breaks; for rectangular structures, +1/2 defect are largely distributed midway through the trench where spirals are highly likely to form [57]. As spirals form, +1/2 defects perform a unidirectional motion moving laterally toward the end of the channel. As +1/2 defects pairs travel along the channel, they exchange partners and spiral with other positive defects. This flow pattern resembles a Ceilidh dance where -1/2 defects stagnate at the boundary.

Different trench widths were investigated experimentally by Hardoüin et al [63]. From these different widths, three forms of activities were identified: shear, dancing, and turbulence. For thin trenches, there is more shearing of planarly aligned microtubules appear with channels widths of $w < 80\mu m$. In this regime, Hardoüin et al reports that the microtubules can create a defect free state where bundles exhibit an extensile motion along the boundary [63]. Eventually, an instability takes place at the boundary caused by a local bend creating a sinusoidal shape to form causing defects to nucleate from the wall. For slightly wider trenches of $90\mu m < w < 120\mu m$, dancing of +1/2 defects traveling along the trench can be observed. This creates organized vorticity arrays as the channel can accommodate more than one defect if the width is comparable to the active length scale of a +1/2 defect. Although this experimental finding closely resembles Shendruk's work for the dancing state [57], Hardoüin reports that it is fragile as vortex lattices are more transient and +1/2 defects can annihilate with their -1/2 counterparts [63]. For active material in channel widths of $w > 120\mu m$, turbulent bulk flows form like more open active systems as defect distributions diminish. Although defect distributions were not as pronounced like in the dancing regime, -1/2 were still likely to localized at the wall and +1/2 defect flow towards the center of the channel. Active material near the wall will still exhibit local shear flow where defects nucleate [64].

2.6.3 Viscous effects on active material and friction serving as a boundary

Using engineered confinements has demonstrated to be a useful method to order material in liquid crystal phase and induce defect nucleation and organization with the contribution of a boundaries. This well-known effect of anchoring where the components in the liquid phase align with a boundary, results in the generation of defects that would otherwise be unstable or unlikely in configurations lacking obstacles or boundary. More specifically, vortices have been a consistent motif when material in the nematic phase are substantially confined and when sufficient spacing is available to allow bundles to bend enough to form two spiraling $+1/2$ defects. As components in the nematic phase are exposed to stronger confinements, there is a tendency for the material to reorganize to maximize entropy. In other words, the vortices are net $+1$ defects like the intermediate confinements reported in Opathalage's work [7]; these higher defect charges would otherwise be unstable in less confined simpler configurations where $\pm 1/2$ defect charges are otherwise more stable [63]. From the previous reports such as Wioland [13] or even DeCamp [13] [6], any kind of boundary/interface can serve a surface to anchor liquid crystal material considering that both examples are between two immiscible fluids, not solid photo-plastics like SU-8. Furthermore, consider a 2-D active nematic where there are oil layers with varying viscosities. As indicated by Sagués et al. varying viscosity influences the friction for active nematic flow [30]. As friction is increased, the dynamics of the active nematic are slowed down resulting in lower velocities and a proliferation of defects [30]. The decrease in velocity results in a larger defect population because their annihilation encounters become less frequent [30]. It calls into question if a solid barrier such as the wall of a microfluidic device is the only necessary component for anchoring.

Differences in shear flow between two interfaces is to enough influence defect formation. Changing friction at the oil interface can be used to probe shear flow of planarly aligned bundled microtubules. The introduction of friction to bundled/microtubules has demonstrated how adaptable the active systems can be when changes in their microenvironment occur. Friction dominates the biological world where bacterial suspensions push against each other and at interfacial boundaries. If we consider an active nematic bacterial suspension with high bacteria concentration, radial confinement, steric interactions, and self-propulsion can be observed as introduced by Wioland et al [13]. Persistent single-vortex states can be induced when confining bacteria generating spiraling patterns at an interfacial boundary not necessarily in solid state. Experimentally Wioland et al. created a physical system of an oil emulsion containing droplets of a highly concentrated aqueous suspension of *Bacillus subtilis* [13] with diameters of $\sim d = 30$–$70 \mu m$ and a height $h = 25 \mu m$. The bacteria can be visualized and modeled as a cylindrical rod fitting into the description of a material transition into a lyotropic liquid crystal phase.
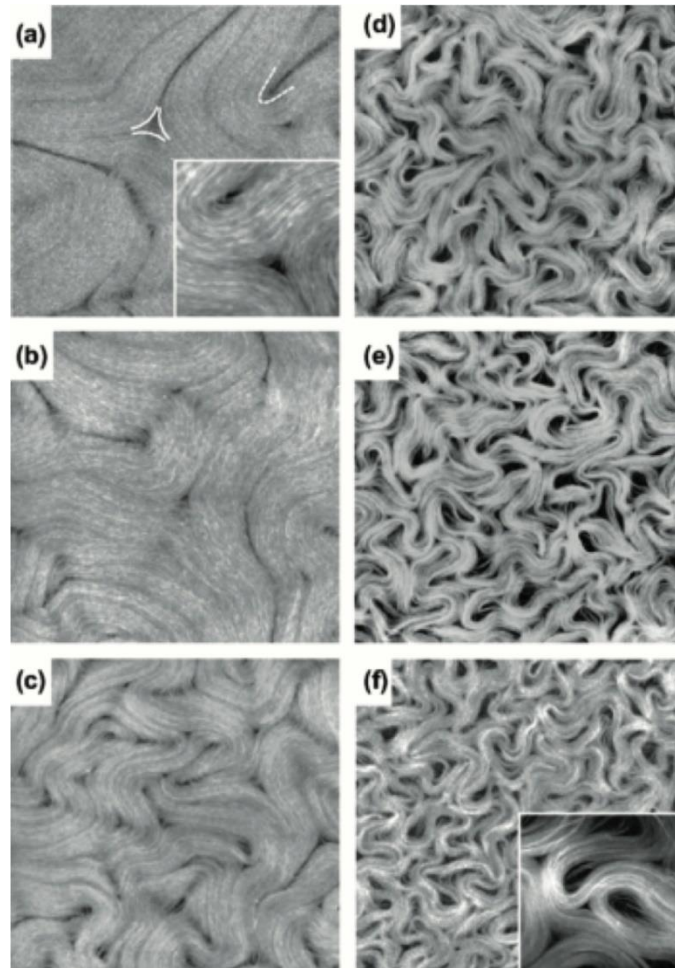
Figure 2.12. Fluorescence confocal micrographs of active nematic in contact with silicone oils of different viscosity with a 400µm wide frame. The oil viscosity range from (a) to (f), is 5 × 10^−3, 5 × 10^−2, 0.5, 5, 12.5, and 300 Pa* s, respectively. Image was reproduced by Guillomat et al [8] with permission ©2016 American Physical Society (APS).

Wioland's work observed that bacterial suspensions are capable of self-organization into a single stable vortex in an isolated droplet where overall bacterial arrangement was reminiscent to rotating spirals. The author states that organization of the bacteria are derived from polar active liquid crystal where the bacterial layer is regarded as a smectic liquid crystal structure while the bulk of the suspension behaves as a chiral nematic phase [13]. Furthermore, the microscopic hydrodynamics at the boundary of the oil droplet must be considered as backflow where the source is from the bacteria itself when they exhibit extensile motion pushing back onto each other to make their circular motions along the boundary. This suggests that conditions at the boundary must be considered as they result in the stabilization control and order the active microbial systems [13].

More pertinent to bundled microtubules, viscosity influencing active material has been demonstrated by Guillomat et al by using silicon oils with different viscosities [8]. From Figure 2.12, Guillomat probed shear viscosity of in sequential five orders of magnitude. Expectedly, network velocity substantially reduces with increasing viscosity (Figure 2.13) [8]. It was found that defects proliferate at higher viscosities. These higher viscosities result in larger rates of defect creation; as the network velocity is substantially reduced and as a result, the defect annihilation event rate is also reduced. In short, Guillomat et al experimentally demonstrates the dramatic changes in defect morphology and network kinematics when changes of viscosity in the oil interface occurs [8]. We will discuss later other methods for spatial activity differences using patterned surfaces.
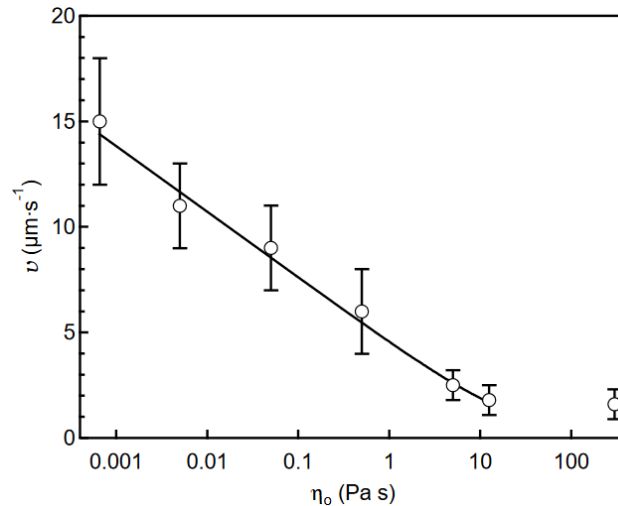
Figure 2.13. Average speed of +1/2 defects as a function of oil viscosity [8]. Image was reproduced by Guillomat et al [8] with permission ©2016 American Physical Society (APS).

2.6.4   Influencing active material using anisotropic sublayers

From section 2.6.3, I discussed that planarly aligned active bundled microtubules are affected by viscous isotropic oils. Anisotropic fluids can also influence particles as nanoparticles have been dynamically assembled using cholesteric liquid crystals reported by Li et al [65]. It is demonstrated that using the liquid crystal phase can collectively organize nanoparticles within the bulk into core-shell morphologies. Anisotropic fluids can also influence active particles at the interface as well. Examples to modulate active nematic flow using anisotropic fluids at the interface has been reported by Guillamat et al [66]. Bundled active microtubules confined at the interface of 4′-octyl-4-biphenylcarbonitrile (8CB) can be softly contained and form net +1 defect charges. This is possible because 8CB form circular conical domains at the interface where microtubule bundles curve and align transiently at the inner boundary. Confinement and circular trajectories depended on concentrations of ATP, PEG, and domain diameters. These findings reveal the adaptability of bundled microtubules and the efficacy of modifying the subjacent fluid to induce soft or virtual boundaries to impact collective motion. The advantage of using anisotropic fluids

provide the advantage of dynamically changing the sublayer to influence planarly alignment active nematics even with electromagnetic fields [67]. There is a lot of potential to control particles using lyotropic suspensions by changing their microenvironment, even at the interface. In general, structured fluids can be used to assemble nanoparticles that would otherwise be randomly dispersed in an isotropic medium.

2.7 Conclusion

In Chapter 2, I have covered what complex or structured fluids are and how ubiquitous they are in everyday life and in research. Complex fluids can be mixtures of several components (colloids, protein assemblies, etc.) or comprised of one kind of molecule such as 5CB. The most fascinating characteristic of these fluids is their ability to self-assemble and organize into often symmetrical structures that serve a vital function in nature. These functions can be both temperature (thermotropic) and/or concentration (lyotropic) dependent as these conditions impact the structure of the material.

In this Chapter, we also went over both a qualitative and quantitative analysis of how structured fluids organize. When exposed to an external force, there are competing factors between what is being applied and the intrinsic elastic properties of the material. These materials have exhibited novel properties when introduced to different forces. Under specific conditions, molecular alignment occurs resulting in anisotropic properties to manifest, as different properties can be measured depending on where the material is being probed. These properties can be optical, mechanical, or electrical. We noted that these materials are everywhere in electronic manufacturing, more specifically in LCDs.

Because this thesis is largely focused on alignment and organizing material, we discussed different studies and publications demonstrating how the anchoring of a material in liquid crystal phase can influence long range alignment. For passive liquid crystal phase, we discussed nematic liquid crystal (5cb) in rectangular fluid devices and smectic liquid crystal phase (Smectic A) exposed to cylindrical pillars arrays. Both examples discussed in this chapter demonstrated how micropatterned structures can promote nanoscale alignment via homeotropic alignment at their respective surfaces. Despite both works focusing on two different liquid crystal phases and surface patterns, consistent motifs can be identified: longer range alignment along the surface, positionally controlled defects and consequential changes in physical properties due to material alignment. The methods proposed in these works motivated us to apply these patterned geometries to active nematic protein assemblies.

Towards the end of Chapter 2, we discussed the active nematic protein microtubule/kinesin assembly in focus for this work. The system is a lyotropic active nematic system composed of microtubules bundled together by their microtubule associated protein (MAPs), kinesin motor proteins. When exposed to an energy source (ATP), kinesins can collective walk along the protein filament resulting in macroscopic internally driven flows. To create a continuous layer to observe defect creation and annihilation, the system is confined between two immiscible fluids creating a quasi-2D active gel between these two interfaces. This system has been heavily studied where this active nematic network has been probed in microfluidic devices and different oil viscosities, which I have covered. I have also

discussed that soft boundaries induced by anisotropic fluids is possible and that these structured fluids result in organized flows. From these works, we developed our own methods to produce our own microfluidic fluidic devices, geometric patterns, and alternative methods of confinement.

Chapter 3: Methods – Creating active nematic gels, patterned surfaces, and surface treatments

3.1   Introduction

Active nematics have recently risen to prominence in the field of soft matter and one of the most interesting examples is the recently developed biopolymer-based active nematic formed from bundled microtubule filaments in the presence of cross-linking kinesin motor clusters [53]. Active nematics consist of energy-driven anisotropic elements to carry out collective molecular motion driving internally generated flows. In this phase, defects can spontaneously arise, move around, braid, annihilate and then reform. In this case, the biopolymers are driven and bundled by the motor proteins powered by ATP hydrolysis. Several experimental methods have already been developed using the bundled microtubules [30] [7] [63] [57]. Furthermore, theoretical, and computational models have been reported describing defect dynamics, pattern formation, and methods to mathematically characterize this novel system [58] [57] [68] [69] [70] [71] [72]. With the use of microfluidics, we aimed to build on Sanchez' results by creating complex surfaces and to observe their influence on defect behavior and active kinematics [53]. Chapter 2 emphasized that the incorporation of new surfaces or immiscible boundaries adds more complexity to an active nematic system [70] [73]. I will discuss methods and preliminary work to expand more on the effects of anchoring on bundled microtubule active nematics on patterned surfaces.

Molecular anchoring in a liquid crystal phase refers to the imposed orientation of the liquid crystal director, $\vec{n}$ with respect to a boundary, surface, or interface [28]. When a confining surface induces an anchoring condition, there may be some conflicts between the intrinsic molecular ordering of the phase, their elasticity, and their tendency to align with the container boundary. This interplay of steric molecular interactions and elastic energy minimization can inevitably lead to topological defects depending on the specific geometry of the containing surface [28]. In the active bundled microtubule system, we observe planar microtubule anchoring since the active nematic is confined at the flat two-dimensional boundary between oil and aqueous fluid layers which was reported by Lemma and DeCamp et al [6] [74]. In a passive nematic phase in two dimensions, without confining boundaries, no defects are topologically required, however they may occur when introduced to stress, fields, or even spontaneously. In an active nematic we see the emergence of pairs of topological defects (+1/2 and -1/2) that braid around one another, continually annihilating and reforming. This is the simplest example of how anchoring can be used to promote organizing an active phase and defect formation. In this Chapter, I will discuss methods to create the active nematic gel, surface treat substrates, and fabricate microstructures.

3.2 Experimental Methods

3.2.1 Preparation of Acrylamide Brush Coverslip

Hydrophilic coverslips were prepared with an acrylamide coating. Clean the coverslips thoroughly with soapy water, ethanol, and 0.1M NaOH with alternate rinses using nanopure water. Once rinsed, coat the coverslips with a silane solution composed of 100mL ethanol, 1mL acetic acid, and 500µl 3-(trimethorylsilyl) poroplymethacrylate (Acros organics) for 15 minutes, then rinse with nanopure water. Prepare an acrylamide solution from 95 mL nanopure water and 5mL 40 wt % acrylamide (company), then degas the solution for 30 minutes in a vacuum oven. Add 0.07 g of ammonium persulfate and 35µl Temed. Pour the acrylamide solution over the coverslips while face up and incubate overnight at room temperature.
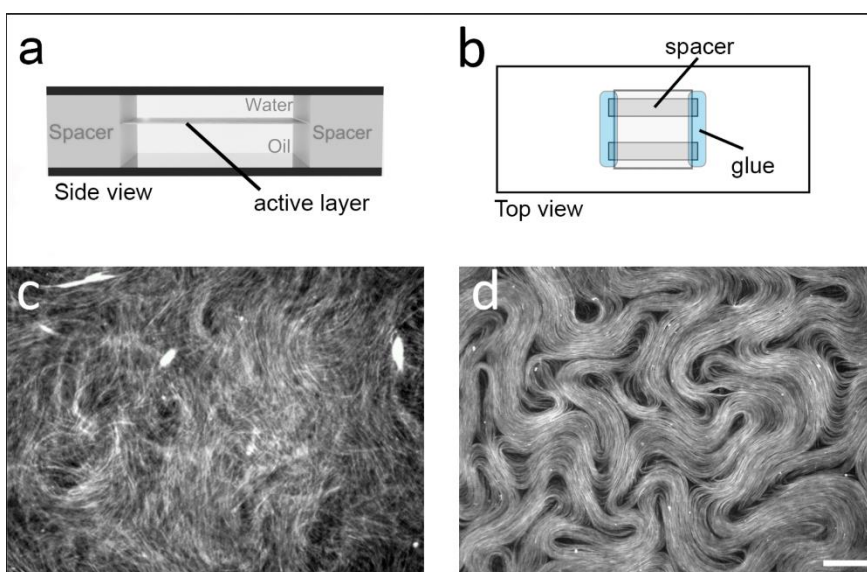
Figure 3.1. (a) Cross section schematic of the flow-cell geometry. (b) Top view schematic of the flowcell. (c) Typical appearance of the active solution before assembly at the oil/water interface. (d) Active nematic assembled at the oil/water interface.

3.2.2 Formation of bundled active nematic network

The microtubule/kinesin-based active nematic was formed by previously described methods. 7µl aliquots of active premixture containing biotin-labeled K401 kinesin motors, streptavidin, PKLDH and phosphoenol pyruvate (PEP) (an ATP regenerating system), an antioxidant solution to prevent photobleaching containing 6.65mM DTT, 4mg/ml glucose, 0.27 mg/ml glucose oxidase, 47µg/ml catalase and 2mM Trolox, and 6% (w/v) 20kD polyethylene glycol (PEG) in M2B buffer (80mM PIPES pH 6.8, 2mM $MgCl_2$, and 1mM EGTA) were prepared as described in [53] [58]. These experiments were performed at kinetic saturation with 1mM ATP (final concentration) being added to the premixture. 2µl of 6mg/ml (3%) Alexa Fluor 647 labeled GMPCPP microtubules are added to the premixture (for a final concentration of 1mg/ml). For fluorescence imaging, microtubules

are fluorescently labelled with Alexa Fluor 647 [53]. This system forms a 3D, unconfined, active microtubule network where only microtubule bundles are observed. Streptavidin can bind up to four biotin-labeled kinesin molecules and when microtubules of opposing polarities align parallel to each other, the kinesin molecules oriented at 180° to each other walk in opposite directions along neighboring microtubule filaments. As the kinesins walk, the filaments perform an extensile motion driven by ATP hydrolysis. We used an ATP concentration at saturation (i.e., the local microtubule extension speed is maximized) and tuned network velocity by adjusting these concentrations.

To confine the active nematic, we followed a previously published procedure [53] [58] [6] to confine the material between two immiscible fluids. We first created a fluidic device comprised of a glass substrate with patterned structures, double-sided adhesive spacers and a coverslip treated with a polyacrylamide brush which prevents excess protein binding to the coverslip. We flow in an oil/surfactant mixture (3M HFE7500 with 1.8% PFPE-PEG-PFPE (perfluoropolyether) surfactant) into the channel first, then we flow in the active microtubule network. The ends of the flow cell are sealed using a UV-curable glue (RapidFix). The sample is then centrifuged in a swinging bucket rotor for 10-15 minutes at 1000 rpm would suffice to confine the active material.

3.2.3 Fabrication of geometries using photolithography

Photolithography is viable method to develop micro- and nano- patterned structures for wide use of applications. I used lithography methods to create microscale geometries for this study [75]. Pillars were fabricated using a negative tone epoxy-based photoresist, SU-8 (MicroChem Corp.) (Figure 3.2a). Prior to fabrication, glass substrates are thoroughly cleaned in soap and water followed by 30-minute sonication periods in acetone, methanol, and ethanol. The glass substrates are rinsed in nanopure water then dried using nitrogen gas. To thoroughly remove any residual particles and thus improve film adhesion, the glass substrates were plasma treated with oxygen for 2 minutes. The glass substrate is placed on a hotplate for 5 minutes at 150°C then is cooled down to room temperature for 5 minutes in a humidity-controlled area to remove any residual moisture that may have accumulated on the substrate after plasma cleaning. A quarter-sized drop of SU-8 2010 is deposited on the glass substrate for spin coating where it is spun at 1000rpm for 45 seconds. The substrate is then soft baked at 65° for 10 minutes then at 95° for 30 minutes on a hotplate to evaporate the remaining solvent in the film. The film was exposed to 365nm UV light (150mJ/cm^2) to release acids from photoacid generators (PAGs) (Figure 3.2) then underwent a post exposure bake (PEB) for 5 minutes at 65° then for 10 minutes at 95°on a hot plate to allow the epoxy groups to crosslink, creating a transparent plastic film. The hot plate is turned off with the substrate still on and allowed to cool to room temperature; removing the film quickly off the hotplate can thermally shock the film, causing stress and then cracks. Once cooled, the substrate is developed in SU-8 developer for 30 minutes with gentle agitations. Once developed, residual SU-8 developer is rinsed away with isopropanol and de-ionized water then dried with nitrogen gas. The thickness of the microstructures was verified using profilometry. A basic schematic of the process flow is visualized in Figure 3.2c.

3.2.4 Photolithography
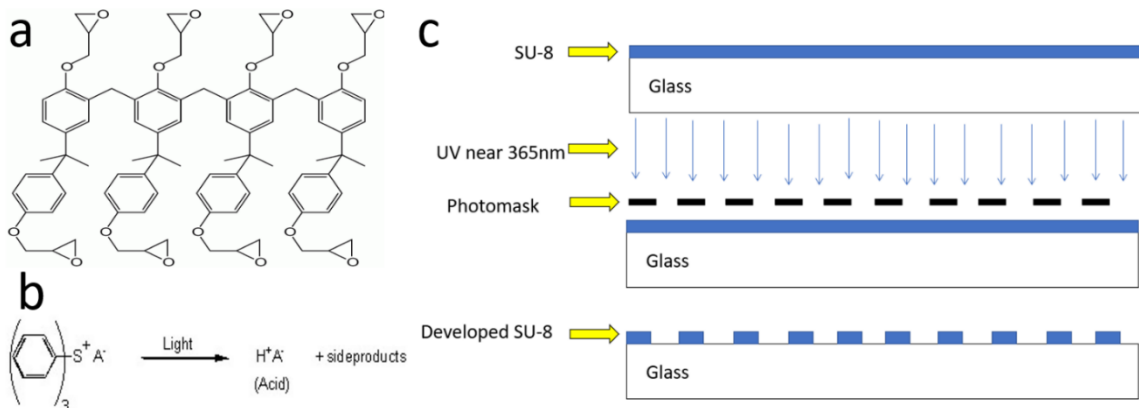
Figure 3.2. (a) Illustration of a SU8 monomer. (b) Illustration of reaction of a photoacid generator (PAG) releasing an acid when exposed to UV light. (c) Process flow diagram illustrating a single exposure process using a negative tone photoresist.

A simple example of a single-patterned fabricated structure is illustrated in Figure 3.2c and protocol in the previous section. The type of wafer depends on the application, but for our system, we use glass as a substrate for our structures because the device should be transparent for fluorescent microscopy. The resist is spun down creating a thin uniform coating onto the substrate where thickness depends on the spin speed. In both research and industry, there are two types of photoresists in lithography based on their tones, negative and positive. The tone is based on their photochemistry when exposed to 365nm of ultraviolet light. One of the properties of photoresists is their photosensitivity. When exposed to ultra-violet light (in this case 365nm), photoacid generators (PAGs) release acids from within the film. The polymer and PAGs are suspended in a solvent, thus they are distributed evenly throughout the exposed cross-section of the film. When heated, the acids effect the film's solubility where two different outcomes can arise depending on the tone. If the film is positive tone, the PAGs break up the polymer, changing it from insoluble to soluble in aqueous solution. If the film is a negative tone resist, the acid released from the PAGs result in crosslinking, producing a change from soluble to insoluble in aqueous solution, leaving behind a thin plastic film.

SU-8 is an epoxy-based negative tone photoresist that can create thin plastic substrates upon exposure and development. It has a wide range of applications in bio-medical devices, cell encapsulation and microfluidics due to its biocompatibility. SU-8 comprises epoxy-based monomers suspended in solvent and PAGs. Upon exposure to ultra-violet (UV) light, the PAGs release acids which serve as a catalyst for the cross-linking reaction. Once the PAGs are released, the film is exposed to a 95°C post exposure bake (PEB) and the acids induce cross-linking of epoxy groups in the film.

The PEB facilitates cross-linking within the SU-8 layer, which is why this is a crucial step to avoid unnecessarily causing stress in the film. Heating the film above its glass transition temperature ($Tg = 55°C$) increases the molecular diffusion of monomers and PAGs resulting in an increased cross-linking rate. It is important to emphasize that extensive

cross-linking affects the mechanical properties of the film as the network will become stiffer and thus potentially brittle. The PEB should be handled with care as to avoid thermally shocking the film and poor adhesion especially for thicker structures. Typically, slowing ramping down the temperature before removing the device from the hotplate can substantially reduce stress. During the development step, the exposed regions remain on the substrate as the cross-linking affects the films solubility in that specific region.

Adhesion of SU-8 on a substrate is an important factor for device production. Substrate to film interaction, substrate cleanliness, film thickness and surface preparation must be considered prior to fabrication. The presence of impurities, moisture, and other residual coatings can greatly compromise adhesion resulting in leaks, cracks, and warps, at the substrate-SU-8 interface affecting device performance and functionality [76]. Glass substrates must be cleaned thoroughly in soap and water followed by sonication for 30 minutes in Acetone, methanol, ethanol then rinsed in nano pure water to ensure minimal presence of surface contaminants. To ensure that the surface is thoroughly clean, the surface is plasma treated with oxygen for 30 seconds. To ensure the removal of residual moisture, glass substrates are placed on a 150-200°C hotplate for 5 minutes and allowed to cool down for 5 minutes at room temperature.
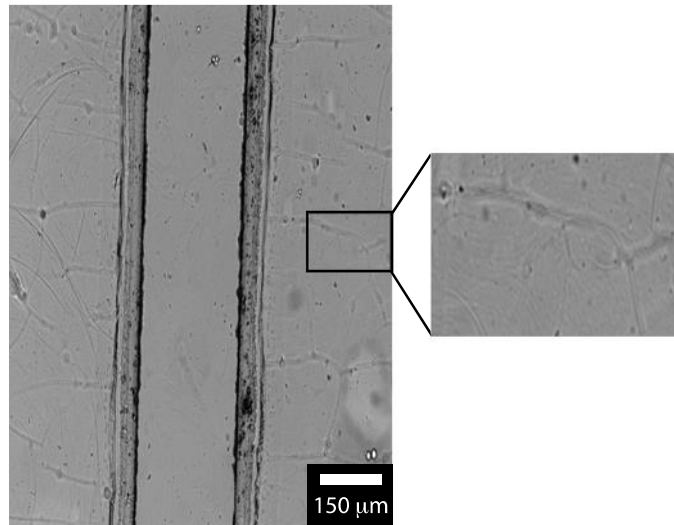
Figure 3.3. Bright field microscope image of a microfabricated thick SU-8 trench. The inset image highlights cracks in the polymerized surface due to rapid cooling.

Film thickness should be carefully considered when designing substrates. Thicker films tend to be highly stressed resulting in cracks, warping of the features and poor adhesion (Figure 3.3). For thicker resins such as SU-8 50, we used gradual cool downs to room temperature after the PEB and a hard bake at 150°C for 2 minutes post development. These steps greatly improved adhesion, resolution of the film pattern, and reduced cracking.

3.3 Results

3.3.1 Role of confinement and anchoring in active nematics
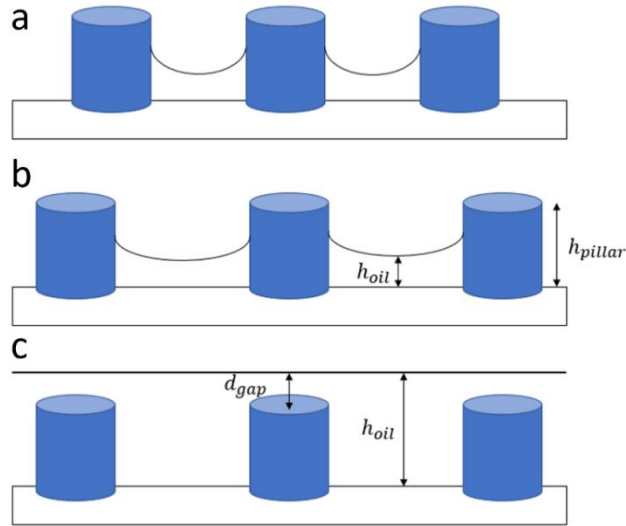
Figure 3.4. Illustrations of several oil layer configurations with fabricated SU-8 pillars. (a) SU-8 pillars with a height greater than the thickness of the oil layer. The smaller separation distance results in high interfacial curvature at the oil/water boundary layer. (b)A similar configuration to (a) but with a larger separation distance between pillars resulting in a larger radius of curvature. (c) SU-8 pillars with a height less than the thickness of the oil layer, i.e., submerged in the oil layer.

I was motivated from previous works presented in Chapter 2 to apply microfluidics with patterned geometries to organize director orientation, spatially position defects, and control defect trajectories. This led us to pursue the goal to design and construct microfabricated surfaces in a transparent fluidic device that can be used to investigate the effects of confining geometries on active flows [77]. Using the cylindrical geometries like in Opathalage's work, but as pillars, not wells, we demonstrate the effects of circular pillars in this section [7]. The arrangement of these pillars acts as circular boundaries within the active layer in the x-y plane. Because these pillars protrude out of the oil and penetrating the active nematic layer, wetting behavior of the oil/water interface on the pillars leads to additional curvature-based effects on the z-axis. Figure 3.5 shows a fluorescence microscope image of active nematic surrounding two circular SU-8 pillars. For these pillars, we observed several -1/2 topological defects bound and distributed around the pillars. These defect points tend to persist and remain relatively immobile as the rest of the active layer flowed around the pillar geometries. This persistent defect radial defect distribution is like that seen in linear channels [63] [57], and future work should explore how different geometrical shapes arrange persistence of defect points.

Investigation into active nematics has been largely focused on flat interfaces, but by designing pillar arrays and channels with the right wetting properties, it may be possible to produce interesting, curved interfaces between immiscible fluids. For example, if $h_{pillar} > h_{oil}$, the oil layer will wet the surface of the SU8 pillar resulting in curvature at the oil-aqueous layer (Figure 3.5a-c). Pillars or any shape that penetrates the interface can be fabricated with varying separation distances to produce tunable degrees of curvature of the oil-water interface, which is discussed in Chapter 5.
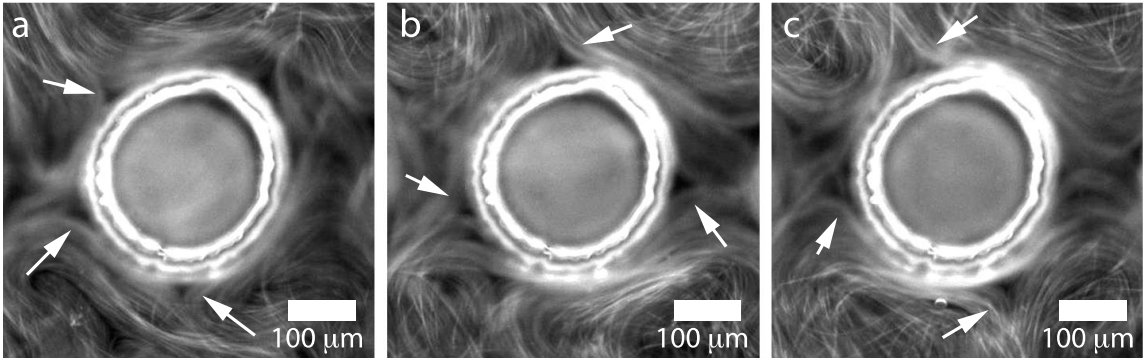
Figure 3.5. Fluorescence microscope images of active nematic surrounding an SU8 pillar. Snapshots are shown at a) t = 0 s, b) 113 s and c) 178 s. -1/2 defects (indicated by white arrows) can be seen to locate at the pillar/fluid interface.

The active nematic has an affinity for regions where the pillars are present. This could be due to curvature from the oil layer wetting creating thicker superjacent regions allowing for a more continuous active later around the SU-8 structure. This is established from the observation that the active nematic is slightly more concentrated around the pillars or the confined region with low concentrations of the microtubule network is observed everywhere else. To expand on these observations, pillars can be fabricated with different separation distances and heights, influencing the radius of curvature between two neighboring structures. This could be clarified through two explanations: 1) The curved interfaces due to wetting, serve as soft boundaries where a higher density of microtubule bundles can be seen. 2) Higher curvature means thicker oil layers which maintains a continuous active layer. The latter explanation will be discussed later in Chapter 4, but for now, thinner oil layers result in a depletion of active material. To measure the curvature, confocal microscopy can be used since the active nematic is labeled and SU-8 tends to auto-fluoresce specifically at lower wavelengths. Such measurements can determine the shape of the active layers to determine its curvature. In Figure 3.6, active matter can be seen to flow around several pillars where two interesting phenomena are highlighted. The fluorescence image shows that in the narrow gaps between pillars the active nematic appears to go out of focus then back into focus. The bundles bend down out of plane on the z-axis. This effect is very likely due to competition between anchoring conditions at the fluid interface (microtubules aligning at the interface) and the elastic cost of bending the microtubules as defects try to pass through a narrow aperture. The active flows pass through the gaps between the pillars by escaping into the 3rd dimension, i.e., the z direction, possibly deforming the interface at that point and thus minimize the bending energy cost with the added degree of freedom.

Secondly, defects between rows of pillars appear to braid around each other in a manner like the silver braid previously reported in addition to the unidirectional ceilidh dance previously reported [63] [57] [58] [78], as if the network was confined to a thin rectangular trench. This effect also supports the idea that the bundles are to some extent repelled from the narrow apertures due to bending constraints and the larger elastic energy cost, and thus the pillar array can act as a virtual channel. In a flow cell containing pillar array structures, the active network tends to concentrate near the pillars, rather than spread throughout the flow cell uniformly where once surrounding the pillars, the network tends to flow preferentially around the regions close to the pillar walls.
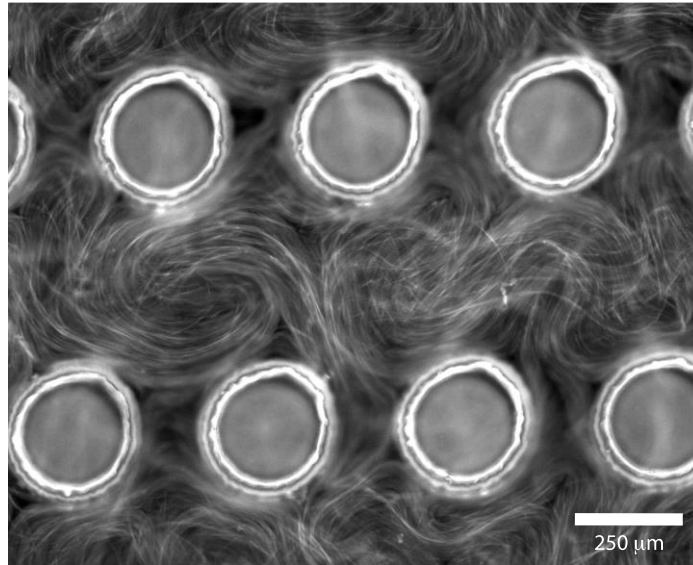
Figure 3.6. Bundled microtubule active nematic flows interacting with an SU8 pillar array.

We made observations of the active nematic system under the condition $h_{pillar} < h_{oil}$ i.e., the fabricated structures are submerged in the oil layer and the active matter moves in a continuous plane away from the submerged structures. This setup appears to have some interesting consequences and show that defect speeds are affected by the presence of the submerged structures. This interesting observation was investigated in addition to the relationship between defect dynamics. However, it would be interesting to observe how the separation distance between the active nematic and the top of a pillar, d_{gap} effect defect trajectories. Using the convenient SU-8 devices, it will be possible to perform these experiments.

3.3.2 Fabricated Trenches

In another interesting direction, I discussed that straight walled trenches can serve as a confinement strategy by Jerome et al [28] in passive nematics, and then, for active nematics [63] [57]. In this more linear configuration, the bundled active nematic is confined to rectangular microfluidic channels with a width of 320μm (Figure 3.7). The twist to this preliminary study is that the pattern is submersed in the superjacent fluid driving interesting

defect behavior. Defects were observed to braid around each other in a distinct pattern and concentrate in specific regions within the channel. More specifically, -1/2 defects tended to localize on the sidewalls of the channel and +1/2 defects tend to localize midway through the trench. Furthermore, +1/2 defects were observed to annihilate when approaching the sidewall, caused by the large concentration of -1/2 defects in this region of the device. In Chapter 4, we describe organized defect distributions.

These findings are fascinating as several implications can be made about the adaptability to the active gel and the viscous properties of the superjacent fluid. 1) The presence of the submersed structure influences the active network via changes in oil depth through an induced effective friction and 2) activity gradients occur consequent to these changes, resulting in positionally controlled defect morphology and kinematics. In Chapter 4, we will go more in depth on these findings.
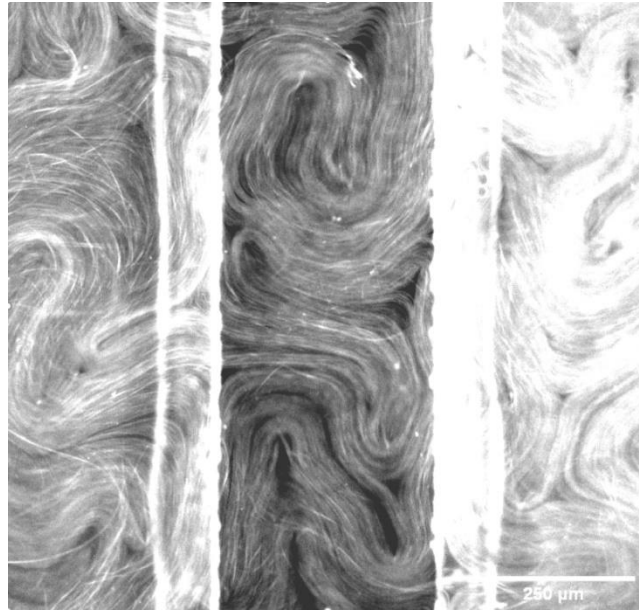
Figure 3.7. Fluorescent image of submerged 320μm wide micropatterned trench soft confining active material.

3.4   Conclusion

In this Chapter, I describe several simple methods to create active nematic compatible structures using a biocompatible glassy photo-patternable polymer SU-8 using a lithography process. These structures can be used to confine active material in a transparent flow cell which is ideal for both bright field and fluorescence microscopy. Using these techniques, various experimental configurations can be envisioned, including pillar arrays, trenches, and other submerged structures. Using these simple tools will help us explore the impact of different geometries on chaotic flows in active nematics.

In this Chapter, we introduced a fabrication process to create these geometries and the importance of handling each step. We emphasize the importance of these steps as to avoid

imperfections and errors that can occur doing a typical process. More specifically, taking these precautions help avoid several issues that can manifest in the film: cracking, warping, leaks, and poor adhesion. Each of these imperfections can negatively impact active nematic experiments and must be avoided to get consistent experimental results.

Finally, we reported on active nematic results and discussed them qualitatively. For pillars, we discuss three pillar/oil height configurations that can impact nematic flow (Figure 3.4), all of which are explored and discussed in later Chapters. In short, the unsubmerged pillar result in the curvature of the oil layer where the curvature can be tuned via the separation distance of neighboring structures. Interestingly, we also discussed submerged pillar and the resulting depletion of active material (Figure 3.4c). The last geometry we discussed was a submerged trench where we first observed the effects of submersed structures in the superjacent.

Confining geometries (submerged or unsubmerged) can significantly impact the motion of topological defects in active nematics. The behaviors observed so far in this work, are just the beginning of our ability to control and manipulate active materials. In the next Chapter, we report our quantitative findings of the presented geometries in addition to other interesting micro-milled designs. Instead of geometries that either impinge or penetrate the interface, the material is completely submerged, creating a virtual or soft boundary. These boundaries generate defects dynamics reminiscent of non-submerged structures.

Chapter 4: Demonstration of virtual boundaries using submersed microstructures

4.1 Introduction

There are many ways to apply different boundaries to an active nematic system. So far, different silicon oils, fluorinated oils, different immiscible fluids, and pattern structures have been described in the preceding chapters. In Chapter 3, I described using negative tone lithography techniques to influence active nematic flow and observe new forms of dynamics. Using photolithography, we propose to build on the micropattern-based method for controlling active nematic dynamics without contiguous contact with active nematic films. This can be achieved by micropatterning oil-submersed solid photo-patternable substrates below the 2D active nematic film with simple geometrical structures of variation of height. In this chapter, I describe how effective virtual boundaries within active films induced by submerged patterns that control topological defect populations, collective flow, and concentration of active nematic material without penetrating the interface of the oil layer or the active film. The implementation of the underlying submersed patterned microstructures allows for the depth of the oil layer to be tuned and adjust the dissipation within the superjacent film. This method can generate a highly tunable technique for controlling the active dynamics and defect morphology. To conduct this investigation, we chose two simple geometries, some of which were discussed in Chapter 3, rectangular trenches, rectangular steps, and circular pillars.

4.2 Experimental Methods

4.2.1 Photolithography

The trench and pillar geometries are produced using photolithography, however unlike in Section 3.2.3, geometry thicknesses had to meet a specific criterion to be submersed. SU-8 was used to create thin film plastics on substrates. Upon thorough cleaning, a quarter-sized drop of SU-8 50 is deposited on the glass substrate. The SU-8 is spin-coated at 2000rpm for 45 seconds followed by a 10-minute wait. The substrate is then soft baked at 65°C for 12 minutes then at 95°C for 45 minutes on a hotplate to evaporate solvent. The substrate is again left to cool to room temperature with another wait of 10 minutes. The film is then exposed to 365nm UV light ($500 \ mJ/cm^2$) followed by a 10-minute wait step. To crosslink the exposed epoxy groups, the substrate undergoes a PEB for 5 minutes at 65°C then for 15 minutes at 95°C on a hot plate. After the 15-minute bake, the hot plate is turned off and allowed to cool to room temperature without the removal of the coated substrate. This step is to avoid thermally shocking the film which can result in cracks and poor adhesion as discussed in Chapter 3.

The substrate is developed for 30 minutes with gentle agitations to loosen residual polymer still on the surface. Once developed, the residual SU-8 developer is rinsed with isopropanol

and nanopure water then dried with nitrogen gas. After development, the substrate is then hard baked for 2 minutes at 150°C. Internal stresses within the substrate due to the abrupt change in surface height are apparent near the edge of the trench as parallel lines. We note that some local residual SU-8 is present at the base of the pillar, but this material does not appear to affect the active nematic flow dynamics. The heights of the microstructures are measured using profilometry to ensure no warping at the edges and to ensure that the dimensions of the structures have met the criteria for the experiment.

4.2.2 Micro-milled Pattern

$$h_0 = (z_{top} - z_{bottom}) \cdot n_{oil}$$

$$h_0 \approx (8.75) \times 1.3 \approx 12 \pm 3 \ \mu m$$
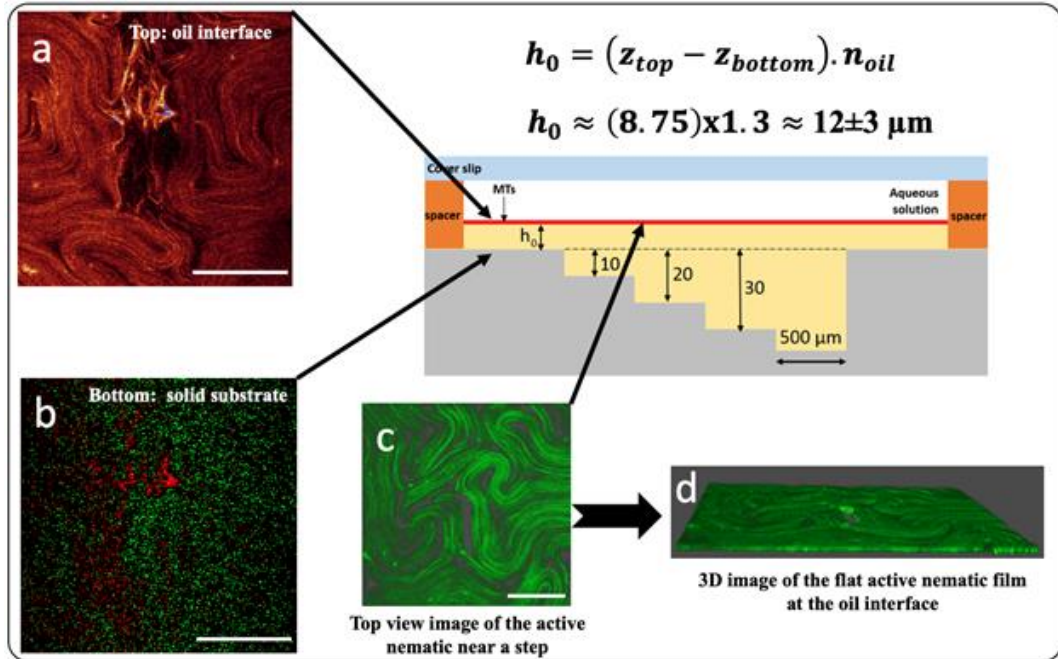
Figure 4.1. (a) Confocal fluorescent images of the active nematic film, (b) the solid substrate supporting the oil, and (c) the active nematic film closest to the step. The thickness of is obtained by measuring the difference between the heights of the active nematic film and the solid substrate, multiplied by the refractive index of the oil (1.3). (d) Near the steps, the 3D reconstruction of the active nematic confirms the film is flat without any deformation or curvature. Scale bars = 100μm. Image was produced from Dr. Mohamed Amine Gharbi in "Submersed Micropatterned Structures Control Active Nematic Flow, Topology and Concentration" [9].

I collaborated with Dr. Mohamed Amine Gharbi, who produced the micro-milled steps, undulated 1D sinusoidal patterns, and the active nematic data (Figure 4.1). I analyzed the data for defect kinematics and defect distributions (See Section 4.2.3).

4.2.3 Data Processing

To investigate how defect dynamics in the active layer are influenced by submerged structures, Alex Fluor 647 labeled microtubule bundles were imaged using fluorescence microscopy. Four hundred frame videos were collected at a rate of 1 frame per second and later processed using Fiji/ImageJ version 1.52a software. Defects were identified and counted manually every 10 frames for each video to produce defect distributions. To record the locations defects, two-dimensional Cartesian components for both x and y axes are

acquired from both +1/2 and -1/2 defects using the Click-for-position plugin in Fiji/ImageJ. For the submersed trench geometry, I used MATLAB to analyze the frequency and position for both +1/2 and -1/2 defects across the channel. Defects were then organized and binned in 10µm horizontal increments across the field of view. I applied the same counting procedure to obtain +1/2 and -1/2 defect positional frequencies across all frames for the stairway geometries as well. In the stairway geometry, we apply the counting procedure sequentially to each step and, for the pillar, the videos are processed by centering the pillar in a $400 \times 400 \mu m^2$ window. Like the analysis done with the submersed trench, we used MATLAB to generate a 2D histogram to represent the frequency of the +1/2 and -1/2 defects along the horizontal axis, positionally distributed in a 2D plane. Defects are organized and binned every 13.4µm in both horizontal and vertical increments. The nematic director field inside the channel was calculated using a Fourier transform-based method reported recently by our group [58]. To measure the director orientation directly above trenches, the imaged active nematic is oriented with the long axis parallel to the y-axis. Each pixel is converted to micrometers (0.9434µm/pixel). Each pixel from each frame containing a x-component, y-component and angle of the bundle-microtubule director is represented on a 2D grid and determined using MATLAB. Our process uses a nested loop and a conditional statement to determine if the angle is between 80-90°; if a director satisfied this condition along the y-axis for the specified x-position, the total is summed then divided by the total number of angles checked by the loop. This probability is appended to a new horizontal array for each probability in the x-position. The result is a time-averaged director orientation mapped across the trench, averaging over all y values.

4.3 Results

4.3.1 Submersed Micropatterned Trench
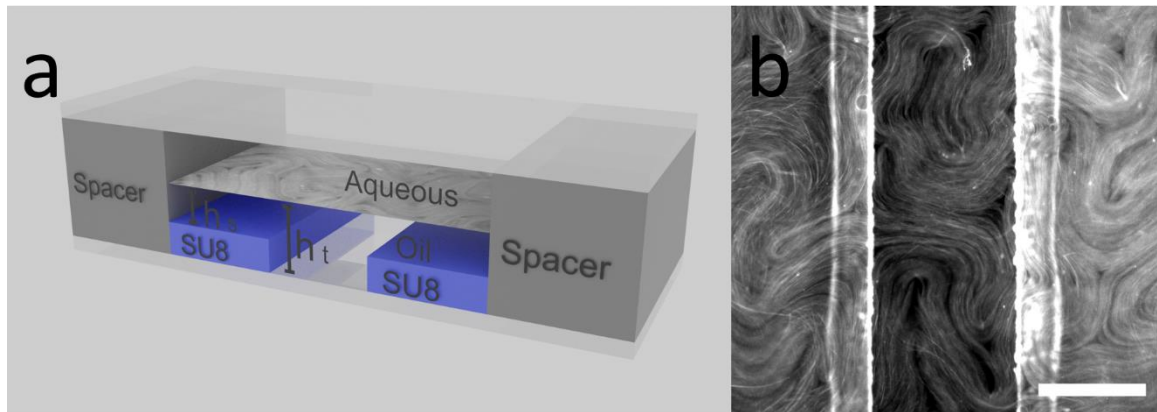
Figure 4.2. (a) 3D rendered images depicting an active film residing at the oil-water interface above different substrate depths. The active flows drag the underlying oil sublayer as viscous dissipation is depth dependent, affecting active nematic film dynamics. (b) Fluorescence microscope image of the active nematic bundled-microtubule film above a submerged trench. Scale bar = 250µm.

We first began our work aiming to investigate how fully submersed structures in a layer of oil influence defect dynamics in the superjacent active film by using the trench geometry depicted in Figure 4.2a. Like the other bundled microtubule-kinesin active networks discussed in the work, the active nematic microtubule network is confined at an oil-water

interface above a micropatterned trench with a depth of $\Delta_t = 18 \pm 1$ and a width of $w_t = 327 \pm 2 \mu m$ was fabricated using photolithography. We observed that flows in the active nematic layer exhibit the coexistence of two distinct regions: one directly above the deep trench region and the other in the shallows surrounding the trench (Figure 4.2b). These regions were separated by a well-defined virtual boundary line located directly above the trench edges. Trench edges are visible from the figure as a pair of parallel white lines due to stress-induced auto-fluorescence of SU-8 in regions of abrupt height change. Moving outside the trench boundaries, the active nematic retains the chaotic nature of active turbulence described by Tan et al [58]. Within the boundaries, the trench width establishes a local soft confining length scale within the superjacent active nematic film indicated in Chapter 3. The virtual walls softly trap defects in the deep trench region and produce active flow behaviors comparable to those observed in confining channels [7] [63] [57] [79] [80]. This observation illustrates the effectiveness of virtual boundaries on how they can be used to define areas between organized flows and areas of unorganized flows without penetrating the active film.

The topological defect distributions between +1/2 and -1/2 across the trench demonstrate that -1/2 defects tend to be at the virtual boundary (Figure 4.3a). From experimental observations, -1/2 defect trajectories near the boundary reveal that they tend to linger over long intervals with very little deviation from their initial position which contributes to peaks indicating a higher population probability. In contrast, +1/2 defects tend to be depleted from the vicinity of the trench boundary and are confined along the center trench region, moving along exhibiting oscillatory trajectories that largely avoiding the inner boundaries as per our analysis in Chapter. In the exterior region (shallow) away from the virtual trench, the defect density profile approaches the expected regime of homogeneous distribution of positive and negative defects. The effective virtual boundaries arise from the sudden steps in fluid depth $h(r)$ between the film and the underlying substrate within the oil sublayer at each point r. The fluid depth h increases from h_s in the surrounding shallows to a trench depth $h_t = h_s + \Delta_t$. As the activity drives the flow within the active film, the underlying oil layer viscously dissipates the momentum because of a no-slip substrate condition, which is the local effective friction acting on the area within the superjacent active film [81]. Following from the lubrication limit, the effective friction coefficient scales as $\gamma \sim \frac{\eta'}{h(r)}$, where η is defined as the effective viscosity of the film. In short, the abrupt height change across the trench boundaries results in sharp, virtual boundaries.
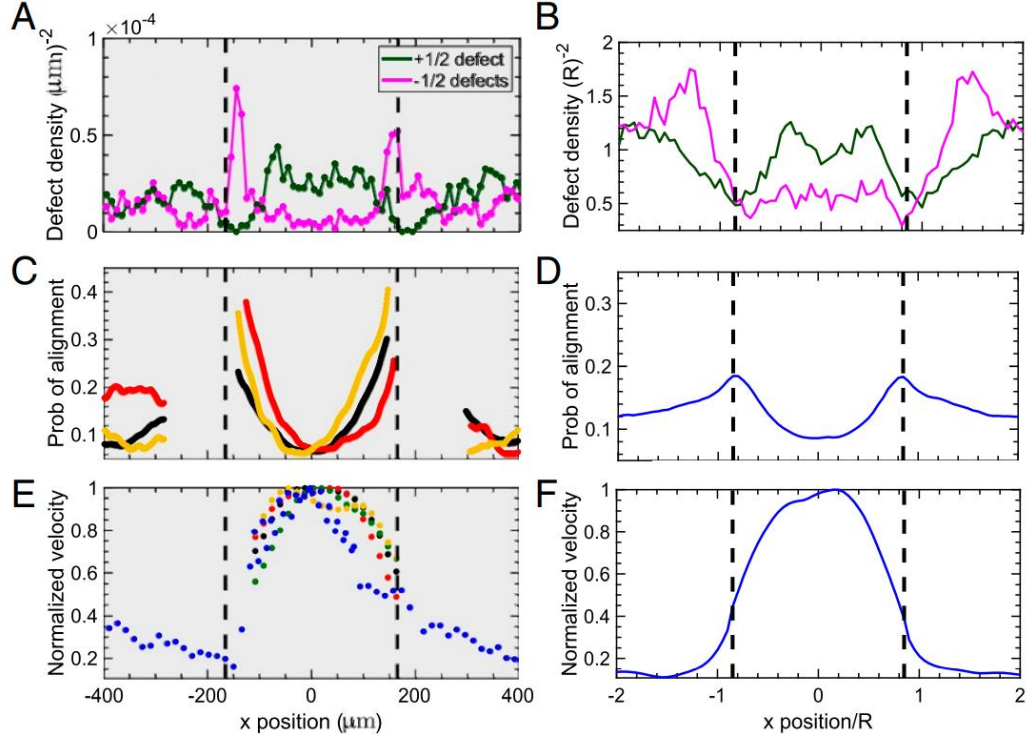
Figure 4.3. (a-b) Distribution of +1/2 (dark green) and -1/2 (magenta) defects as a function position x. (c-d) Probability of nematic director oriented less than 10° from the direction parallel to the trench wall as a function of x. (e-f) Normalized root mean square fluid velocity profile across the trench.

With the help of our collaborators Dr. Tyler Shendruk and Dr. Krisitan Thijssen, nemato-hydrodynamic simulations were developed to replicate the observed experimental data where the submersed micropatterns are incorporated by applying an effective friction field. Numerical results demonstrated that a step in effective friction can reproduce experimentally observed nematic flows and computationally introduce virtual boundaries in the active layer repelling +1/2 defects (Figure 4.3a-b).

Integration of the defect density across the channel in Figure 4.3b gives a net zero defect charge; however, it was challenging to accurately identify -1/2 defects than +1/2 from experiments. This caused some labeling bias and a slight net positive charge in Figure 4.3a as defects is more difficult to define because of the lack of a continuous layer. This agreement between experimental and numerical defect distributions demonstrates how effective friction is the mechanism by which micropatterned structures create a virtual planar boundary and introduce a confinement length scales to the active nematic without the need for the structure to penetrate the film. The -1/2 defect density peak at the virtual boundary (Figure 4.3a) being a consistent motif which has been cited by Opathalage and Hardouin et al [7] [63] showing that walls can act as a point of defect nucleation: in other words, +1/2 defects nucleate from the virtual boundary and is propelled into the interior of the trench, while the -1/2 defects remain behind. From the experimental data, -1/2 defect density peaks are sharp when in the vicinity of the virtual boundaries (Figure 4.3a), however, it is broadened and peaked outside the trench region in simulations (Figure 4.3b).

Time-averaged director orientation across the trench reveals that the virtual boundaries introduce a bias in the alignment of the director as the probability of aligning to the interface relative to the bulk, reminiscent of that seen for impermeable boundaries. This is due to orthogonal bundling midway over the boundary being subject to a large axial laminar flow inside and slow disorderly flows outside producing aligning torque. The simulations exemplify this behavior, showing that the probability declines to a uniform distribution far from the trench (Figure 4.3d). The experiments exhibit much stronger planar alignment at the virtual boundaries compared to simulations, however. This resembled simulations for passive nematic tactoids where defects travel outside the interface and become virtual unless an anchoring term is included [82]. It is apparent that stronger alignment in experiments restricts -1/2 defects to the region within the inner boundary of the trench. Simulations on the other hand indicate that they are pushed to the outside of the boundaries (Figure 4.3a-b). In fact, experimentally, -1/2 are not very likely to go beyond the inner boundary towards the outer boundary. +1/2 defects are more likely to enter a region of high friction as they have more energy to overcome the frictional barrier while -1/2 are more subject to stagnation flows. Regardless both experiments and simulations confirm that +1/2 defects are largely confined between the virtual boundaries.

In addition to impacting the nematic alignment and defect position, the submersed trench also affects the velocity field depending on the depth of the oil sublayer (Figure 4.3e-f). Velocities are lower in the proximity of the trench boundary and at its maximum approaching the trench center. Since activity varies between experiments findings, the flow profiles (Figure 4.3e) were normalized and compared to the decrease predicted by the model from simulations (Figure 4.3f). Virtual boundaries do not impose no-slip conditions but rather, decrease the speed to the slower value of the surrounding active turbulence, which can be seen explicitly for an experimental position (indicated by the blue dots in (Figure 4.3e)) and from simulations (Figure 4.3f). The decreasing flow profile explains the preferential alignment of the microtubule bundles near the virtual boundaries from what can be seen in Figure 4.3c-d. Any orthogonal bundle halfway over the boundary is subject to a large, axial, laminar flow inside and slow disorderly flows outside, which compete to produce torque alignment. Comparing the faster flow profile above the trench to the slower, disorderly active turbulence in the exterior region recalls that active turbulence is a low-Reynolds number phenomenon [83]. Confinement monitors chaotic flows that would otherwise develop on scales larger than the trench width, while the low friction allows the rapid-but-steady flow profiles superjacent to the trench (Figure 4.3b-c). Despite this, higher friction produces a smaller characteristic length scale [84] but slower velocity fields within the shallow regions. Thus, the submersed micropatterned trenches can segregate rapid laminar flow above the trench and slow-but-disorderly active turbulence outside.

The submerged micropatterned trench produced virtual boundaries resulting in a confining length scale. This is due to competition between the confinement and the intrinsic active nematic length. Experiments demonstrated that a consistent vorticity structure was established between the virtual boundaries when active and confining scales coincide [7] [57] [85] and simulations emphasize the periodic nature of +1/2 defects exhibiting counter-rotating vortices. Velocity autocorrelation functions were examined in our published work to quantify different flow profiles above the trench in the deep region [9] due to how similar

their internally generated flows were to non-virtual structures. From this work correlation function exhibited repetition between correlated and anti-correlated regions due to repeating clockwise and anti-clockwise vortices of position defects in a somewhat unidirectional motion along the trench.

From simulations for a narrow trench, flows are long-ranged and oscillatory with a strong preference align along the boundaries. This oscillatory vortex-like state occurs when the confining length scale w_t, is small compared to the low-friction which is to intrinsic active nematic length scale which was reported by Shendruk et al [57]. Increasing the trench width on the other hand, predicts active turbulence in both the area superjacent to the trench and the shallow exterior regions. The difference being that active nematic length scales between the deep and shallow regions as higher friction results in smaller defect cores and length scales previously mentioned. Equally higher levels of activity decrease the active length scales and such findings have experimentally observed instances of chaotic flow states for both deep and shallow regimes. The structure of different flow states impacts the effective director alignment observed in Figure 4.3d. Again, for wider trenches, the director varies widely because of the larger area gives rise to defect creation events like reports discussed by Hardouin et al [63]. We note that the relative position of the -1/2 defect peaks at the interface does not change regardless of trench. Bound -1/2 defects is a consistent motif for any interfacial boundary.

The trench geometry demonstrates that submerged micropatterned structures can induce virtual boundaries for maintaining the coexistence of distinct flow behaviors simultaneously at different locations in a single active nematic layer. The advantage of this approach is that the boundaries act without physically penetrating the film and so active material does not first have to saturate a cavity before confinement dynamics can be examined [7]. Filling complex geometries with filament-based active material may be the prohibitive step in active microfluidics [86]. The proposed micropatterned method circumvents these hurdles, opening many more possibilities for experiments involving more complex geometries.

4.3.2   Submersed Rectangular Steps
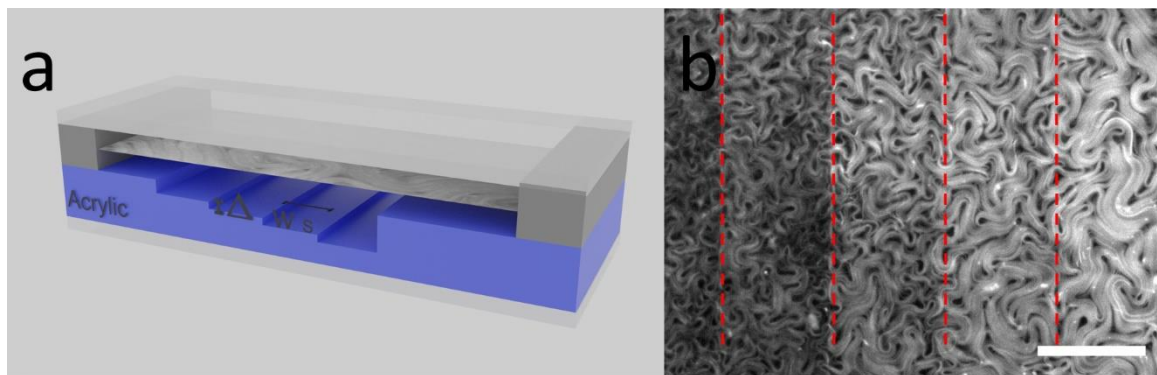
Figure 4.4. (a) 3D rendered submerged steps. (d) Fluorescence microscope image of micro-milled stairway and the superjacent active bundled-microtubule film. Scale bar = 500µm where the step locations are indicated by red dashed lines and the oil depth increases from left to right.

In our work to study the effects of friction on active nematics, we present a submerged stairway geometry (Figure 4.4a) which was designed to simultaneously observe active turbulence and progressions in the characteristic length scales. Individual steps were micro-milled having a horizontal width $w_s = 500 \pm 2\mu m$ and a step height of $\Delta_s = 10 \pm 1\mu m$. The fluid/oil depth is $h(r) = h_0 + \Delta_s n(x)$, where the step number is n and initial fluid depth of $h_0 = 12 \pm 3$, which was determined through confocal microscopy. An illustration of the cross-section of steps can be visualized in Figure 4.5. In this work, we focused our attention on steps $7 \leq n \leq 9$ for which the microtubule network formed a well-defined, continuous nematic field depicted in Figure 4.4b. As the oil depth increases with step number n, the effective dissipation within the oil-layer decreases, which was simulated via discrete steps in effective friction in the superjacent active film.
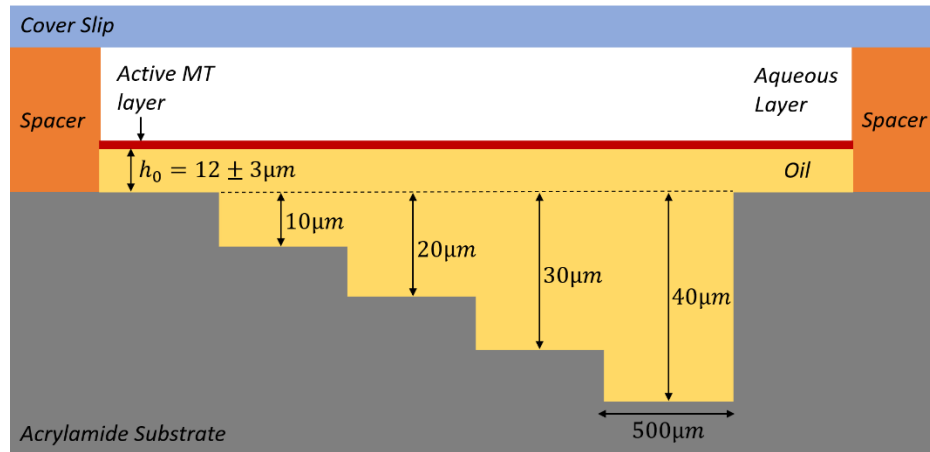
Figure 4.5. Illustration of the cross section of the submerged steps.

Above the submerged step pattern, active length scales increase with decreasing friction, characterized by the defect distribution in Figure 4.6a-b and Figure 4.5a. Within each step, the +1/2 defect distribution is relatively flat however, at each edge, the number density of -1/2 defects peaks. Furthermore, for deeper oil layers cause the density of +1/2 defects to plunge. This is consistent with defect densities at the edges of the trench (Figure 4.3a-b). Although the simulated edge peaks are less pronounced than the experimental findings, numerical results show more clearly the decrease in defect density across multiple steps. The change in defect density is relatively modest which is consistent with studies demonstrating the increase of oil viscosity by five orders of magnitude results in an increase of defect density by a factor of order unity which has been reported [8] [87] highlighting the potential tunability of our method. Because the effective friction is inversely proportional to oil depth, changes to the defect density become less pronounced

with step number and, with the large-oil-depth limit, substrate features become indiscernible within the nematic flows.
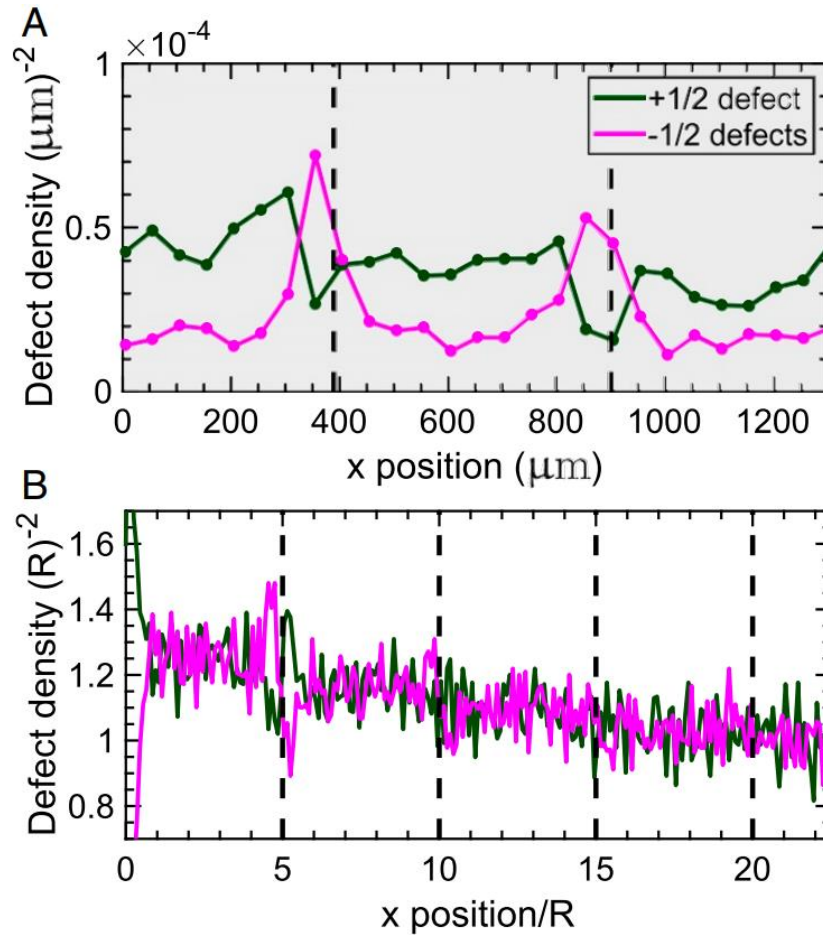
Figure 4.6. Plus (dark green) and minus (magenta) defect distribution as a function of position down the stairway x. (a) Measurements from experiments for steps of width wt = 500μm (b) Measurements from simulations for steps of width of width wt = 5R.

For both experiments and simulations done by our collaborators, we only observe a continuously well-defined nematic field for oil depths that are much greater than h_0 depicted in Figure 4.4e which can be reliably resolved that the nematic order and measure defect density with low experimental uncertainty for the seventh step ($n = 7$). For smaller step numbers ($n < 7$), the active film exhibits a disorderly nonhomogeneous texture analogous to observations in experiments utilizing highly viscous oils [8]. Active material above very thin oil layers result in a gradual loss of active material can no longer form a continuous layer. Instead, active nematic bundles appear more like strands of strings and not as a 2D sheet. This puts into context that submersed micropatterned structures can do more than impact flow and orientational state; it also demonstrates how the micropatterned substrate can control active matter concentration via thin oil layers that are still fully submerged in the underlying oil-layer.

4.3.3   Submersed Circular Pillar – High Friction
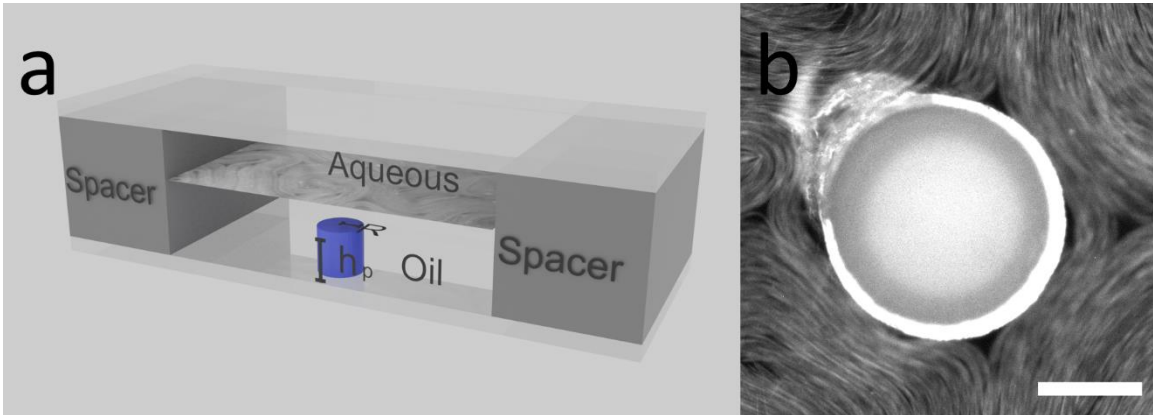
Figure 4.7. (a) 3D rendered image of submerged pillars (b) Fluorescence microscope image of the bundled-microtubule film above the SU-8 micropillar. Scale bar = 100μm.

Another simple geometry I studied was fully submerged SU-8 circular pillars (Figure 4.7a). These pillars were fabricated with a radius of $r_p = 116 \pm 2\mu m$ and a height of $h_p = 6.8 \pm 0.3\mu m$. Like the trench, sinusoid and stairway geometries, the active nematic layer is subject to a step-change in the effective oil/film friction however, differentiating it from the previous structures, the pillar's virtual boundary forms a closed loop. The most prominent effect is a pronounced depletion of active material from the enclosed pillar region Figure 4.7b which is qualitatively recapitulated in the simulations. We confirmed that the absence of active material is not a result of the pillar penetrating the active nematic film by observing microtubule bundles moving above the apex of the pillar. In Figure 4.8a-b, we observe a +1/2 defect entering the highly viscous region on the top of the pillar only to quickly dissipate leaving the top of the pillar to be completely depleted of active material. Furthermore, we did not observe curvature of the superjacent active layer in the vicinity of the micropillar, indicating that a finite oil depth lies between the subjacent pillar top and the nematic film.
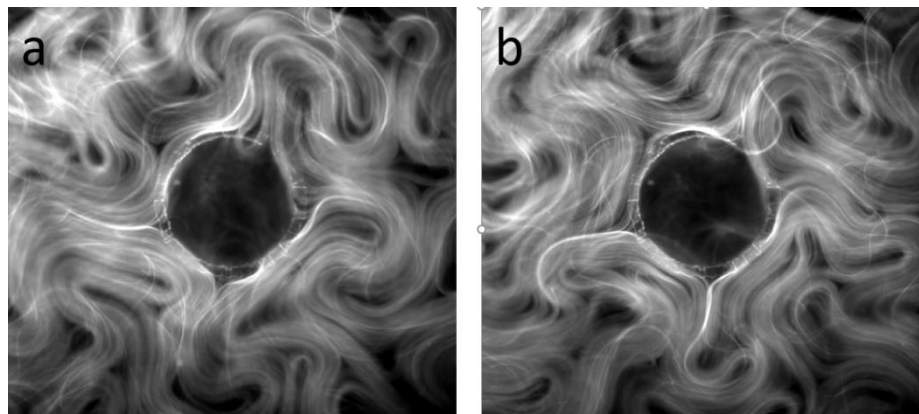
Figure 4.8. (a) Submerged SU-8 pillar with a +1/2 defect penetrating the top portion of the pillar. (b) As the +1/2 pushes toward the interior of the pillar, it quickly dissipates leaving the top of the pillar completely deplete of active material.

To understand this mechanism resulting in a pillar-bound dilute phase of active matter, a simplified model of the active nematic was considered. The effective friction is locally large above the pillar, causing the flow speeds of defects and active material to decrease in or near the enclosed area but remain non-zero beyond the pillar border. Since nematic ordering can arise in active microtubule network films due to activity-induced motion, the sharp decrease in flow causes defect speeds to also reduce when approaching the circular virtual border. The abrupt loss in velocity produces a radially outward average active force because bundles are tightly pushed at the boundary. This repulsive force moves radially outward where it sharply peaks at the interface because of the higher density of microtubule bundles, which was observed in simulations.
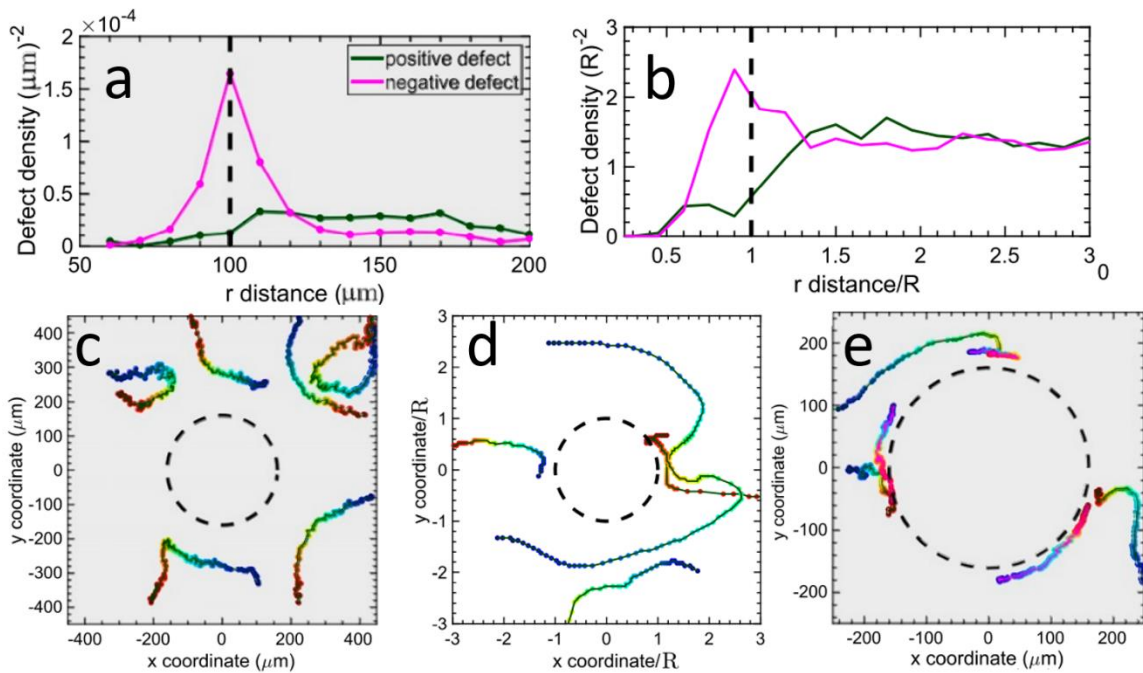
Figure 4.9. (a) Radial defect distributions from experiments (b) Radial defect distributions from simulated work. (a-c) x-y trajectories of example ±1/2 defects dynamics in the vicinity of the pillar. Time along the trajectory is displayed as circular markers colored blue at the initial time and changing to red at the final instant. (c-d) +1/2 defects deflecting from the pillar; experiments (c) and simulations (d). (j) Experimental x-y trajectories of +1/2 defects being absorbed at the pillar boundary through defect annihilation with the -1/2 residing at the perimeter.

Activity does not produce increased pressure across the perimeter but rather is able to selectively deplete the concentration of active material, enabling depletion in the incompressible film. For depletion to occur, outward advection from the encircled pillar region must be more frequent than further away from the boundary. This is the case because the activity depends on the local amount of active material present causing the radially outward force to be stronger in magnitude compared to when active material is further away. If the surrounding active turbulence is subject to advection, the local active forces increase as there is more active material concentrated at the perimeter. Hence, the active

forces can repel the material from the dissipative (high friction) region. The depletion of active matter above the pillar is a result of the high effective friction lowering the velocity causing nematic discontinuity and discrimination due to the direct dependence of activity on the local concentration.

The accumulation or depletion of active material subject to submerged micropatterned structures relies on two conditions: (i) The oil-layer must be thin (high effective friction) to suppress the active flows necessary to exhibit nematic order and (ii) there must an enclosed area that is circumscribed by a virtual boundary prohibiting longitudinal active streams because of incompressibility. Therefore, we observe lower material concentration to occur above both trench and stair geometries. Finally, we point out that material does not deplete from the pillar center in simulations on timescales investigated when a pillar radius is much larger, since the material does not diffuse to the interface where it could be selectively depleted. In addition to controlling concentration, submersed pillars interact with defects. We observe a greater frequency of -1/2 defects in the vicinity of the virtual boundary in reported simulations from our collaborators where the planar alignment of the director field explains the distribution of -1/2 defects at the pillar boundary (Figure 4.9a-b). The bend deformations at the boundary/perimeter drives boundary nucleated defects pairs with newly created self-motile +1/2 defects propelled perpendicularly from the interface and leaving behind immotile -1/2 defects.

Finally, another interesting phenomenon where submersed pillars serve as a virtual obstacle for defect trajectories. Two events can occur when a +1/2 defect approaches a pillar from the surrounding turbulence: stalling or deflection once in proximity to the pillar (Figure 4.9c-e). In Figure 4.9c-e, nine representative trajectories were considered, and we show four from a total of 360 in Figure 4.9 to illustrate the observed interactions at the periphery of the boundary. Deflected +1/2 defects first slow as they approach the pillar, then scatter and regain speed as they move away from the submerged structure (Figure 4.9c-d). On the other hand, +1/2 defects that stall as they approach the boundary temporarily hold their position before annihilating with pillar-associated -1/2 defects (Figure 4.9e). While positive defects that directly approach the pillar can temporarily enter the depleted area by driving active material ahead of them, such infrequent events are transient as the repulsive active force pushes such incursions radially outward.

4.4   Conclusion

In this Chapter, I introduced a novel non-invasive method to control and tune active nematic material using submerged geometries. These experimental finding were coupled with simulated work from our collaborators, Dr. Kristian Thijssen and Dr. Tyler Shendruk; the undulated and stair patterns were contributed from Dr. Mohamed Amine Gharbi and Dr. Seth Fraden. The geometries chosen for this work was trenches, pillars, stairways, and sinusoidal undulated patterns. We considered different conditions of oil height may influence nematic flow using pillars and trenches. In this Chapter, we aimed to make quantitative arguments for our observations with our collaborators providing simulations to our work.

For our rectangular trench, we quantified director orientation, defect distributions and v_{rms} at specific horizontal regions. We found that the abrupt change in oil depth results in the creation of a virtual boundary, causing a higher probability of microtubule bundle alignment at the boundary. The alignment probabilities in contrast to the region midway through the trench and outside the virtually confined, shallow region, found alignment less probably compared to the vicinity of the boundary. As a result of the creation of a new boundary, defects positionally organized causing -1/2 defects to be largely located at the inner virtual boundary of the soft confinement, and +1/2 defect to be largely populated midway of the channel. We argue that one of the causes of virtual boundary is the sudden change of material momentum across the deep and shallow regions. We were prompted to calculate the v_{rms} across the channel confirming that shallow oil depths result in slower velocity fields. For the stair geometries we found similar defect population patterns of +1/2 and -1/2 positioning. We did notice defect populations decreasing with increasing oil depth because of lower friction. For higher friction, defects with smaller length scales were produce allowing for larger defect populations, as slow defects cause a reduction in defect annihilation events.

Pillars were another geometry I studied for this work. The submersed pillar had an extremely thin oil layer, resulting in a complete dissipation of active material in the encircled region. If +1/2 defects managed to find their way into high friction region, it would complete dissipate and eventually disappear from the encircled area. Of course, we found similar positional defect distributions with -1/2 defects found at the outer radius of the structure with no +1/2 defects at the periphery. We also observed and quantified +1/2 defect trajectories approaching the encircled region. Two outcomes would occur, the +1/2 would either scatter and deflect elsewhere or it would be absorbed at the boundary to annihilate with a pinned -1/2 defect. Regardless of both these outcomes, the defect would slow down considerable on approach, this is likely due to a radially out forces coming from the periphery of the pillar as bundles are highly concentrated at the boundary.

Although that these submerged geometries varied in shape, we notice consistent motifs of defect dynamics. The motifs are changes in velocity fields, defect organization, and depletion of active material with oil thickness. In the next chapter, we will discuss a new method to tune oil thickness and observe defect density and the depletion effect we have observed in this chapter.

Chapter 5: Two-Tier active nematic system

5.1   Introduction

Using submerged geometries, we reported [9] that discontinuities in the depth of the underlying fluid substrate (oil layer) can also produce confinement effects, using a submersed surface structure which is not in direct contact with the active fluid. More specifically, we observed this for higher steps resulting in thinner oil depths from our step examples in the previous section. We showed that the effective viscosity of the underlying oil substrate plays a decisive role in nematic alignment and flow kinematics. If the momentum of the active nematic is not conserved between two materials (hard or soft), friction will facilitate planar anchoring between the interfaces of high and low friction. Hence, the friction generated from a submerged pattern creates positionally controlled activity gradients on the surface resulting in alignment at the boundary by varying the oil thickness [24] [88] [89] [90]. We have from this thesis that the control of active flows is not limited to hard surface boundaries of microfluidic systems, but that the material can be controlled using a soft boundary created by effective frictional discontinuity induced by the oil sublayer.

In this Chapter, I build off the previous chapter regarding the effective friction to demonstrate a new way to tame chaotic flows in active nematics. We apply a similar method of submerged geometries that impinge on the oil interface inducing curvature in the active layer that localizes the confinement effects and thus control active flows. For this investigation, we revisit the circular pillars, like the previous chapter, to create a ring of local curvature that controls active nematic dynamics in a similar fashion to cylindrical wells reported by Opathalage et al [7]. We demonstrate a variety of phenomena induced by the confinement effect consistent with other confinement methods and quantify flow velocities and defect densities as a function of underlying oil thickness. Controlling active nematic flows with curvature is advantageous over hard-well based methods as continuity of the active layer can be maintained depending on the oil thickness. This new technique provides a novel tool in the emerging suite of methods for control of active nematic flows.

5.2   Experimental Methods

5.2.1   Setup

As with our previous experiments, the active nematic is confined at the interface of the oil layer and an aqueous layer with the exception that there is curvature at specific locations within the fluidic device. The circular pillars impinge on the underlying active interface depicted in Figure 5.1, where the active material is continuous and not restricted with in the boundary of the pillar. Active material is free to move into the pillar region and outside the boundary to the open unconfined region. +1/2 defects can easily penetrate the virtual

boundary exiting and leaving the high friction region. The aim was to finely tune the superjacent fluid thickness by using pillars with varying heights.
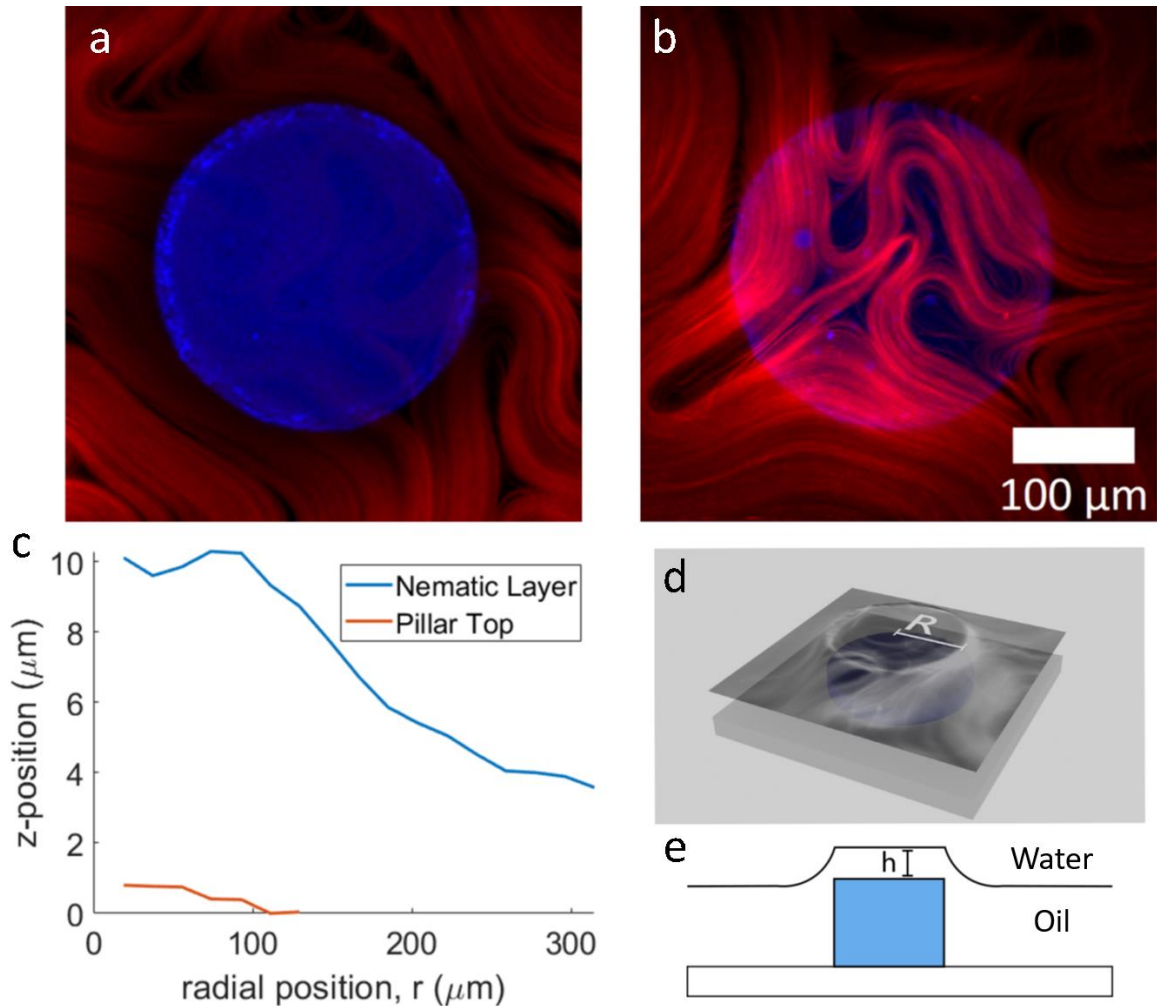
Figure 5.1. The two-tier active nematic system. (a) Two channel laser scanning confocal microscopy images showing a pillar (blue) overlayed with the active nematic layer (red) a z = 0um and (b) z = 7.45um with respect to top of the pillar. (c) graph showing curvature of the active layer plotted from the pillar center and (d) 3D illustration of the experimental setup. (e) An illustration depicting the pillar and the curvature of the active fluid.

To achieve the set-up depicted in Figure 5.1, hydrophobic pillars are partially submerged in the oil layer. Because the pillars are hydrophobically treated, the oil wets the sides of the pillar but also coats the top with a thin layer of the superjacent fluid. Cohesive forces keep the surface of the oil layer intact across the top of the pillar maintaining a relatively flat shape. Once the suspended active material is flow into the fluidic device and in contact with the oil layer, the presence of the pillar gently presses oil into the water interface enough to allow interfacial deformation to occur, producing an elevated circular region similar in shape to a butte.

The formation of curvature at the pillar boundary originates from the capillary effect that takes place at the oil-pillar interface. This is on the condition that the fabricated pillars are tall enough to impinge onto the interface of the oil layer but not tall enough to penetrate the active layer. There are several assumptions made regarding the geometry of the curved superjacent: (i) If active material is to occupy the top of the pillar region, there must be a thin oil layer within the circular boundary; (ii) the oil must also be thick enough to allow material to flow within the inner diameter of the circular boundary, D; (iii) If the oil layer is too thin, active material will be unable to form well defined defects; This implies that active material progressively depletes with thinner oil sublayers which I discussed earlier in Chapter 4 [9].

5.2.2   3D image reconstruction using confocal microscopy

To measure the curvature of the active and oil layers, we used confocal microscopy to obtain 3D reconstructions at the boundary of and across the top of the submerged pillar. In Figure 5.1a-b, we can confirm that active material within the pillar radius ($r \leq R$) is elevated from everywhere else outside the pillar radius ($r > R$). In Figure 5.1a, we observe a confocal image somewhere within the interior of the pillar set at a z-stack position of $z = 0\mu m$; at this position, active matter is seen everywhere and depleted at $r \leq R$. As we move up along the z-axis up to $z = 7.45\mu m$ (Figure 5.1b), we notice a gradual loss of fluorescent signal at $r > R$ and an increase of signal within the pillar boundary of $r \leq R$. To quantify this transition of height in the active nematic field, we were able to plot and graphically visualize the curvature of the active layer which is depicted in Figure 5.1c. It is important to note that the active material would not be confined within the pillar region without the presence of the superjacent fluid. Extremely thin or no oil within a region results in a depletion of active material and an inability to form identifiable defects as previously reported [9]. Figure 5.1d-e are illustrations representing the curvature of the active material above the oil. Mean fluorescence intensity of the active layer versus z-position is plotted from confocal z-stacks. Briefly, a series of concentric rings in the x-y plane are constructed, of width $dr = {}^r/_{14}$. The total fluorescence intensity in each concentric ring is then plotted as a function of z (Figure 5.1c); from this plot we can visualize the shape of the active layer as it covers the pillar. A ring of maximum curvature in the active layer is positioned approximately above the pillar circumference.
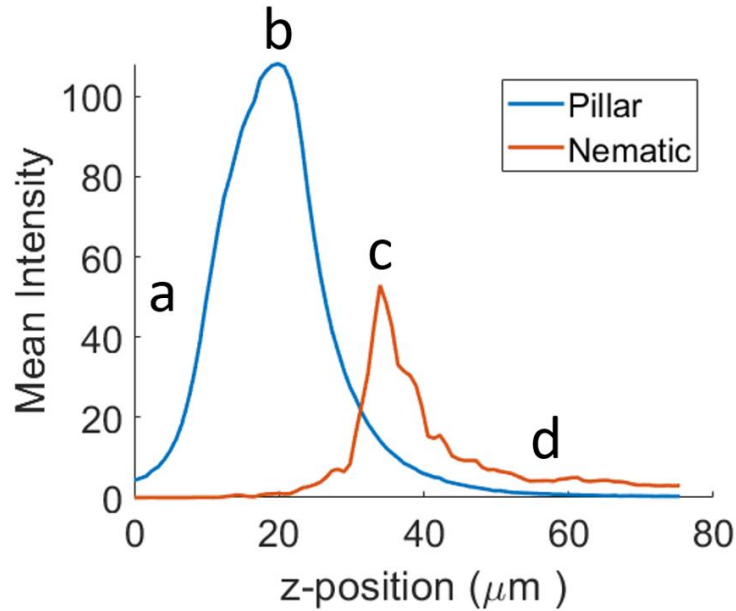
Figure 5.2. Intensity plots of the pillar and the active nematic. (a) Lowest point on intensity curve. (b) Intensity peak for Pillar. (c) Intensity peak for Nematic. (d) Signal of residual active material suspended in 3D.

To obtain the position profiles for the top of the pillar and the center of the active nematic layer, Z-stack images were taken using a LSM880 confocal microscope with a water immersion 20X objective. Z-stack images were recorded for each individual pillar (See Figure 5.2). Images within the stack were taken at 0.83μm intervals along the z-axis using two separate channels to image the pillar and the nematic layer simultaneously. Although the pillar was unlabeled, SU-8 is auto-fluorescent allowing us to obtain its 3-dimensional reconstruction using an excitation wavelength of 488nm. For the active material, we used microtubules fluorescently labeled with Alexa Fluor 647 as supplied by the Center for biomaterials at Brandeis University. The active layer was imaged using an excitation wavelength of 647nm. This labelling scheme ensured minimal cross-over effects between confocal channels.

Fiji software was used to analyze the confocal image stacks. To obtain the z-position of the top of the pillar and center of the active layer, we plotted a fluorescence intensity along the z-axis using a method of concentric rings. Beginning from the center of the pillar, concentric rings increasing in radius and of width $dr = D/14$ where D is the diameter of the pillar were defined in the x-y plane. Concentric rings are defined by the diameter, D of the pillar to fit seven data points within the pillar boundary ($d < D$). The diameters and radii of each concentric ring are denoted as $d1, d2, ..., d7$ and $r1, r2, ..., r7$ respectively, dr is also the radius of the central circle, r1. To define dr for any given pillar with a diameter D, we obtain the diameter of the central circle $d1 = D/7$. If the radius of the first concentric ring is r1=d1/2, then the radius of the first concentric ring is $r1 = D/14$. Since $dr = r1$, then dr=D/14. For each ring, we obtained a mean intensity vs. the z-position plot from the stack for both the pillar and the nematic. Using these plots, we were able to determine

locations near the bottom of the pillar (Figure 5.2a), the top of the pillar (Figure 5.2b) and the densest point of the nematic layer (Figure 39c) by overlapping both their intensity profiles (Figure 5.2). By looking at the intensity profiles, we can also observe some residual signal of active material still suspended in 3D (Figure 5.2d). The points of interest that were collected for our analysis were the peaks of the two intensity profiles. To obtain the thickness of the oil layer, we averaged the seven points from both the nematic layer and the seven points from the top of the pillar. From these results, we obtained the thickness of the oil by calculating the difference in z between the averaged values of the center of the active layer and the average values on top of the pillar. A similar process was also applied outside the pillar boundary ($D > d$) to plot active layer curvature across the pillar region (Figure 5.1d).

5.2.3 Image analysis

To investigate how defect dynamics in the active layer are influenced by submerged structures, labeled microtubule bundles were imaged using fluorescence microscopy. 400 frame videos were collected at 1 frame per second and processed using Fiji/ImageJ version 1.53c software. To acquire defect distributions, active nematic microtubule defects were identified and counted manually every 10 frames for each video. 2-D x-y cartesian components were acquired for both +1/2 and -1/2 defects using the "Click-Coordinates-Tool" plugin for Fiji/ImageJ. The videos were processed by cropping a 400 x 400 µm window and subtracting everything outside the pillar boundary; each pillar was analyzed individually. From the raw data, counted the number of +1/2 and -1/2 defects in each frame, obtained the average number of defects, then divided the averaged value by the surface area of the circular boundary. We then plotted the relationship between defect density and oil thickness for both +1/2 and -1/2 defects.

To determine root-mean-square velocity (v_{rms}) as a function of oil thickness, two regions of similar area were selected to measure from the same field of view: within the pillar boundary and outside the pillar boundary. Within the selected area, velocity fields were generated for each frame using the MATLAB app PIV lab v2.53. v_{rms} was subsequently averaged over all frames and the average normalized by the maximum value.

5.3   Results

5.3.1   Defect Morphology and transient novel defects
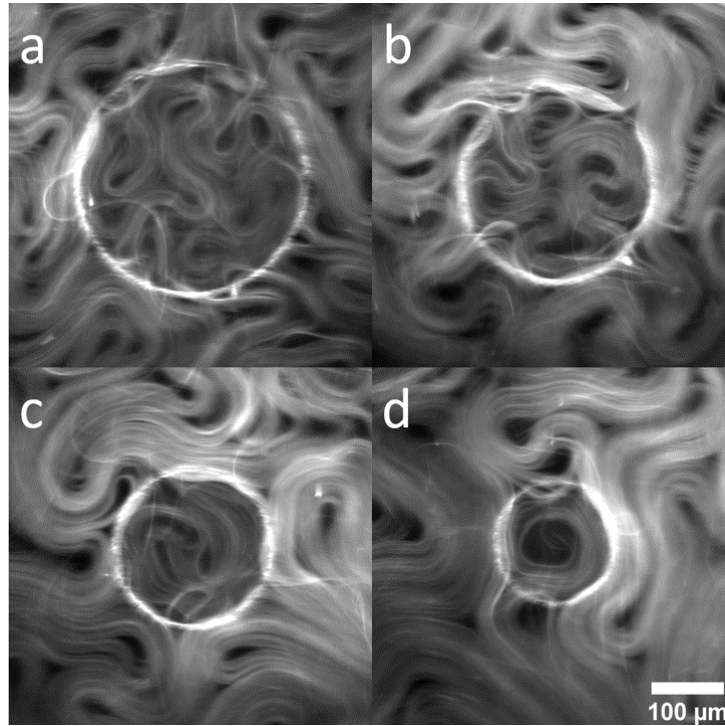
Figure 5.3. Fluorescence microscopy images of active nematic with increasing confinement above pillars of varying diameter, (a) 300μm (b) 250μm, (c) 200μm, (d) 150μm.

The active nematic devices are filled with active material as previously reported [77] [9] and during this process, fluorescence imaging shows that the active nematic layer takes time to occupy the region on top of the pillar. Once the interfacial area above the top of the pillar reaches confluence, we observe that the circular confinement effect stabilizes the nematic material.

Figure 5.3 displays four different examples of active nematic layers confined on top of pillars of different diameters of (Figure 5.3a) 300μm (Figure 5.3b) 250μm, (Figure 5.3c) 200μm and (Figure 5.3d) 150μm, respectively. We can observe topological defects in the active layer moving as though trapped within the circular pillar top region. The confined material exhibits a reduction in bundle velocity and shorter active length-scales, consistent results seen for activity above a thin oil layer reported in Thijssen et al [9]. In these examples, we observe the characteristic motions of material trapped in a circular well (Opathalage et al [7]). In Figure 5.3b a transient -1 topological defect (quatrefoil) can be observed. Figure 5.3c shows three +1/2 defects rotating about one -1/2 defect for a net defect charge of +1. In Figure 5.3d, a +1 defect with active material aligned along the inner boundary is captured.

I emphasize that the material above the pillar is not entirely confined as some defects and bundles move between the pillar top and the surrounding regions occasionally, aided by the continuous connection between these two regions. Such soft confinement is similar in nature to the results reported in Thjissen et al [9] where confinement is achieved by frictional forces, with a finite defect escape rate. Organization of the active material is enhanced with increasing confinement. For material on top of larger pillars (Figure 5.3a), circular flows do not tend to persist around the circumference of the inner radius, but as the pillar radius decreases, longer radial flows along the inner boundary can be observed. As the active material rotates about the inner boundary, defects tend to position themselves at the center of the circular region.
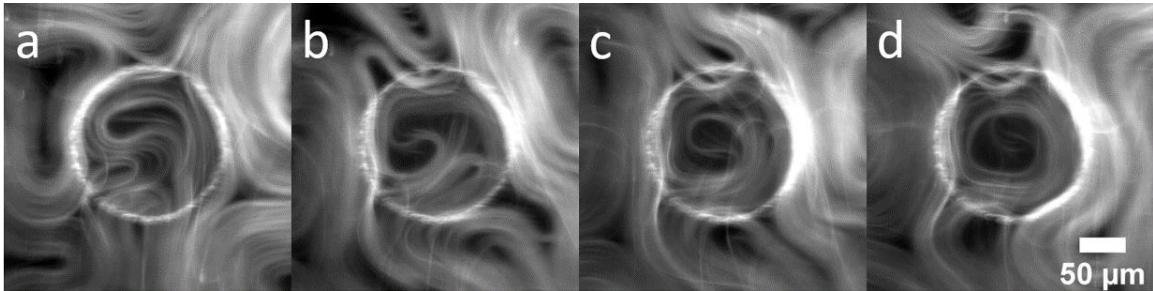
Figure 5.4. Fluorescence image sequence showing the motion of active nematic confined above a pillar. The sequence demonstrates nucleation of a defects exhibiting circular flow influenced by the circular geometry. (a) t = 230 seconds, (b) t = 275 seconds, (c) t = 300 seconds and (d) t = 320 seconds.

Focusing on the transition of +1 defects, Figure 5.4 shows a time series of images highlighting this characteristic behavior. In Figure 5.4a, a boundary nucleated defect can be observed forming and moving towards the center of the pillar. Active material collects at the boundary of the confining region and the +1/2 defects begin to spiral in Figure 5.4b. In Figure 5.4c the two +1/2 defects spiral in unison allowing them to merge while slowing being pushed towards the center, ultimately forming a +1 defect as represented in Figure 5.4d. The +1 defect performs a transient circular flow and eventually pinches off a small +1/2 defect, escaping the boundary. Such boundary nucleated defects are also observed with hard confinements (i.e., wells, [7]), even when the confining radius is small enough to produce transitory +1 defects.

5.3.2 Effect of oil layer thickness on velocity fields and defect density
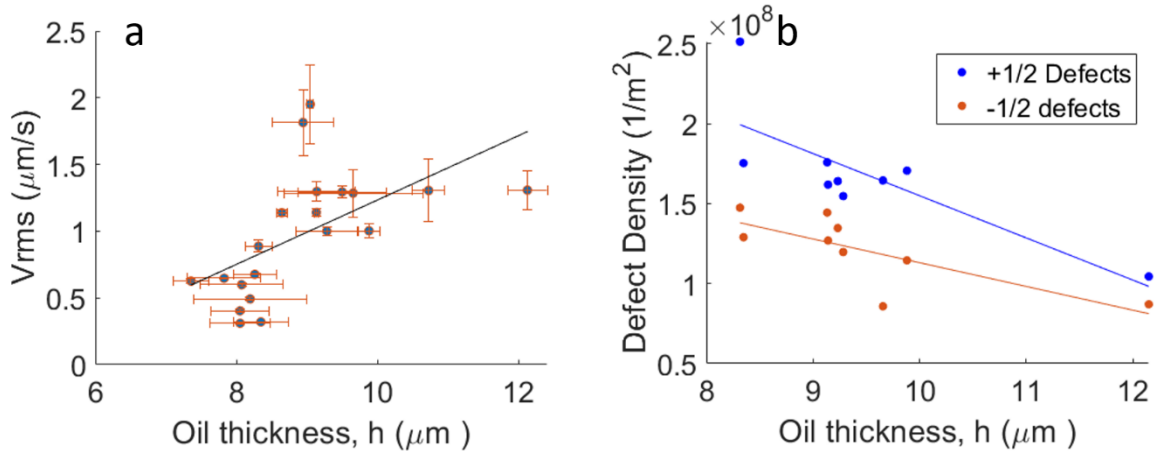
Figure 5.5. Plots showing the effect of oil substrate thickness above the pillars on nematic flow dynamics. Plots show (a) v_{rms} for the nematic flow field and (b) defect density, both as a function of oil thickness measured between the top of the pillar and the nematic layer using confocal microscopy.

Varying the oil thickness above a solid substrate (in this case the pillar tops) can result in changes in the size of the +1/2 defect core radius, the active length scale and defect kinematics [9]. Figure 5.5a shows a plot of microtubule v_{rms} for the active layer as a function of oil thickness above the pillar in the range of $\sim 7 - 12\mu m$. For each data point, the oil thickness above a different pillar was measured using confocal microscopy for a range of different pillar radii. v_{rms} was calculated using PIVLab (see methods). The linear fit added to the plot demonstrates the trend that microtubule velocity increases as the oil thickness increases, albeit with relatively large error bars. These results are consistent with previous reports and deviations from trend line may be attributed to the small areas sampled above the pillars [9]. Pillars with oil layers $< 7\mu m$ could not be measured because of the material depletion due to high friction. This will be described in more detail in the following section. Figure 5.5b shows defect density as a function of oil thickness. In a recent paper [9] defect density above a series of submerged steps revealed that defect density decreases with increasing oil thickness, and here we observe a similar trend, but for a thinner range of length-scales (8-12µm).

Despite the curvature barrier at the virtual pillar boundaries, defects can still penetrate this soft boundary wall, entering and leaving the circular region even after the system has reached steady state. As defects move onto the top of the pillar, active material and disclinations gradually slow down relative to velocity beyond the virtual boundary where they tend to circulate at the inner radius $(r \sim R)$. Defects with straighter trajectories are more likely to escape if they approach the boundary at close to 90° as defects need to overcome the change momentum because of friction. We noticed that with thicker oil layers above the pillar it is more likely that defects can escape and that they are less likely to become confined. Thus, defect kinematics in tandem with the curvature barrier at the pillar

boundary act to generate the soft confinement effect between the two regions: the pillar top, and everywhere else outside the circular boundary.

5.3.3 Thinner Oil Layers Deplete Active Nematic Material
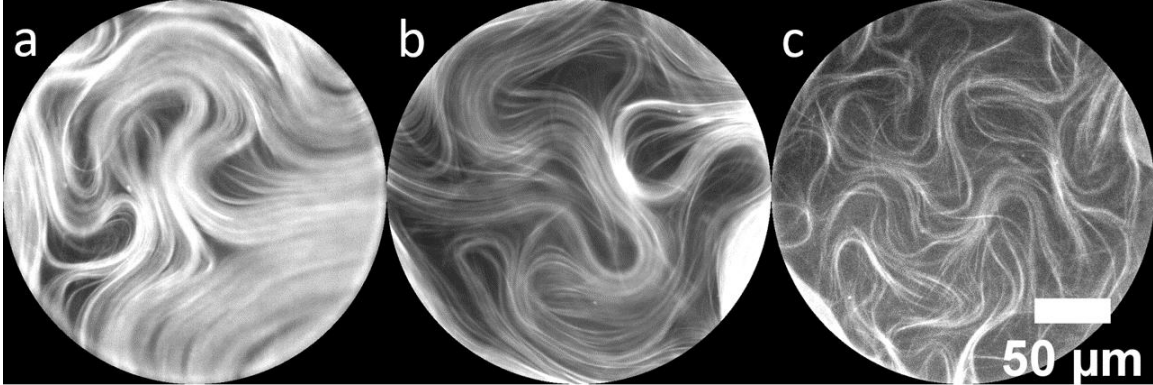
Figure 5.6. Fluorescence microscope images of active nematic on top of pillars. The images are cropped to show only the pillar tops. Consequence of depletion within a 250 µm pillar boundary with oil thickness of (a) 11.6µm, (b) 9.3µm and (c) 7.8µm.

We demonstrated in Figure 5.6, thinning the oil layer produces changes in v_{rms} and defect density. For the range of oil thicknesses depicted in Figure 5.6 (~9-12µm), voids within the active layer are minimal and primarily located at the defect cores. However, this is not the case with very thin oil layers with oil thicknesses at < 9µm. Very thin oil layers produce depletion of active material, as reported in Thjissen at al [9]. High effective friction due to a closely underlying surface disrupts the continuous nematic layer and we see similar effects within the region above the pillar when the oil thickness is very thin and large voids begin to appear. This effect is demonstrated in Figure 5.6 for three similar pillar diameters but different oil thicknesses. Figure 5.6a shows a continuous layer of active material above a pillar top with an underlying oil thickness of 11.6µm where the material away from the defect cores is nematic-like and relatively uniform. At an oil thickness of 9.3µm (Figure 5.6b) the microtubule density is reduced, but topological defects are still well defined; we also observe smaller active length scales within this region because of higher friction. Figure 5.6c shows material above a 7.8µm layer of oil where the active layer is much less dense and topological defects are poorly defined when compared to their Figure 5.6a-b counterparts. Instead of a continuous layer, the material in Figure 5.6c is composed of separated strands of bundles, with poor nematic alignment. The material continuously folds and turns but does not exhibit typical active nematic flows. Very thin oil layers result in a gradual depletion of the active material until no material is present over the pillar top, but because our method to measure the oil thickness depends on observation of the fluorescent active material above the pillar, we were unable to get an oil thickness measurement for a completely depleted pillar.

Two effects combine to deplete material from the pillar tops when the oil layer is very thin (below ~8µm). First, because the difference in effective friction between the deep and shallow regions is significant, bundles slow and are repelled when they encounter the pillar

top as previously described [9]. In addition, the curvature barrier induced by the pillar makes it difficult for defects to enter the area above the pillar. We observe that in the steady state, if +1/2 defects enter the pillar top region, they become depleted of material and the space is filled with lower density than the surrounding regions; the active nematic state is not well defined, and defects have less distinct cores.

5.4   Conclusion

In this chapter, I have demonstrated that surface-induced curvature in an active nematic layer can be a useful method to confine topological defects. To achieve the curvature confinement effect, we used circular pillars, slightly impinging on the active layer from below to produce a ring of interfacial curvature sufficient to softly confine mobile topological defects to the pillar tops. This method maintains a thin oil layer above the pillars, on which the continuous active layer is suspended. Defect motions consistent with other confinement methods were observed in previous Chapters and reported work, including slower kinematics and higher defect densities seen for thin underlying oil layers. Local curvature via our pillar method provides a new tool to direct defect flows and investigate defect dynamics on curved landscapes. This technique can be used to design defect arrays and examine defect-defect interactions in environments with obstacles. It will also be interesting to use asymmetric pillar designs to add another level of complexity to the system. This proof-of-concept method adds to the emerging suite of tools available for the control of active nematics and can actualize more possibilities for fundamental studies.

Chapter 6: Future Directions

6.1 Organized flow in pillar array lattices

The use of micro-patterned substrates to probe the bundled microtubule/kinesin system has demonstrated to be a useful method to study anchoring effects on materials in the liquid crystal phase. In previous Chapters, parallels between boundaries and director orientation of material in lyotropic liquid crystal phases have been discussed. We have demonstrated several different methods to confine active material using different geometries, either submerged or unsubmerged. Moving beyond what has been published, future aims involve control of the active fluid at a larger scale. We previously discussed active defects exposed to singular submerged pillars with varying oil thickness as to tune defect kinematics. For a future direction, revisiting unsubmerged pillars would be an interesting experiment to organize flows. We propose using unsubmerged ~60μm pillar arrays with fixed lattice spacings to observe how defects move through obstacles by tuning ATP concentrations. The aim was also to observe if defect domains can spontaneously form and perform vortex-like motion along the rows of the fabricated lattice.
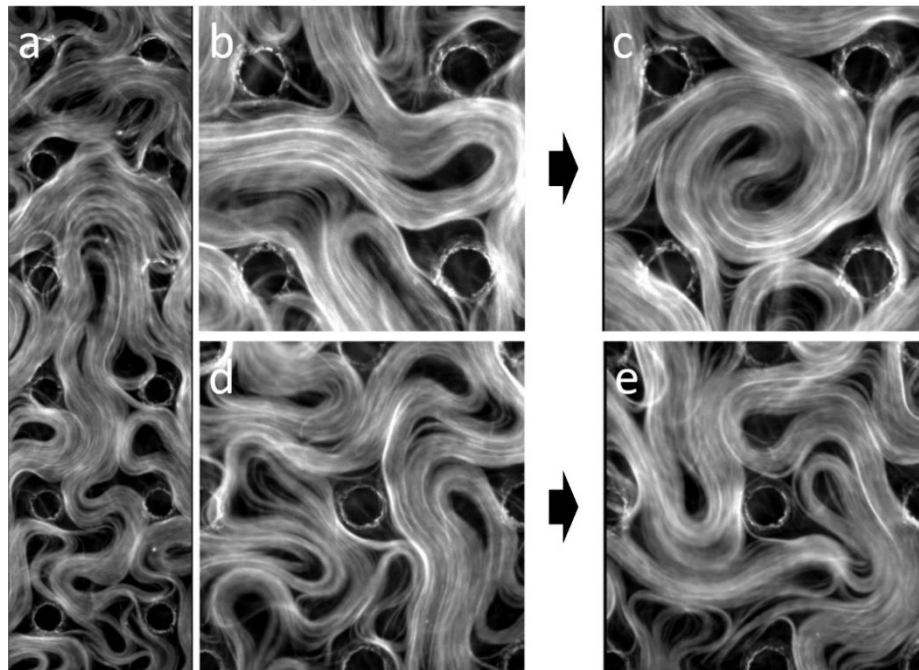

Figure 6.1. (a) +1/2 defect moving between a column of pillars in a ballistic-like fashion. (b-c) Transition of two spiraling +1/2 defects between four pillars. (d) Pinned -1/2 defect at a single pillar. (e) A pinned -1 defect at the same pillar in (d); pinned defects at pillars transitions between -1/2 and -1 interchangeably.

From initial experiments, I observe three consistent motifs of defect behaviors when in proximity to the geometries. The first motif is ballistic-like trajectories of defects as they traverse across the column of pillars. Preliminary experiments of active material exposed to pillar arrays have demonstrated more organized and straighter defect trajectories, where several defects follow relatively straighter than normal paths. These trajectories were reminiscent of the defect trains we observed for the submersed undulated geometries discussed in Chapter 4 (Figure 6.1). Active material confined to a trench exhibit unidirectional movement resembling a ceilidh dance. This dance is composed of two +1/2 defects briefly spirally around each other continuously switching partners. They continue to move towards either end of the channel where -1/2 defects accumulate at boundary. In contrast, although +1/2 defects are moving along the pillar array in a unidirectional motion, the pathways are far straighter than the braiding seen in the trench geometry.

Although the braiding observed for the channel was not observed, we did see transient +1/2 pairs spiral briefly at the center between four pillars (Figure 6.1b-c). Interestingly, these spirals can occur synchronously at adjacent points of the grid of pillars. Like the trench, negatively charged defects can also be statically pinned at a fixed position at the pillar. When pinned, -1/2 can transiently change to a -1 defect and vice versa over time (Figure 6.1d-e). Furthermore, these pinned negative defects can have longer lifetimes and will not annihilate with impinging +1/2 defects.

This new method is interesting as negative defect lifetimes and charge continuity appear longer. This could be the result of the pillar arrays pinning the negative defects at specific locations reducing the rate of annihilation events. Furthermore, the +1/2 defects could be less likely to annihilate with static negative defects because the positive defects are pushed away radially outward, which is discussed in Chapter 4 for the submerged pillar experiments. From preliminary work, the active material appears to adapt their length scales to the lattice spacing. Upon observation, defects outside the pillar array seem larger than defects within the array at lower ATP concentrations.

6.2   Defect scattering

We reported in Chapter 4 that of +1/2 defects can undergo two different scenarios when in proximity to a boundary. We reported that defects can either scatter or absorb with a pinned -1/2 defect, at the border of a confining geometry. Regardless of the outcome, when positive defects approach the boundary, they gradually slow down until it either annihilates or deflects. This reduction in velocity is due to the higher concentration of bundled microtubules at the boundary resulting in a net resistive repulsive force, pushing defects radially outward from the enclosed area. An interesting direction that can be taken is to further expand on the stagnation flows of pinned -1/2 defects and the scattering of their +1/2 counterparts.

Investigating these two effects can be used to help tune defect trajectories using different sized defects with varying lattice spacings. For example, when observing +1/2 defects approaching pillars with smaller diameters, there are less likely to be absorbed by a pinned -1/2 defect, instead they are likely to scatter. Furthermore, +1/2 defects are likely to briefly orbit the pillar, creating a net +1 defect charge with a defect ensemble of either one -1/2

defects and three +1/2 or one -1 defect and four +1/2. These observations build from the work in the section 6.2, as the organized flows through the pillar arrays are a consequence of this scattering effect. The study of how this repulsive force and pillar diameter screens whether a defect scatters or annihilates would be a good future direction for understanding how to tame chaotic active nematic flows.

6.3 Defects in the void
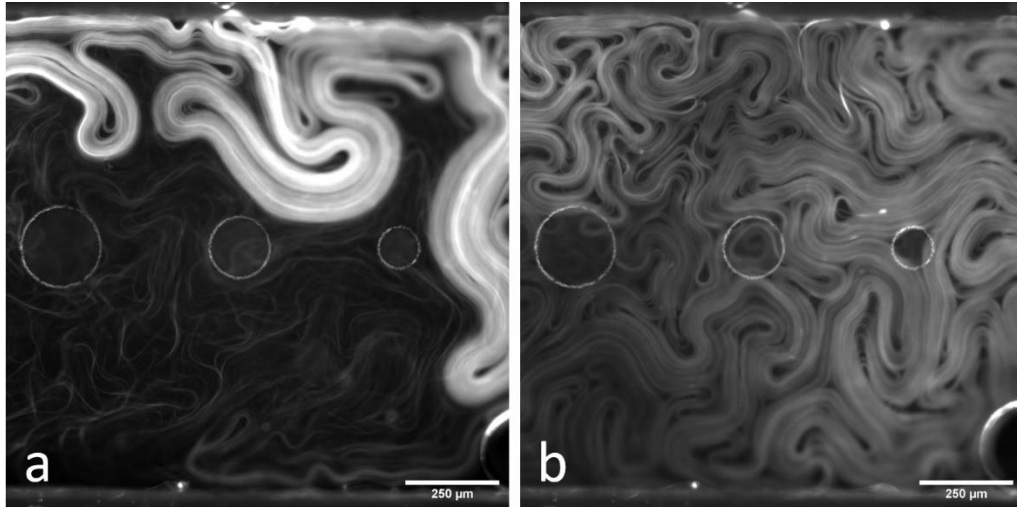
Figure 6.2. (a) Active nematic microtubule concentrated on one end of the microfluidic channel at t=1 second. (b) Active material reaching full coverage over the surface interface at t = 510 seconds.

The last direction I propose is how active material occupies depleted regions. When confining active material between the oil-water interface, different spin methods briefly accumulate the network in one portion of the interface. Due to the high density of active material at one location, defect cores and active length scales are larger. The interplay of microtubule density and activity push larger +1/2 defects into a region that is devoid of any active material. The interface increasingly becomes covered with the network, resulting in the reduction of active length scales (Figure 6.2a-b).

For this direction, the configuration of active material resembles that of a fractal, where overtime lengths are gradually reduced until they reach a critical size. Since different ATP concentrations result in different active lengths, we can observe the rate of reduction of the lengths of defects until the system reaches full coverage. Modelling this system to develop a method for fractal analysis may be a new way to characterize the networks motion and morphology of defects. Such methods have been reported by Mitchell et al [91] for a completely quasi 2D interface. It would be interesting to quantify the rate of change of active length scales over time using Mitchell's model.

6.4 Conclusion

In this dissertation, I have demonstrated novel defect kinematics and morphology using simple geometrical patterns in different configurations. The methods covered in this work

build on a novel living liquid crystal system to tame turbulent motion using microfabrication. Although the geometries presented are simple, I have presented a way to organize chaotic flows. Although we have contributed to active matter, there are still a lot more questions that can be answered in addition to building on the geometries we already worked with.

Appendix A – Experimental Preparation

A.1 Protocols for SU-8 structures

Pre-fabrication setup

Prior to fabrication, surface of substrates should be thoroughly clean to improve film/substrate adhesion. Impurities on the surface can result in features pre-maturely lifting off during measurements and experiments.

1. Sonicate glass slides for 30 minutes in Acetone
2. Sonicate glass slides for 30 minutes in Methanol
3. Sonicate glass slides for 30 minutes in Ethanol
4. Sonicate glass slides for 30 minutes in ddH2O
5. N2 gas dry and stored in a 50°C oven for later use
6. Once ready for fabrication, the substrates of surface treated using an oxygen plasma for 1 minute
7. Once in the clean room, place the substrates on a hotplate at 200°C for 2 minutes to ensure any residual moisture is completely evaporated.

SU8 patterns Fabrication protocol using SU8-50 for trenches

1. Pour a quarter sized dollop of SU8 on a clean glass slide.
2. Spin coat the SU8 using a spin coater at
   a. 500rpms, 100rpm/second then 4000rpm/second, 300rpm/sec
   b. Wait 5 minutes before removing from the spinner coater
   c. Perform a soft bake to remove remaining solvent from the film for 5 minutes at 65°C and then 30 minutes at 95°C
3. Remove from the hotplate and wait 10 minutes
4. Exposure – Measure the intensity of the lamp prior to use:
   a. Expose the SU8 at 250mJ/cm^2 at 365nm
   b. Make sure the mask makes hard contact with the film
5. Perform a post exposure bake:
   a. 2 minutes at 65°C
   b. 15 minutes at 95°C
   c. Turn off the hotplate with the glass slide still on and let it cool to 40°C
6. Development
   a. Develop the SU8 in SU8 Developer for 30 minutes with some perturbations
   b. Since is Isopropanol bath
   c. Rinse in warm water bath to avoid stress in the film
   d. Dry with N2 gas

7. (Optional) Hard bake
     a. Used to remove residual stress
     b. Place on a hot plate for 150°C for 2 minutes
     c. Remove and let it cool to room temperature then store for later use

SU8 patterns Fabrication protocol using SU8-2010 for ~18μm

1. Pour a quarter sized dollop of SU8 on a clean glass slide.
2. Spin coat the SU8 using a spin coater at
     a. 500rpms, 100rpm/second then 1250rpm/second, 300rpm/sec
     b. Wait 5 minutes before removing from the spinner coater
     c. Perform a soft bake to remove remaining solvent from the film for 10 minutes at 65°C and then 30 minutes at 95°C
3. Remove from the hotplate and wait 10 minutes
4. Exposure – Measure the intensity of the lamp prior to use:
     a. Expose the SU8 at 160mJ/cm^2 at 365nm
     b. Make sure the mask makes hard contact with the film
5. Perform a post exposure bake:
     a. 5 minutes at 65°C
     b. 10 minutes at 95°C
     c. Turn off the hotplate with the glass slide still on and let it cool to 40°C
6. Development
     a. Develop the SU8 in SU8 Developer for 30 minutes with some perturbations
     b. Since is Isopropanol bath
     c. Rinse in warm water bath to avoid stress in the film
     d. Dry with N2 gas
7. (Optional) Hard bake
     a. Used to remove residual stress
     b. Place on a hot plate for 150°C for 2 minutes
     c. Remove and let it cool to room temperature then store for later use

A.2 Active matter solution preparation and surface treatments

Acrylamide polymer brush glass slide treatment

1. Room temperature ddH2O mixed with 100µl of soap is prepared
2. Coverslips are washed in the water/soap mixture then rinsed 3 times in ddH2O water
3. Can keep submerged in ddH2O until ready for the next cleaning steps
4. Clean in 100ml in Ethanol then rinse 3 times in ddH2O
5. Clean in 100ml 0.1 M NaOH solution then rinsed 3 times in ddH2O water
6. Lay all cleaned coverslips face up in a glass dish with adequate space between them
7. Prepare silane agent:

Silane agent solution

-100ml Ethanol

-1ml Acetic acid

-500µl silane agent (Trimethylsilyl) poroplymethacrylate

8. Submerge the coverslips in the silane agent

9. Incubate for 15 minutes

10. Rinse the coverslips 3 times in ddH2O

11. Prepare Acrylamide solution

Acrylamide solution

-95ml ddH2O water

-5ml 40% Acrylamide

-degas for 30 minutes

-add 0.07 grams of ammonium persulfate (APS)

-add 35µl Temed

12. Submerge the coverslips in the Acrylamide solution and let it incubate over night at room temperature

Aquapel treatment for hydrophobic glass slides

1. Clean glass slides in acetone, methanol, ethanol and ddH2O for 30 minutes each
2. Allow to dry and stored in oven until used at 50°C
3. When it is time for an experiment, allow the glass slide to reach room temperature
4. Drop 100µl of aquapel on the cleaned glass slide

5. Drop and line up another glass slide to "sandwich" the aquapel between both slides to ensure an even coating
6. Let it sit for 1 minute
7. Take the coated glass slide and clean/sonicate in ddH2O for 2 minutes. **NOTE:** Do not sonicate if there are fabricated patterns on the surface. This can cause features to fall off. As an alternative, let the treated glass slide sit in ddH2O for 10 minutes and manually swirl it.
8. Do an additional rinse and then N2 dry

A.3 Active Matter Premix Preparation

Prepared Buffers

M2B Buffer	Solutions in M2B Buffer	Solutions in 20mM K2HPO4 (Dibasic Potassium Phosphate)
1mM EGTA	200mM PEP pH 6.9 with NaOH	20mM Trolox pH 7.48
2mM MgCl2	0.5M DTT	300 mg/ml Glucose + 70mM KCl pH 7.2
80mM PIPES pH 6.8	0.352 mg/ml Streptavidin	20 mg/ml Glucose Oxidase pH 7.5
		3.5 mg/ml + 100mM KCl pH7.4

KSA	MIX	AO1	AO2
5 µl 0.7 mg/ml K401	933 µl M2B Buffer	16 µl 0.5M DTT	20 µl 3.5 mg/ml Catalase
5.7µl 0.325 mg/ml Streptavidin	67 µl 1M MgCl2	4 µl M2B Buffer	20 µl Glucose Oxidase
0.5 µl 1:100 DTT		20 µl 300 mg/ml Catalase	
Incubate for 40 minutes			
9.7 µl M2B Buffer			

Once previous solutions are prepared, add components together in one Eppendorf tube on ice with other smaller tubes.

Active Premix
12 µl 6% wt% 20kD PEG
8 µl PEP
6 µl Trolox
4 µl KSA
2.9 µl MIX
1.7 µl PKLDH
1.33 µl AO1
1.33 µl AO2

Once the active premix is made, aliquot 3.73 µl of the solution in individual small tubes while still on ice. For each aliquot, close the tube to prevent evaporation of the solution. Once finished with the aliquots, flash freeze using liquid nitrogen and store immediately in a -80°C.

Active Nematic Bundled Microtubule/Kinesin Experiments using submerged structures

Active nematic bundled microtubule/kinesin material is prepared fresh prior to each experiment. ATP concentrations in these experiments are at saturation kinetics of 1mM. Active nematic bundled microtubule solution is comprised of:

Active nematic network
3.73µl active premix
1.00µl 6mg/ml microtubules
0.60µl 10mM MgATP
0.67µl M2B

1. Prior to conducting experiment, glass slides with fabricated geometries are treated with aquapel so the pattern and glass substrate is hydrophobic.
2. Double sided adhesive spacers are placed around the structures to form a rectangular channel.
3. An acrylamide treated coverslip is retrieved from solution and rinsed in ddH2O then dried with nitrogen gas, keeping track of the hydrophilic slide
4. The hydrophilic side of the coverslip is placed facedown and pressed gently onto the double-sided adhesive making sure the coverslip is firmly bound creating channel with only two openings on either side.
5. 6µl of HFE 7500 with 1.8% RAN surfactant slowly pipetted into the channel ensuring the flowcell is filled with oil being mindful to avoid bubbles.
6. 6µl of active material is pipetted into the flowcell. Filter paper is used to help wick the active material towards the other end of the cell making sure to avoid bubbles.
7. Both ends of the flowcell are sealed using Rapid FIX epoxy glue and cured using UV light.
8. The flowcell containing the active material is spun down using a sorval swing bucket centrifuge at 1000rpms for 15 minutes.

A.4 Active Nematic Bundled Microtubule/Kinesin Experiments using pillar arrays

Active nematic bundled microtubule/kinesin material is prepared fresh prior to each experiment. For this work, different ATP concentrations were used for these experiments. Active nematic bundled microtubule solution is comprised of:

Active nematic (1mM MgATP)	Active Nematic (100µM MgATP)	Active Nematic (50µM MgATP)	Active Nematic (10µM MgATP)
3.73µl active premix	3.73µl active premix	3.73µl active premix	3.73µl active premix
1.00µl 6mg/ml microtubules	1.00µl 6mg/ml microtubules	1.00µl 6mg/ml microtubules	1.00µl 6mg/ml microtubules
0.60µl 10mM MgATP	0.60µl 10mM MgATP	0.60µl 500mM MgATP	0.48µl 125µM MgATP
0.67µl M2B	0.67µl M2B	0.67µl M2B	0.79µl M2B

1. Prior to conducting experiment, glass slides with fabricated geometries are treated with aquapel so the pattern and glass substrate is hydrophobic.
2. Excess pillars in array are scraped off using a razor blade to fit to a specific flowcell width.
3. Double sided adhesive spacers are placed around the structures to form a rectangular channel.
4. An acrylamide treated coverslip is retrieved from solution and rinsed in ddH2O then dried with nitrogen gas, keeping track of the hydrophilic slide
5. The hydrophilic side of the coverslip is placed facedown and pressed gently onto the double-sided adhesive making sure the coverslip is firmly bound creating channel with only two openings on either side.
6. 6µl of HFE 7500 with 1.8% RAN surfactant slowly pipetted into the channel ensuring the flowcell is filled with oil being mindful to avoid bubbles.
7. 6µl of active material is pipetted into the flowcell. Filter paper is used to help wick the active material towards the other end of the cell making sure to avoid bubbles.
8. Both ends of the flowcell are sealed using Rapid FIX epoxy glue and cured using UV light.
9. The flowcell containing the active material is spun down using a sorval swing bucket centrifuge at 1000rpms for 15 minutes.

Appendix B   Selected code for data analysis

B.1   Initialize computation for angle bias in groups

Initialize_order_param_calc.m

```matlab
nframe = 400;
order_param_data = [];
for framenumber = 1:nframe
    load(['directors',num2str(framenumber)]);
    xpos = pixTomicron * (1:size(directors,2));
    %ypos = pixTomicron * (1:1016); %Trench 1: 1024, 2: 1026, 3: 1000, 4: 1016
    ypos = pixTomicron * (1:size(directors,1));
    Xc = directors(:,:,1);
    Yc = directors(:,:,2);
    Zc = Yc./Xc;
    theta = atand(Zc);
    order_param_testing_V1;
    order_param_data = [order_param_data;order_param_set];
    fprintf('End of frame %d.\n',framenumber);
end

ave_op_trench = mean(order_param_data);

plot(1:size(div_theta, 2),ave_op_trench);
xlim([0,101]);
ylim([0,1]);
title('Order Parameter across channel');
xlabel('Binned Data in 30µm intervals');
ylabel('Order Parameter, S');
```

B.2   Calculate the probability of director at a horizontal position

Comp_angle_bias_V2

75

```matlab
%nframes = 400;
%mkdir('test');
%savefile = 'C:\Users\Cyrus\Desktop\director_field\02-08-2018\test\';
%load('02-08-2018\AN2_DF_1\directors1');
%load('directors100');
pixTomicron = 0.9434; %micron/px
% count = 0;
%xpos = pixTomicron * (1:344); %Trench 1: 342, 2: 340, 3: 340, 4: 344
xpos = pixTomicron * (1:size(directors,2));
%ypos = pixTomicron * (1:1016); %Trench 1: 1024, 2: 1026, 3: 1000, 4: 1016
ypos = pixTomicron * (1:size(directors,1));
Xc = directors(:,:,1);
Yc = directors(:,:,2);
Zc = Yc./Xc;
theta = atand(Zc);

posTheta = abs(theta);
posTheta(isnan(posTheta))=0;
mag = sqrt((Xc).^2 + (Yc).^2);
[Xc, Yc] = meshgrid(xpos, ypos);
%condTheta = zeros(1,344); %Trench 1: 342, 2: 340, 3: 340, 4: 344
condTheta = zeros(1,size(directors,2));
for i=1:size(directors,2) %Trench 1: 342, 2: 340, 3: 340, 4: 344 1:size(directors,2)
%    disp(i);
    for j=posTheta(1:end,i)
%        disp(j);
        count=0;
        for ii=1:size(directors,1) %Trench 1: 1024, 2: 1026, 3: 1000, 4: 1016
1:size(directors,1)
            if j(ii) > 80 && j(ii) < 90
                count = count + 1;
            end
        end
        condTheta(i) = count;
    end
end

prob = condTheta./size(directors,1); %Trench 1: 1024, 2: 1026, 3: 1000, 4: 1016  e =
size(directors,1);
```

B.3 Frequency plots for submerged steps

frequency_plot.m

```matlab
Neg = readtable('AN_Steps_37_5bin_Neg_Freq.csv');
Pos = readtable('AN_Steps_37_5bin_Pos_Freq.csv');
%Neg = readtable('neg_def_SDS.csv');
%Pos = readtable('pos_def_SDS.csv');
neg_x_pos = Neg.Var1;
neg_y_freq = Neg.Var2;
pos_x_pos = Pos.Var1;
pos_y_freq = Pos.Var2;
neg_x_max = max(neg_x_pos);
neg_x_min = min(neg_x_pos);
pos_x_max = max(pos_x_pos);
pos_x_min = min(pos_x_pos);
total_defects = neg_y_freq + pos_y_freq;
defect_array = [pos_y_freq, neg_y_freq];

figure(1)
plot(neg_x_pos, neg_y_freq, 'r');
%xlabel('x-position ({\mu}m)');
%ylabel('Frequency');
hold on
%figure(2)
plot(pos_x_pos, pos_y_freq, 'b');
%xlim = ([pos_x_min, pos_x_max]);
xlim = ([neg_x_min, neg_x_max]);
xlabel('x-position ({\mu}m)');
ylabel('Frequency');
legend('-1/2 Defects', '+1/2 Defects');

figure(3)
bar(neg_x_pos, defect_array, 'stack');
% xlim([pos_x_min, pos_x_max]);
% xlim([10, 1000]);
xlabel('x-position ({\mu}m)');
ylabel('Frequency');
legend('+1/2 Defects', '-1/2 Defects');

figure(4)
bar(neg_x_pos, total_defects);
xlabel('x-position ({\mu}m)');
ylabel('Frequency');
```

B.4   Finding the center of the pillar

circFit.m

```
circ_points = [65.033   27.124;231.373  278.758;44.771   258.497]; %10132021_300_11

%circ_points = [212.987 380.519;360.390 188.961;163.636 157.143]; %250 02-05-2021
12V2


x1 = circ_points(1, 1);
y1 = circ_points(1, 2);
x2 = circ_points(2, 1);
y2 = circ_points(2, 2);
x3 = circ_points(3, 1);
y3 = circ_points(3, 2);

%Calculate the slopes for the points
m_AB = ((y1 - y2)/(x1 - x2));
m_BC = ((y3 - y2)/(x3 - x2));

%Determines the x-coordinate of the center of the circle
x_ctr = ((m_AB*m_BC*(y3 - y1) + m_AB*(x2 + x3) - m_BC*(x1 + x2))/(2*(m_AB -
m_BC)));

%Determines the y-coordinate of the center of the circle
y_ctr = (-(1/m_AB)*(x_ctr - ((x1 + x2)/2)) + (y1 + y2)/2);

%Find the radius of the circle
radius = sqrt((x1 - x_ctr)^2 + (y1 - y_ctr)^2);

%Print center of circle i.e. pillar
circ_center = [x_ctr, y_ctr];
radius_string = sprintf('The radius of the pillar is: %d', radius);
ctr_string = sprintf('The center of the pillar is:\n %d, %d', circ_center);
disp(radius_string);
disp(ctr_string);
disp("Nice one gamer!");
```

B.5   Histogram plot for a single pillar script

Sing_Pill_Hist.m

```
Lvid3 = readtable('L_Single_Pillar_Vid3.csv', 'HeaderLines', 1);
Lvid6 = readtable('L_Single_Pillar_Vid6.csv', 'HeaderLines', 1);
```

```matlab
Lvid8 = readtable('L_Single_Pillar_Vid8.csv', 'HeaderLines', 1);
Rvid3 = readtable('R_Single_Pillar_Vid3.csv', 'HeaderLines', 1);
Rvid6 = readtable('R_Single_Pillar_Vid6.csv', 'HeaderLines', 1);
Rvid8 = readtable('R_Single_Pillar_Vid8.csv', 'HeaderLines', 1);

x_hist = 77:8:269;
r_position = 60:10:250;

center_of_pillar = [200.9597 199.221]; %Left Pillar Vid3
%Master defect line up... These columns do not discimate between +1/2 and
%-1/2 defects. This only organizes the x and y positions into two columns,
%respectively
x_position = [Lvid3.X; Lvid3.X_1; Rvid3.X; Rvid3.X_1; Lvid6.X; Lvid6.X_1; Rvid6.X;
Rvid6.X_1; Lvid8.X; Lvid8.X_1; Rvid8.X; Rvid8.X_1];
y_position = [Lvid3.Y; Lvid3.Y_1; Rvid3.Y; Rvid3.Y_1; Lvid6.Y; Lvid6.Y_1; Rvid6.Y;
Rvid6.Y_1; Lvid8.Y; Lvid8.Y_1; Rvid8.Y; Rvid8.Y_1];

%Negative defect histogram2
neg_x_position = [Lvid3.X; Rvid3.X; Lvid6.X; Rvid6.X; Lvid8.X; Rvid8.X];
neg_y_position = [Lvid3.Y; Rvid3.Y; Lvid6.Y; Rvid6.Y; Lvid8.Y; Rvid8.Y];

%Positive defect histogram2
pos_x_position = [Lvid3.X_1; Rvid3.X_1; Lvid6.X_1; Rvid6.X_1; Lvid8.X_1;
Rvid8.X_1];
pos_y_position = [Lvid3.Y_1; Rvid3.Y_1; Lvid6.Y_1; Rvid6.Y_1; Lvid8.Y_1;
Rvid8.Y_1];

%B = x_position(~isnan(x_position));
x = rmmissing(x_position);
y = rmmissing(y_position);

pos_x = rmmissing(pos_x_position);
pos_y = rmmissing(pos_y_position);

neg_x = rmmissing(neg_x_position);
neg_y = rmmissing(neg_y_position);

r_all = sqrt((x_position - center_of_pillar(1,1)).^2 + (y_position -
center_of_pillar(1,2)).^2);
r_pos = sqrt((pos_x - center_of_pillar(1,1)).^2 + (pos_y - center_of_pillar(1,2)).^2);
r_neg = sqrt((neg_x - center_of_pillar(1,1)).^2 + (neg_y - center_of_pillar(1,2)).^2);

%plots the master histogram2 indisciminate of defect charge
figure(1)
histogram2(x, y, [30 30],'FaceColor','flat');
```

```matlab
colorbar
xlabel('X-position ({\mu}m)');
ylabel('Y-position ({\mu}m)');
zlabel('Frequency');

figure(2)
histogram2(neg_x, neg_y, [30 30],'FaceColor','flat');
colorbar
xlabel('X-position ({\mu}m)');
ylabel('Y-position ({\mu}m)');
zlabel('Frequency');

figure(3)
histogram2(pos_x, pos_y, [30 30],'FaceColor','flat');
colorbar
xlabel('X-position ({\mu}m)');
ylabel('Y-position ({\mu}m)');
zlabel('Frequency');

pos_hist = histogram(r_pos);
pos_edges = pos_hist.BinEdges;
pos_counts = pos_hist.BinCounts;
pos_values = pos_hist.Values;

neg_hist = histogram(r_neg);
neg_edges = neg_hist.BinEdges;
neg_counts = neg_hist.BinCounts;
neg_values = neg_hist.Values;
defect_array = [pos_counts; neg_counts];

figure(4)
bar(r_position, defect_array, 'stack');
xlim([0 220])
xlabel('radial position ({\mu}m)');
ylabel('Frequency');
legend('+1/2 Defects', '-1/2 Defects');
```

B.6   Tracking 2D defect trajectories using manual tracking data script

Track_trajectory_plots.m

```matlab
%Trajectory plotting of defects

%Enter the number of tracks
ntrack =17;
```

```matlab
%Center of the pillar from circFit.m script; please make sure you have this
%data before continuing the script!!!
center_of_pillar = [283.488 280.987]; %Vid6 Left Pillar
pix_con = 1;

%Upload manual tracking data
trackingDataTable = readtable('Results from MMStack_Default in µm per sec.csv');


%trackingDataTable = readtable('test_track_Rvid3_5.csv');

%Converts table into matrix so it is easier to parse through tracks
T_matrix = trackingDataTable{:,:};

%Practicing how to organize the converted matrix
%track1 = T_matrix(T_matrix(:,1)==1,:);
%x(x(:,1)==1,:);
%track2 = T_matrix(T_matrix(:,1)==2,:);
%trackingData(trackingData(:,2)==0,:);

%This loop converts the matrices into a one row cell array where the number
%of columns equates to the number of tracks
for i = 1:ntrack
    T{i} = T_matrix(T_matrix(:,1)==i,:);
%    T{i} = T_matrix(T_matrix(:,1)==i,:);
%    T{i} = [i; i + 1]
%    T_matrix(T_matrix(:,1)==track,:);
%    plot(T_matrix(T_matrix(:,1)==track,:));
end

%from here the track is stored as its own matrix in a cell array
%We want the script to determine the number of tracks from the manual track
%datasheet; some commented out code is due to testing what works

%distance = sqrt((x - center_of_pillar(1, 1)).^2 + (y - center_of_pillar(1, 2)).^2);
%sqrt((T{1,j}(:,3) - center_of_pillar(1, 1)).^2 + (T{1,j}(:,4) - center_of_pillar(1, 2)).^2);

%This loop normalizes each individual time interval of the each track and
%plots them all together.

tracks = size(T,2);
for j = 1:tracks
    max_t = max(T{1,j}(:,2));  %End time of track
    min_t = min(T{1,j}(:,2));  %Start time of track
```

```matlab
int_time = max_t - min_t;  %Time interval
total_time = int_time + 1; %Total_time
hold on
%plot(T{1,j}(:,2),T{1,j}(:,3));
%plot(T{1,j}(:,2),sqrt((T{1,j}(:,3) - center_of_pillar(1, 1)).^2 + (T{1,j}(:,4) -
center_of_pillar(1, 2)).^2));
plot(1:total_time,sqrt((pix_con * T{1,j}(:,3) - center_of_pillar(1, 1)).^2 + (pix_con *
T{1,j}(:,4) - center_of_pillar(1, 2)).^2), 'LineWidth', 2.0);
xlabel('Time interval (s)');
ylabel('Distance from pillar center ({\mu}m)');
end

hold off
```

B.7   Single curvature plot script of active nematic and top of a pillar

Single_curvature_plot_script_V2.m

```matlab
X = xlsread('Curvatureplots_V2.xlsx');

% numColumn = size(X(1,:),2);
% numOfCells = numColumn/3;
% plotCellArray = {};
%
% % Places each individual set of pillar data to its individual cell within
% % the array
%
% for i=1:numOfCells
%     plotCellArray{i}=X(:,3*i-2:3*i);
% end
%
% % Normalizes the curve plots to have them shift downward by it's minimum
% % value
%
% for j=1:numOfCells
%     min_plot = min(plotCellArray{j}(:,2));
%     plotCellArray{j}(:,2) = plotCellArray{j}(:,2) - min_plot;
% end
%
% % Plots each normaized array into a single graph
%
% hold on
% for k=1:numOfCells
%     plot(plotCellArray{1,k}(:,1), plotCellArray{1,k}(:,2), 'LineWidth', 2.0);
%     xlabel('x-position ({\mu}m)');
```

```
%    ylabel('y-position ({\mu}m)');
% end
% hold off

min_pillar_point = min(X(:,3));

norm_nematic = X(:,2) - min_pillar_point;
norm_pillar = X(:,3) - min_pillar_point;

x_axis_radius = X(:,1) ./ 2;


hold on
% plot(X(:,1),X(:,2), 'LineWidth', 2.0);
% plot(X(:,1),X(:,3), 'LineWidth', 2.0);
plot(x_axis_radius,norm_nematic, 'LineWidth', 2.0);
plot(x_axis_radius,norm_pillar, 'LineWidth', 2.0);
legend('Nematic Layer', 'Pillar Top');
ylabel('z-position ({\mu}m)');
xlabel('radial position, r ({\mu}m)');
set(gca,'FontSize',20)
hold off
```

B.8   Vrms vs oil thickness plotting script

Vrms_thiccness_plots.m

```
Data = xlsread('vrms_vs_thickness_V5.xlsx');

%The scale bar for 20X is 3.07 pixel/micron
%The reciprocated, the scale is 0.325732899 micron/pixel

scale = 0.325732899;
oil_THICCNESS = Data(:,3);
oil_THICCNESS_Var = Data(:,4);
Vrms_inside = Data(:,5) .* scale;
Vrms_inside_Var = Data(:,6) .* scale;

p = polyfit(oil_THICCNESS, Vrms_inside, 1);
px = [min(oil_THICCNESS), max(oil_THICCNESS)];
py = polyval(p, px);

hold on
scatter(oil_THICCNESS, Vrms_inside,'filled')
```

```
errorbar(oil_THICCNESS, Vrms_inside, Vrms_inside_Var, Vrms_inside_Var,
oil_THICCNESS_Var, oil_THICCNESS_Var, 'o');
plot(px, py, 'k');
xlabel('Oil thickness, h (\mum )');
ylabel('Vrms (\mum/s)');
set(gca,'FontSize',20)
hold off
```

     Defect density vs oil thickness plotting script

DefectDensity_plots.m

```
clc;
clear all;

Data = xlsread('DefectDensityvsThickness_V4.xlsx', 'Sheet3');

oil_THICCNESS = Data(:,1);
oil_THICCNESS_Var = Data(:,2);

posDefectDensity = Data(:,3);
negDefectDensity = Data(:,4);

plus_p = polyfit(oil_THICCNESS, posDefectDensity, 1);
plus_px = [min(oil_THICCNESS), max(oil_THICCNESS)];
plus_py = polyval(plus_p, plus_px);

neg_p = polyfit(oil_THICCNESS, negDefectDensity, 1);
neg_px = [min(oil_THICCNESS), max(oil_THICCNESS)];
neg_py = polyval(neg_p, neg_px);

hold on
scatter(oil_THICCNESS, posDefectDensity, 'filled', 'b')
scatter(oil_THICCNESS, negDefectDensity, 'filled', 'MarkerFaceColor', [0.8500 0.3250
0.0980])
plot(plus_px, plus_py, 'b');
plot(neg_px, neg_py, 'Color', [0.8500 0.3250 0.0980]);
xlabel('Oil thickness, h (\mum )');
ylabel('Defect Density (1/m^2)');
legend('+1/2 Defects', '-1/2 defects');
set(gca,'FontSize',20)
hold off
```

B.10   Defect counting from sheet script

Defect_count_from_sheet.m

```matlab
clc;
clear all;

Data = xlsread('DefectDensityvsThickness_V4.xlsx', 'Sheet3');

oil_THICCNESS = Data(:,1);
oil_THICCNESS_Var = Data(:,2);

posDefectDensity = Data(:,3);
negDefectDensity = Data(:,4);

plus_p = polyfit(oil_THICCNESS, posDefectDensity, 1);
plus_px = [min(oil_THICCNESS), max(oil_THICCNESS)];
plus_py = polyval(plus_p, plus_px);

neg_p = polyfit(oil_THICCNESS, negDefectDensity, 1);
neg_px = [min(oil_THICCNESS), max(oil_THICCNESS)];
neg_py = polyval(neg_p, neg_px);

hold on
scatter(oil_THICCNESS, posDefectDensity, 'filled', 'b')
scatter(oil_THICCNESS, negDefectDensity, 'filled', 'MarkerFaceColor', [0.8500 0.3250 0.0980])
plot(plus_px, plus_py, 'b');
plot(neg_px, neg_py, 'Color', [0.8500 0.3250 0.0980]);
xlabel('Oil thickness, h (\mum )');
ylabel('Defect Density (1/m^2)');
legend('+1/2 Defects', '-1/2 defects');
set(gca,'FontSize',20)
hold off
```

References

[1]   G. Popkin, "The Physics of Life," *Nature,* vol. 529, pp. 16-18, 2016.

[2]   DTEKAdmin, "DTEK Live Bee Removal," DTEK Live Bee Removal, 10 July 2020. [Online]. Available: https://dteklivebeeremoval.com/what-to-do-if-you-spot-a-swarm-of-bees/.

[3]   M. Morimoto, "Free the Ocean Blog," [Online]. Available: https://www.freetheocean.com/journal/images-of-schools-of-fish/.

[4]   E. Lushi, H. Wioland and R. E. Goldstein, "Fluid flows created by swimming bacteria drive self-organization in confined suspensions," *PNAS,* vol. 111, no. 27, pp. 9733-9738, 2014.

[5]   X. Tang and J. V. Selinger, "Orientation of topological defects in 2D nematic liquid crystals," *Soft Matter,* vol. 13, pp. 5481-5490, 2017.

[6]   S. J. DeCamp, G. S. Redner, A. Baskaran, M. F. Hagan and Z. Dogic, "Orientational order of motile defects in active nematics," *Nat. Mat.,* vol. 14, pp. 1110-1115, 2015.

[7]   A. Opathalage, M. M. Norton, M. P. N. Juniper, S. A. Aghvami, B. Langeslay and S. Fraden, "Self-organized dynamics and the transition to turbulence of confined active nematics," *PNAS,* vol. 116, no. 11, pp. 4788-4797, 2019.

[8]   P. Guillamat, J. Ignés-Mullol, S. Shankar, M. C. Marchetti and F. Sagués, "Probing the shear viscosity of an active nematic film," *Phys. Rev.,* vol. 94, no. 6, 2016.

[9]   K. Thijssen, D. A. Khaladj, S. Aghvami, M. Gharbi, S. Fraden, J. Yeomans, L. S. Hirst and T. Shendruk, "Submersed micropatterned structures control active nematic flow, topology, and concentration," *PNAS,* vol. 118, no. 38, 2021.

[10] D. Needleman and Z. Dogic, "Active matter at the interface between materials science and cell biology," *Nature Reviews Materials,* vol. 2, no. 17048, 2017.

[11] V. A. Porvatov, A. D. Rozenblit, A. A. Dmitriev, O. I. Burmistrov, D. A. Petrova, G. Y. Gritsenko, E. M. Puhtina, E. I. Kretov, D. S. Filonov, A. Souslov and N. A. Olekhno, "Optimizing self-rotating bristle-bots for active matter implementation with robotic swarms," *Journal of Physics: Conference Series,* vol. 2086, p. 012202, 2021.

[12] T. Ishikawa, "Suspension biomechanics of swimming microbes," *J. R. Soc. Interface,* vol. 6, p. 815–834, 2009.

[13] H. Wioland, F. G. Woodhouse, J. Dunkel, J. O. Kessler and R. E. Goldstein, "Confinement stabilizes a bacte-rial suspension into a spiral vortex," *Phys. Rev. Lett.,* vol. 110, no. 268102, 2013.

[14] J. Chen, "Nanobiomechanics of living cells: a review," *Interface Focus,* vol. 4, no. 20130055, 2014.

[15] M. J. Han, D. Wei, H. S. Yun, S.-h. Lee, H. Ahn, D. M. Walba, T. J. Shin and D. K. Yoon, "Precise orientation control of a liquid crystal organic semiconductor via anisotropic surface treatment," *NPG Asia Materials,* vol. 14, no. 28, 2022.

[16] L. S. Hirst, Fundamentals of Soft Matter Science, Boca Raton: CRC Press Taylor and Francis Group, 2013.

[17] Q. Liu, B. Senyuk, J. Tang, T. Lee, J. Qian, S. He and I. I. Smalyukh, "Plasmonic Complex Fluids of Nematiclike and Helicoidal Self-Assemblies of Gold Nanorods with a Negative Order Parameter," *Physical Review Letters,* vol. 109, no. 088301, 2012.

[18] A. C. Toma, R. Dootz and T. Pfohl, "Analysis of complex fluids using microfluidics: the particular case of DNA/polycations assemblies," *J. Phys. D: Appl. Phys.,* vol. 46, no. 114001, 2013.

[19] C. Blanc, D. Coursault and E. Lacaze, "Ordering nano- and microparticles assemblies with liquid crystals," *Liquid Crystals Reviews,* vol. 1, no. 2, p. 83–109, 2013.

[20] O. Lavrentovich, "Nematic Liquid Crystals: Defects," *Materials Science,* pp. 6071-6076, 2001.

[21] T. B. Saw, W. Xi, B. Ladoux and C. T. Lim, "Biological Tissues as Active Nematic Liquid Crystals," *Adv. Mater.,* vol. 30, no. 1802579, 2018.

[22] A. Sengupta, S. Herminghaus and C. Bahr, "Liquid crystal microfluidics: surface, elastic and viscous interactions at microscales," *Liquid Crystals Reviews,* vol. 2, no. 2, pp. 73-110, 2014.

[23] X. Tang and J. V. Selinger, "Orientation of topological defects in 2D nematic liquid crystals," *Soft Matter,* vol. 13, pp. 5481-5490, 2017.

[24] X. Tang and J. V. Selinger, "Alignment of a topological defect by an activity gradient," *Phys. Rev. E,* vol. 103, no. 022703, 2021.

[25] H. Zhang, J. Zhu, Q. Li and Q. Tan, "Design of Light Guide Plate Using White Light Emitting Diode for Direct Illumination of Liquid Crystal Display," *Symposium on Photonics and Optoelectronics,* pp. 1-4, 2010.

[26] M. M. Montasser and D. Korzec, "Investigation of using the organic thin film transistors in the pixel circuit of the active matrix organic light emitting diode flat panel display," *2008 International Conference on Microelectronics,* pp. 437- 440, 2008.

[27] D.-H. Jeon and S.-W. Lee, "Unified Overdrive Technology Applicable to Liquid-Crystal Displays and Organic Light- Emitting Diode Displays Utilizing Linearity of Transitions in Voltage Domain," *IEEE Transactions on Electron Devices,* vol. 65, no. 7, pp. 2885-2891, 2018.

[28] B. Jerome, "Surface effects and anchoring in liquid crystals," *Rep Prog Phys,* vol. 54, no. 391, p. 391–451, 1991.

[29] M. C. Marchetti, "Spontaneous flows and self-propelled drops," *Nature,* vol. 491, p. 340–341, 2012.

[30] A. Doostmohammadi, J. Ignés-Mullol, J. M. Yeomans and F. Sagués, "Active nematics," *Nature Communications,* vol. 9, no. 3246, 2018.

[31] D. S. Kim, S. Čopar, U. Tkalec and D. K. Yoon, "Mosaics of topological defects in micropatterned liquid crystal textures," *Science Advances,* vol. 4, no. 11, 2018.

[32] D. C. Zografopoulos, E. E. Kriezis and T. D. Tsiboukis, "Tunable Highly Birefringent Bandgap-Guiding Liquid-Crystal Microstructured Fibers," *Journal of Lightwave Technology,* vol. 24, no. 9, pp. 3427-3432, 2006.

[33] D. C. Zografopoulos, E. E. Kriezis and T. D. Tsiboukis, "Photonic crystal-liquid crystal fibers for single-polarization or high-birefringence guidance," *Optics Express,* vol. 14, no. 2, pp. 914-925, 2006.

[34] B. Senyuk, H. Wonderly, M. Mathews, Q. Li, S. V. Shiyanovskii and O. D. Lavrentovich, "Surface alignment, anchoring transitions, optical properties, and topological defects in the nematic phase of thermotropic bent-core liquid crystal A131," *Physical Review E,* vol. 82, no. 041711, 2010.

[35] P. Rodgers, "Top down, bottom up," *Nature Nanotechnology,* 2006.

[36] A. Honglawan, D. A. Beller, M. Cavallaro, R. D. Kamien, K. J. Stebe and S. Yang, "Pillar-Assisted Epitaxial Assembly of Toric Focal Conic Domains of Smectic-A Liquid Crystals," *Advanced Materials,* vol. 23, p. 5519–5523, 2011.

[37] C. Gear, K. Diest, V. Liberman and M. Rothschild, "Engineered liquid crystal anchoring energies with nanopatterned surfaces," *Optics Express,* vol. 23, no. 2, pp. 807-814, 2015.

[38] Y. Choi, H. Yokoyama and J. S. Gwag, "Determination of surface nematic liquid crystal anchoring strength using nano-scale surface grooves," *Optics Express,* vol. 21, no. 10, pp. 12135-12144, 2013.

[39] D. Dell'Arciprete, M. L. Blow, A. T. Brown, F. D. C. Farrell, J. S. Lintuvuori, A. F. McVey, D. Marenduzzo and W. C. K. Poon, "A growing bacterial colony in two dimensions as an active nematic," *Nature Communications,* vol. 9, no. 4190, 2018.

[40] Z. You, D. J. G. Pearce, A. Sengupta and L. Giomi, "Geometry and Mechanics of Microdomains in Growing Bacterial Colonies," *Phys. Rev. X,* vol. 8, no. 031065, 2018.

[41] H. Li, X.-q. Shi, M. Huang, X. Chen, M. Xiao, C. Liu, H. Chaté and H. P. Zhang, "Data-driven quantitative modeling of bacterial active nematics," *PNAS,* vol. 116, no. 3, pp. 777-785, 2018.

[42] M. Basaran, Y. I. Yaman, T. C. Yüce, R. Vetter and A. Kocabas, "Large-scale orientational order in bacterial colonies during inward growth," *eLife,* vol. 11, no. 72187, 2022.

[43] D. v. H. t. Echten, G. Nordemann, M. Wehrens, S. Tans and T. Idema, "Defect dynamics in growing bacterial colonies," *arXiv [Preprint] (2020). https://arxiv.org/,* 2021.

[44] T. B. Saw, A. Doostmohammadi, V. Nier, L. Kocgozlu, S. Thampi, Y. Toyama, P. Marcq, C. T. Lim, J. M. Yeomans and B. Ladoux, "Topological defects in epithelia govern cell death and extrusion," *Nature,* vol. 544, p. 212–216, 2017.

[45] K. Kawaguchi, R. Kageyama and M. Sano, "Topological defects control collective dynamics in neural progenitor cell cultures," *Nature,* vol. 545, p. 327–331, 2017.

[46] C. Pérez-González, R. Alert, C. Blanch-Mercader, M. Gómez-González, T. Kolodziej, E. Bazellieres, J. Casademunt and X. Trepat, "Active wetting of epithelial tissues," *Nature Physics ,* vol. 15, p. 79–88, 2019.

[47] G. Duclos, C. Blanch-Mercader, V. Yashunsky, G. Salbreux, J. F. Joanny, J. Prost and P. Silberzan, "Spontaneous shear flow in confined cellular nematics," *Nature Physics,* vol. 14, p. 728–732, 2018.

[48] G. Duclos, C. Erlenkämper, J.-F. Joanny and P. Silberzan, "Topological defects in confined populations of spindle-shaped cells," *Nature Physics,* vol. 13, p. 58–62, 2017.

[49] L. Huber, R. Suzuki, T. Krüger, E. Frey and A. R. Bausch, "Emergence of coexisting ordered states in active matter systems," *Science,* vol. 361, no. 6399, pp. 255-258, 2018.

[50] N. Kumar, R. Zhang, J. J. d. Pablo and M. L. Gardel, "Tunable structure and dynamics of active liquid crystals," *Science Advances,* vol. 4, no. 10, 2018.

[51] R. Zhang, N. Kumar, J. L. Ross, M. L. Gardel and J. J. d. Pablo, "Interplay of structure, elasticity, and dynamics in actin-based nematic materials," *PNAS,* vol. 115, no. 2, pp. E124-E133, 2017.

[52] F. J. Nédélec, T. Surrey, A. C. Maggs and S. Leibler, "Self-organization of microtubules and motors," *Nature,* vol. 389, p. 305–308, 1997.

[53] T. Sanchez, D. T. N. Chen, S. J. DeCamp, M. Heymann and Z. Dogic, "Spontaneous motion in hierarchically assembled active matter," *Nature,* vol. 491, p. 431–434, 2012.

[54] P. Nelson, Biological Physics: Energy, Information, Life, New York: W. H. Freeman and Company, 2004.

[55] J. R. McIntosh, E. O'Toole, G. Morgan, J. Austin, E. Ulyanov, F. Ataullakhanov and N. Gudimchuk, "Microtubules grow by the addition of bent guanosine triphosphate tubulin to the tips of curved protofilaments," *J. Cell Biol.,* vol. 217, no. 8, p. 2691–2708, 2018.

[56] G. Henkin, S. J. DeCamp, D. T. N. Chen, T. Sanchez and Z. Dogic, "Tunable dynamics of microtubule-based active isotropic gels," *Phil. Trans. R. Soc. A,* vol. 372, no. 20140142, 2014.

[57] T. N. Shendruk, A. Doostmohammadi, K. Thijssen and J. M. Yeomans, "Dancing disclinations in confined active nematics," *Soft Matter,* vol. 13, no. 3853, 2017.

[58] A. J. Tan, E. Roberts, S. A. Smith, U. A. Olvera, J. Arteaga, S. Fortini, K. A. Mitchell and L. H. Hirst, "Topological chaos in active nematics," *Nat. Phys.,* vol. 15, p. 1033–1039, 2019.

[59] B. Martínez-Prat, J. Ignés-Mullol, J. Casademunt and F. Sagués, "Selection mechanism at the onset of active turbulence," *Nat. Phys.,* vol. 15, p. 362–366, 2019.

[60] R. Zhang, Y. Zhou, M. Rahimi and J. J. d. Pablo, "Dynamic structure of active nematic shells," *Nature Comm.,* vol. 7, no. 13483, 2016.

[61] P. G. D. Gennes and J. Prost, The Physics of Liquid Crystals, New York: Oxford University Press, 1993.

[62] E. J. Hemingway, P. Mishra, M. C. Marchetti and S. M. Fielding, "Correlation lengths in hydrodynamic models of active nematics," *Soft Matter,* vol. 12, p. 7943–7952, 2016.

[63] J. Hardouin, R. Hughes, A. Doostmohammadi, J. Laurent, T. Lopez-Leon, J. M. Yeomans and J. F. I.-M. Sagues, "Reconfigurable flows and defect landscape of confined active nematics," *Nature Comm. Phys.,* vol. 2, no. 121, 2019.

[64] J. Hardoüin, J. Laurent, T. Lopez-Leon, J. Ignés-Mullol and F. Sagués, "Active boundary layers," *arXiv cond-mat.soft,* 2020.

[65] Y. Li, N. Khuu, E. Prince, M. Alizadehgiashi, E. Galati, O. D. Lavrentovich and E. Kumacheva, "Nanoparticle-laden droplets of liquid crystals: Interactive morphogenesis and dynamic assembly," *Science Advances ,* vol. 5, 2019.

[66] P. Guillamat, J. Ignés-Mullol and F. Sagués, "Taming active turbulence with patterned soft interfaces," *Nature Communications,* vol. 8, no. 564, 2017.

[67] P. Guillamat, J. Ignés-Mullol and F. Sagués, "Control of active liquid crystals with a magnetic field," *PNAS,* vol. 113, p. 5498–5502, 2016.

[68] A. Maitra, P. Srivastava, M. C. Marchetti, J. S. Lintuvuori, S. Ramaswamy and M. Lenz, "A nonequilibrium force can stabilize 2D active nematics," *Proceedings of the National Academy of Sciences,* vol. 115, no. 27, pp. 6934-6939, 2018.

[69] S. Shankar, S. Ramaswamy, M. C. Marchetti and M. J. Bowick, "Defect Unbinding in Active Nematics," *Phys. Rev. Lett.,* vol. 121, no. 108002, 2018.

[70] Z. Cui, J. Su and X. Zeng, "Effects of Anchoring Boundary Conditions on Active Nematics," *Current Nanoscience,* vol. 13, no. 4, 2017.

[71] L. Giomi, L. Mahadevan, B. Chakraborty and M. Hagan, "Excitable patterns in active nematics," *Phys. Rev. Lett.,* vol. 106, no. 218101, 2011.

[72] R. A. Simha and S. Ramaswamy, "Hydrodynamic fluctuations and instabilities in ordered suspensions of self-propelled particles," *Phys. Rev. Lett.,* vol. 89, no. 058101, 2002.

[73] V. M. O. Batista, M. L. Blow and M. M. T. d. Gama, "The effect of anchoring on the nematic flow in channels," *Soft Matter,* vol. 11, p. 4674–4685, 2015.

[74] L. M. Lemma, S. J. DeCamp, Z. You, L. Giomi and Z. Dogic, "Statistical properties of autonomous flows in 2D active nematics," *Soft Matter,* vol. 15, pp. 3264-3272, 2019.

[75] H.-J. Butt, K. Graf and M. Kappl, Physics and Chemistry of Interfaces, Weinheim: WILEY-VCH Verlab GmbH & Co. KGaA, 2006.

[76] S. K. Mitra and S. Chakraborty, Microfluidics and Nanofluidics Handbook: Fabrication, Implementation, and Applications, Boca Raton: CRC Press, 2012.

[77] D. A. Khaladj, A. J. Tan and L. S. Hirst, "Using epoxy-based lithography to probe confinement effects on active nematics," *Proc. SPIE,* vol. 11092, 2019.

[78] Y. H. Tee, T. Shemesh, V. Thiagarajan, R. F. Hariadi, K. L. Anderson, C. Page, N. Volkman, D. Hanein, S. Sivaramakrishnan, M. M. Kozlov and A. D. Bershadsky, "Cellular chirality arising from the self-organization of the actin cytoskeleton," *Nat Cell Biol.,* vol. 17, no. 4, pp. 445-457, 2015.

[79] A. Doostmohammadi, T. Shendruk, K. Thijssen and J. M. Yeomans, "Onset of meso-scale turbulence in active nematics," *Nat. Commun.,* vol. 8, 2017.

[80] S. Chandragiri, A. Doostmohammadi, J. M. Yeomans and S. P. Thampi, "Active transport in a channel: Stabilisation by flow or thermodynamics," *Soft Matter,* vol. 15, p. 1597–1604, 2019.

[81] F. S. LM Pismen, "Viscous dissipation and dynamics of defects in an active nematic," *The Eur. Phys. J. E.,* vol. 40, no. 92, 2017.

[82] L. Metselaar, I. Dozov, K. Antonova, E. Belamie, P. Davidson, J. M. Yeomans and A. Doostmohammadi, "Electric-field-induced shape transition of nematic tactoids," *Phys. Rev. E,* vol. 96, no. 2, 2017.

[83] R. Alert, J. F. Joanny and J. Casademunt, "Universal scaling of active nematic turbulence," *Nat. Phys.,* vol. 16, p. 682–688, 2020.

[84] K. Thijssen, M. R. Nejad and J. M. Yeomans, "Role of friction in multidefect ordering," *Phys. Rev. Lett.,* vol. 125, no. 218004, 2020.

[85] B. Zhang, B. Hilton, C. Short, A. Souslov and A. Snezhko, "Oscillatory chiral flows in confined active fluids with obstacles," *Phys. Rev. Res.,* vol. 2, no. 043225, 2020.

[86] F. Kempf, R. Mueller, E. Frey, J. M. Yeomans and A. Doostmohammadi, "Active matter invasion," *Soft Matter,* vol. 15, p. 7538–7546, 2019.

[87] B. Martínez-Prat, R. Alert, F. Meng, J. Ignés-Mullol, J.-F. Joanny, J. Casademunt, R. Golestanian and F. Sagués, "Scaling regimes of active turbulence with external dissipation," *Phys. Rev. X,* vol. 11, no. 3, 2021.

[88] R. Zhang, S. A. Redford, P. V. Ruijgrok, N. Kumar, A. Mozaffari, S. Zemsky, A. R. Dinner, V. Vitelli, Z. Bryant, M. L. Gardel and J. J. d. Pablo, "Spatiotemporal control of liquid crystal structure and dynamics through activity patterning," *Nat. Mater.,* vol. 20, p. 875–882, 2021.

[89] S. Shankar and M. C. Marchetti, "Hydrodynamics of active defects: From order to chaos to defect ordering," *Phys. Rev. X,* vol. 9, no. 041047, 2019.

[90] A. Mozaffari, R. Zhang, N. Atzin and J. J. d. Pablo, "Defect spirograph: Dynamical behavior of defects in spatially patterned active nematics," *Phys. Rev. Lett.,* vol. 126, no. 227801, 2021.

[91] K. A. Mitchell, A. J. Tan, J. Arteaga and L. S. Hirst, "Fractal generation in a two-dimensional active-nematic fluid," *Chaos,* vol. 31, no. 073125, 2021.